The Dissertation Committee for Zhiwei Fang Certifies that this is the approved version of the following Dissertation:

Structural Engineering and Electronic Tuning of Non-Noble Transition Metal-Based Electrocatalysts

Committee:

Guihua Yu, Supervisor

Arumugam Manthiram

Keith P. Johnston

Yuanyue Liu

Structural Engineering and Electronic Tuning of Non-Noble Transition Metal-Based Electrocatalysts

by

Zhiwei Fang

Dissertation

Presented to the Faculty of the Graduate School of

The University of Texas at Austin

in Partial Fulfillment

of the Requirements

for the Degree of

Doctor of Philosophy

The University of Texas at Austin

May 2021

Dedication

Dedicated to my parents Chengyi Fang & Ailan Li

Acknowledgements

First, I wish to especially thank my supervisor Prof. Guihua Yu for his continuous support and invaluable guidance through my entire doctoral research study at the University of Texas at Austin. Prof. Yu offers me enough space to identify my research interest and meanwhile teaches me to think hard and work hard. Meanwhile, I want to express my gratitude to all my dissertation committee. My sincere thanks go to Prof. Arumugam Manthiram, Prof. Keith P. Johnston, and Prof. Yuanyue Liu for kindly serving as my committee members. Without their insightful guidance and useful feedback, I would not have made it.

I would like to offer my special thanks to many people who have provided much assistance in my Ph.D. research. Dr. Lele Peng and Dr. Yue Zhu, two former Ph.D. students in our group, taught me numerous experimental and technical skills in the electrochemical fields. Dr. Ping Wu, a visiting postdoc scholar in our group and now a professor at Nanjing Normal University, taught me plenty of experimental skills in materials synthesis and we share ideas together. I would like to extend my sincere thanks to so many wonderful colleagues in Dr. Yu's Research Group. I wish to offer my special thanks to Dr. Yumin Qian, Zhengyu Ju, Xiao Zhang, Dr. Panpan Zhang, Dr. Chunshuang Yan, Dr. Chade Lv, Dr. Yangen Zhou, Dr. Zhongchao Bai, Dr. Nana Wang, Dr. Ye Shi, Xingyi Zhou, Leyuan Zhang, Jiwoong Bae, Youhong Guo, Xuelin Guo, Wen Shi, Sishuang Tang, Lei Pan, Desiree Fernandez, Dr. Changkun Zhang, Dr. Jun Zhang, Ke Yan, Mingxiang Hu. My special thanks go to Prof. Changzheng Wu (University of Science and Technology of China) and Professor Judy J. Cha (Yale University) for those efficient collaborations.

My appreciation also goes out to my family and friends for their encouragement and support all through my studies. Finally, I would also like to express my thanks to several unique people whose names I prefer to keep in my own heart.

Abstract

Structural Engineering and Electronic Tuning of Non-Noble Transition Metal-Based Electrocatalysts

Zhiwei Fang, PhD

The University of Texas at Austin, 2021

Supervisor: Guihua Yu

Catalysis, a process that can accelerate chemical reactions, has become a pivotal role in producing renewable energy (e.g. fuel cells, solar energy, biofuels, etc.) s by environmentally friendly routes. Heterogeneous electrocatalysis has prompted intensive efforts, owing to their low thermodynamic requirements, cost-effective energy, high coulombic efficiency, and reduced carbon footprint. However, the unfavorable kinetics of most electrochemical reactions severely limits the large-scale applications of energy conversion devices. To reduce the reaction barrier, efficient electrocatalysts, with high active-site accessibility, abundant surface areas, good electrical conductivity, desirable electrical conductivity and long-term stability, are necessarily required.

This dissertation offers a dual-tuning strategy combining structural design and electronic tuning of non-noble-metal-based electrocatalysts. To push the mass/charge transfer of non-noble-meal-based catalysts for practical applications, strategies including structural engineering and optimized electronic modification are applied to achieve efficient and stable electrocatalysts.

Porosity engineering is firstly introduced in 2D transition metal-based electrocatalysts to alleviate the restacking issue of the 2D nanomaterials, offering large active surface areas and fast ion transfer (Chapter 3). Besides, to overcome the inferior electron transfer during the electrochemical process, electronic modification, such as anionic substitution, is employed to boost the electron transfer. By applying structural engineering and electronic modification in 2D electrocatalyst, both mass transport and charge transfer are improved. The density of state and the local electronic/atomic structure optimizations of electrocatalysts are further studied by modeling computation.

To extend the structural design and electronic modification to a broad range of electrocatalysts, gel-based electrocatalysts with enhanced mass/charge transfer are further introduced. Unlike conventional electrocatalysts prepared from bulky powders suffering from severe issues on mass transport and electron transfer, gel-based electrocatalysts offer larger numbers of active sites, due to unique hierarchical structures, compositional tunability, ease of functionalization, and high wettability for electrolyte penetration (Chapter 4). By introducing functional dopants or alloying with transition metals, not only the electron transfer of gel-derived alloys can be improved, but also the N adsorption energy can be regulated (Chapter 5). Finally, key strategies combining structural design and electronic tuning of non-noble-metal-based electrocatalysts are summarized and possible future directions are provided (Chapter 6).

Table of Contents

List of Tables xiii

List of Figures xiv

Chapter 1: Introduction 1

Chapter 2: General experimental procedures 9

2.1 Materials synthesis 9

2.2 Materials characterizations 9

2.2.1 Scanning electron microscopy 9

2.2.2 Transmission electron microscopy 9

2.2.3 Energy-dispersive X-ray spectroscopy 10

2.2.4 Raman spectroscopy 10

2.2.5 Fourier transform infrared spectroscopy 10

2.2.6 Ultraviolet-visible spectroscopy 10

2.2.7 Temperature-dependent electrical resistance test 11

2.2.8 Brunauer−Emmett−Teller test 11

2.2.9 Thermogravimetric analysis 11

2.3 Electrochemical measurements 11

2.3.1 Electrode preparation 11

2.3.2 Cyclic voltammograms and Linear sweep voltammograms 12

2.3.3 Electrochemical impedance spectroscopy 13

2.3.4 Electrochemical surface area 13

2.3.5 Cycling test and stability test 13

Chapter 3: Pore engineering and anion effect in 2D mixed-transition-metal-based electrocatalysts for water splitting 14

3.1 Introduction to 2D materials 14

3.2 Materials synthesis and characterization details 16

3.2.1 Synthesis of graphene oxide (GO) nanosheets 16

3.2.2 Synthesis of $NiCo(OH)_x$/rGO hybrid 17

3.2.3 Synthesis of $NiCoO_x$ holey nanosheets 17

3.2.4 Synthesis of $Ni_xCo_{3-x}Se_4$ Holey Nanosheets 18

3.2.5 Synthesis of NiCoP holey Nanosheets 19

3.2.6 Materials characterization 19

3.2.7 Electrochemical measurement and calculation 20

3.3 Results and discussion 21

3.3.1 Pore engineering in 2D nanostructured Ni/Co-oxide/selenide/phosphide 21

3.3.2 Metallic $NiCo_2Se_4$ holey nanosheets for electrocatalytic oxygen evolution 30

3.3.3 Anion effect in 2D nanostructured Ni/Co-oxide/selenide/phosphide for electrocatalytic hydrogen evolution 34

3.4 Conclusions 50

Chapter 4: Hybrid organic−inorganic hydrogels for electrocatalytic acidic water oxidation 53

4.1 Introduction to gels for electrocatalysis 53

4.2 Materials synthesis and characterization details 60

4.2.1 Synthesis of cyano coordination polymers 60

4.2.2 Synthesis of organic-inorganic hybrid hydrogels 61

4.2.3 Synthesis of control samples for acidic OER 63

4.2.4 EXAFS experimental details 64

4.2.5 Electrochemical measurements.....64

4.3 Results and discussion 65

4.3.1 Structural design in hybrid organic−inorganic hydrogel catalysts 65

4.3.2 Electronic modification in hybrid organic−inorganic hydrogel catalysts.....68

4.3.3 Acidic OER of hybrid organic−inorganic hydrogel electrocatalysts...72

4.4 Conclusions.....79

Chapter 5: Structural engineering and electronic tuning of Gel-Derived Alloys for Electrocatalytic Ammonium Synthesis.....81

5.1 Introduction to hydrogel-derived materials 81

5.2 Introduction to electrocatalytic NH_3 synthesis and Bi-based NRR catalysts 86

5.3 Materials synthesis and characterization details.....89

5.3.1 Synthesis of cyano coordination polymers 89

5.3.2 Synthesis of 3D amorphous BiNi electrocatalyst 89

5.3.3 Synthesis of 3D crystalline BiNi electrocatalyst 90

5.3.4 Materials characterization.....92

5.3.5 Electrochemical measurement 92

5.3.6 Determination of ammonia 93

5.3.7 Determination of hydrazine 94

5.3.8 Estimation of the maximum amount of NH_3 impurity from N_2 flow ..95

5.4 Results and discussion 96

5.4.1 Facilitating electron transfer by alloying Bi with Ni 96

5.4.2 Chemical adsorption of N_2 on BiNi alloy.....98

5.4.3 Bi-Ni Cyano Coordinated Polymers-derived 3D amorphous BiNi alloy 104

5.5 Conclusions.....114

Chapter 6: Summary 118

6.1 Dissertation summary 118

6.2 Future directions 121

References.....123

Vita.....130

List of Tables

Table 3.1: Synthesis of NCO holey nanosheets with different Ni/Co ratios in the precursor. 18

Table 3.2: Hydrogen adsorption enthalpy on NCO (111). 39

Table 3.3: Hydrogen adsorption enthalpy on NCS (010). 39

Table 3.4: Hydrogen adsorption enthalpy on NCP (001). 39

Table 3.5: Comparison of HER performance for holey NCP with other non-noble-metal HER electrocatalysts in alkaline solution. 44

Table 3.6: Comparison of HER performance for holey NCP with other non-noble-metal HER electrocatalysts at all-pH values. 46

Table 3.7: Comparison of overall water splitting application for holey NCP with other non-noble-metal electrocatalysts at basic media. 49

Table 5.1: Synthesis of amorphous BiNi alloy, crystalline BiNi alloy, and other metals. 91

Table 5.2: Comparison table of a-BiNi with recently reported Bi-based NRR electrocatalyst. 111

List of Figures

Figure 1.1: Electrochemical energy storage and conversion systems in modern society. 1

Figure 1.2: Energy conversion can bridge this gap, store this renewable energy as valuable chemicals. 2

Figure 1.3: Advanced energy conversion technologies: (a) water electrolyzer. (b) fuel cells. (c) Metal-air batteries. 3

Figure 1.4: (a) Activation energy barrier of a chemical reaction with and without catalyst. (b) heterogenous catalysis. 4

Figure 1.5: Some typical design strategies in electrocatalysts at both atomic level and nanoscale. 5

Figure 3.1: Some typical strategies of design 2D nanomaterials for improved electrochemical properties. 16

Figure 3.2: Schematic illustration of the key features of 2D holey structures during the electrochemical process. 22

Figure 3.3: Scheme of synthesis of Ni/Co-based oxide/selenide/phosphide holey nanosheets 23

Figure 3.4: XRD of a series of Ni/Co-based holey nanosheet samples and Rietveld refinement of the XRD data of $NiCo_2Se_4$ (black line, data points; red line, calculation line; green vertical line, marker points; blue line, difference line). 24

Figure 3.5: Crystal structure of $NiCo_2Se_4$ showing a monoclinic structure. 25

Figure 3.6: (a) HRTEM and SAED of a NCS holey nanosheet. (b) EDX images of NCS holey nanosheets. (c) HRTEM and SAED of a NCP holey nanosheet. (d) EDX images of NCP holey nanosheets. Scale bars: (a) 20 nm, (b) 200 nm, (c) 10 nm, 10 nm^{-1} in the inset of (c), (d) 200nm.....26

Figure 3.7: Chemically interconnected nanoparticles in holey nanosheet: (a)(b) TEM images and (c) HRTEM images of the holy structure. (d) Hole structures for enhanced mass and charge transfer during electrocatalysis. 27

Figure 3.8: STEM and SEM (inset) images of (a) NCO, (b) NCP and (c) NCS holey nanosheets (scale bar: 200 nm, inset: 500 nm). Particle size distribution in (d) NCO (8-12 nm) (e) NCP (12-18 nm) and (f) NCS (10-15nm) holey nanosheets. Hole size distribution in (g) NCO (8-12 nm) (h) NCP (12-18 nm) and (i) NCS (12-18 nm) holey nanosheets.....28

Figure 3.9: Comparison of overpotentials requires j = 10 mA cm^{-2} of NCS and NCO with different morphology in 1.0 M KOH.....29

Figure 3.10: (a) Density of states (DOS) of Ni/Co-oxides (NCO) and selenides (NCS) across the Fermi level. (b) Charge density wave (isosurface: 0.07 e/Bohr3) and (c) Temperature-dependent electrical resistance of NCS. 31

Figure 3.11: (a) 95% IR-corrected polarization curves, (b) overpotential @ 10 mA cm^{-2} and Tafel slop of NCS holey nanosheets with different compositions heteroatom doping degree. 32

Figure 3.12: (a) OH^- adsorption energy of Co_3Se_4, $NiCo_2Se_4$, and NiSe (010) facets. (b) 95% IR-corrected polarization curves of a series of $NiCo_2Se_4$, $NiCo_2O_4$, and RuO_2.....33

Figure 3.13: XPS test of a series of NCA holey NSs: (a) Ni $2p_{3/2}$ spectrum, (b) Co $2p_{3/2}$ spectrum, and (c) P $2p_{1/2}$ spectrum of NCP holey NSs. (d) Ni $2p_{3/2}$ spectrum, (e) Co $2p_{3/2}$ spectrum, and (f) Se 3d spectrum of NCS NSs. (h) Ni $2p_{3/2}$ spectrum, (h) Co $2p_{3/2}$ spectrum, and (i) O 1s spectrum of NCO holey NSs. 35

Figure 3.14: Electrical resistance plotted as a function of the temperature of Ni-Co-O, Ni-Co-P, and Ni-Co-Se. 37

Figure 3.15: (a) Atomic structure of the H-covered surfaces and (b) the corresponding H adsorption/desorption enthalpy diagram. 38

Figure 3.16: HER performance of a series of NCA holey nanosheets in 1.0 M KOH aqueous solution and the correlation between electron localization and hydrogen binding. 41

Figure 3.17: (a) LSV curves of NCP holey NSs. (b) Tafel plots of NCP holey NSs, c-NCP (control NSs, no holes), and bare Ni foam. (c) LSV curves of phosphide holey NSs. (d) HER performance of NCP holey NSs in acidic, neutral, and alkaline media. (e) Chronopotentiometric measurement of NCP holey NSs and c-NCP at the current density of 10 mA cm^{-2}. (f) Cycling stability of NCP holey NSs....42

Figure 3.18: (a) OER performance of NCP and NCO holey NSs on Ni foam. (b) LSV curve of NCP holey NSs for overall water splitting. (c) Stability test of water splitting for NCP holey nanosheets. 47

Figure 3.19: Digital photos of NCP/NCP holey NS-modified electrode couple for water electrolyzer showing H_2 and O_2 release on cathode and anode electrode, respectively....48

Figure 4.1: Schematic illustration of the key features of gel materials for electrocatalysis. 55
Figure 4.2: (a) Photograph of a typical Sn−Fe cyanogel. (b) Structural model of cyanogels. (c) Ligand-substitution reaction. 57
Figure 4.3: Diagram of the functionalization of cyanogel by adding carbon-based materials, polymers, and nanomaterials into cyanogel host. 59
Figure 4.4: Scheme of the formation of PPy/CCP gel dual-network (DN gels) and their digital photos. 61
Figure 4.5: Mechanism of the simultaneous formation of PPy/CCP DN gels..... 62
Figure 4.6: FTIR spectra of $K_3Fe(CN)_6$, $K_4Fe(CN)_6$, $Fe(CN)_6^{4-}$-doped PPy and undoped PPy. 63
Figure 4.7: Stability of InFeCo-CCP: XRD patterns of InFeCo-CCP before and after soaking in strong acid for 7 days, and after 100 OER cycles (1.23-2.00V vs. RHE)..... 65
Figure 4.8: (a) XRD results of double-network gels and pure InFeCo-cyanogels and the simulated XRD pattern. (b) TEM image (scale bar: 1 μm; inset: SAED pattern, scale bar: 10 nm in the inset of (b) and (c) STEM-HAADF image of double-network gels and corresponding elemental mapping with a pixel size of 1.5 Å (scale bar: 20 nm in c). 66
Figure 4.9: SEM images of (a) InFe-CCP and (b) double-network gels. (c) ECSA of DN gels and InFeCo-CCP..... 67
Figure 4.10: (a) XPS spectra of InFeCo-CCP (InFeCo-cyanogels) and double-network gels. (b) XANES and (c) EXAFS of double-network gels, InFeCo-CCP. ...68

Figure 4.11: The pre-edge structures of DN gels and InFeCo-CCP in Fe K-edge absorption spectra. The XANES of double-network gels shows two pre-edge peaks at 7112.8 eV and 7116 eV are the typical fingerprints of the Fe^{2+} oxidation state of $Fe(CN)_6^{4-}$.[15] 69

Figure 4.12: TGA curves of DN gels, InFeCo-CCP, and DN gels testing from room temperature to 700 ℃. 70

Figure 4.13: (a) LSV (polarization) after the ECSA normalization and (b) EIS curves of double-network gels and pure InFeCo cyanogel. 71

Figure 4.14: (a) LSV curves and (b) Tafel slopes of double-network gels, InFeCo-cyanogel, and PPy gel. (c) Chronoamperometric measurement of double-network gels and InFeCo- cyanogel for 50 h. (d) Cycling stability test. 72

Figure 4.15: (a) Raman, (b) FT-IR, and (c) Fe 2p and (d) In 3d XPS spectra of the double-network gel electrocatalyst before and after OER cycling in the pH = 0 aqueous electrolyte. 74

Figure 4.16: ICP-OES measurement of the concentration of (a) Fe and (b) Co from the electrolytes of DN gels and $InFeCo_x$. (c) The remaining metal amount for DN gels and $InFeCoO_x$ during the OER electrocatalysis based on ICP-OES analysis. 76

Figure 4.17: (a) Proposed OER mechanism for defect-rich cyano-based OER electrocatalyst and (b) corresponding calculated free energy diagram at the equilibrium potential on Fe and Co sites in InFeCo-CCP. 77

Figure 4.18: Calculated adsorption energies for H_2O molecules on Fe sites (top center) with different coordination numbers.....78

Figure 5.1: Schematic illustration of the key features of gels and their derivatives for electrocatalysis, including macro/mesopores for mass transfer, good electrical conductivity for charger transfer, controlled dopants for tunable catalytic activity, and self-supporting electrode features. 82
Figure 5.2: Electrocatalytic oxygen reduction activity of the cyanogel derived Pd−Ni nanocorals. 84
Figure 5.3: Synthetic routes for gel-derived metal/alloys. (a) Synthesis of Sn-Ni/graphene gels. (b) TEM images of Sn-Ni/GO double-network aerogels and (c) Sn-Ni/graphene dual framework. 85
Figure 5.4: Digital images of Bi-Ni-cyano-gel and sol by controlling the concentration in DEG solvent. 89
Figure 5.5: Schematic illustration of the synthesis of 3D amorphous BiNi and 3D crystalline BiNi. 90
Figure 5.6: XRD patterns of amorphous BiNi (a-BiNi), amorphous Ni (a-Ni), crystalline Bi (c-Bi), crystalline Ni (c-Ni), physically mixed high-crystalline Bi and Ni (c-Bi + c-Ni), crystalline BiNi (c-BiNi). 91
Figure 5.7: Calibration curves in 0.10 M Na_2SO_4 using NH_4Cl solutions of different concentrations from 0 to 1.0 μg mL^{-1}: (a) UV-vis of indophenol assays after incubated for 1 hour and (b) calibration curve used for estimation of NH_3 concentration. The absorbance at 655 nm was measured by UV-Vis spectrophotometer, and the fitting curve shows good linear relation of absorbance with NH_3 concentration. 94
Figure 5.8: (a) UV-vis spectra and (b) calibration curve of N_2H_4 with different concentrations from 0 to 1.0 μg mL^{-1} using p-$C_9H_{11}NO$ as the indicator. ...95

Figure 5.9: XPS survey scan of c-Bi and a-BiNi: Ni 2p and 3p peaks confirmed the introduction of Ni.....96
Figure 5.10: XPS Bi 4f spectra of Bi and BiNi alloy: peak shifts to lower energies in Bi 4f and higher energy in Ni 2p peaks, indicating the electron acceptor of Bi and the electron transfer from Ni to Bi. 97
Figure 5.11: EIS spectra of Bi and BiNi: smaller radius of the semicircles showing improved charge transfer in BiNi. 98
Figure 5.12: Adsorption of N_2 on (100) crystal facets of Bi and BiNi from three directions.....99
Figure 5.13: Gibbs free energy diagrams of NRR on different low-index crystal facets of Bi and BiNi from DFT calculation. For the Bi surface, molecular N_2 cannot chemically adsorb on (001) or (100) crystal facet, resulting in $\Delta G = 0$ in the first step. In comparison, both BiNi (001) and (100) crystal facets can chemisorb N_2, bringing our improved overall NRR kinetics. 100
Figure 5.14: Adsorption of N_2 on BiNi alloys versus Bi-metal: (a) Nitrogen (orange) adsorption on Bi and BiNi alloys: Ni-substitution can promote the N_2 adsorption while no adsorption on pure Bi-metal. (b) Energy diagram of NRR process on Bi and BiNi. The RDS is the 2nd step and Ni substitution can effectively modulate the adsorption abilities of nitrogen adsorption.....101

Figure 5.15: Electrocatalytic NRR activity of crystalline BiNi alloys and Bi. (a) CA curves under different voltages from -0.4V to -0.8V and CV curves of Bi and Bi-Ni alloys. (b) LSV curves of Bi and BiNi alloys in N_2 and Ar-saturated 0.1M Na_2SO_4 electrolyte. (c) The yield rate of NH_3 Faradic efficiency from -0.4 V to -0.8 V of Bi and BiNi alloys under N_2 production. 102

Figure 5.16: (a) XRD of a-BiNi and c-BiNi. (b) TEM, ED, (c) HRTEM, and (d) elemental mapping of a-BiNi.....104

Figure 5.17: Composition and crystallinity evolution of the reduction of Bi-Ni-CCP to BiNi via $NaBH_4$ in DEG. The amorphous phase can be indirectly characterized by annealing the samples under 400℃, Bi cannot form an amorphous phase by $NaBH_4$ reduction of Bi precursor, according to the experimental results in Figure 5.6.....105

Figure 5.18: TEM images of 3D a-BiNi on C grid: The 3D porous framework is composed of small nanosheets (around 20 nm diameter). Annealing the amorphous BiNi alloy catalyst at 400 ℃ in Ar transformed the amorphous phase into a phase-pure crystal, and the particle size can be maintained after heat treatment.....107

Figure 5.19: (a) CA curves under different voltages from -0.4V to -0.8V of a-BiNi alloys. (b) The yield rate of NH_3 production and Faradic efficiency from -0.4 V to -0.8 V of a-BiNi alloys and c-BiNi (crystalline alloys) alloys under N_2. (c) Comparison of the NH_3 yield rate at -0.6 V of c-Bi, c-Ni (crystalline Bi and Ni), a-BiNi, and c-BiNi alloys.....108

Figure 5.20: ECSAs of Bi-based NRR electrocatalysts: improved ECSA in amorphous BiNi compared with c-Bi and c-BiNi, due to enhanced electron transfer and amorphous feature. 109
Figure 5.21: Exclusion of N contamination in amorphous BiNi alloy: No N-species were found before electrochemical tests: (a) UV-vis absorption spectra of electrolyte under different testing conditions. No N signals are detected from (b) EDS and (c) XPS spectra in a-BiNi. 110
Figure 5.22: UV-vis spectrum from 420 to 510 nm of electrolytes after 2-hour-NRR of a-BiNi. 112
Figure 5.23: (a) Alternating cycling test of a-BiNi @−0.6 V (vs. RHE) between N_2 and Ar-saturated 0.1 M Na_2SO_4. (b) Long-term stability test of a-BiNi. (c) Post-XRD analysis of a-BiNi. 113
Figure 5.24: XRD of a-BiNi before and after NRR. No detectable difference between the fresh a-BiNi and post-NRR samples indicates no new phase or crystalline BiNi were formed. 114
Figure 5.25: Nitrogen cycle via biological and artificial methods 116
Figure 5.26: Nitrate reduction reaction process contributing to the future sustainability of fertilizer and renewable fuels recycling. 116
Figure 6.1: Conclusion and perspectives of structural engineering and electronic tuning of non-noble-metal-based electrocatalysts. 119

Chapter 1: Introduction

Driven by the increasingly rapid depletion of fossil fuels and global warming issues, developing advanced energy storage and conversion technologies, such as water electrolysis, fuel cells, and metal-air batteries, has become one of the most critical challenges for the sustainable development of society (Figure 1.1).[1-3] Electrochemical energy conversion is critical for sustainable development and climate change, which can bridge the gap between intermittent renewable energy, such as solar, wind, and hydro energy, and the continuous demand for human society (Figure 1.2). [4]

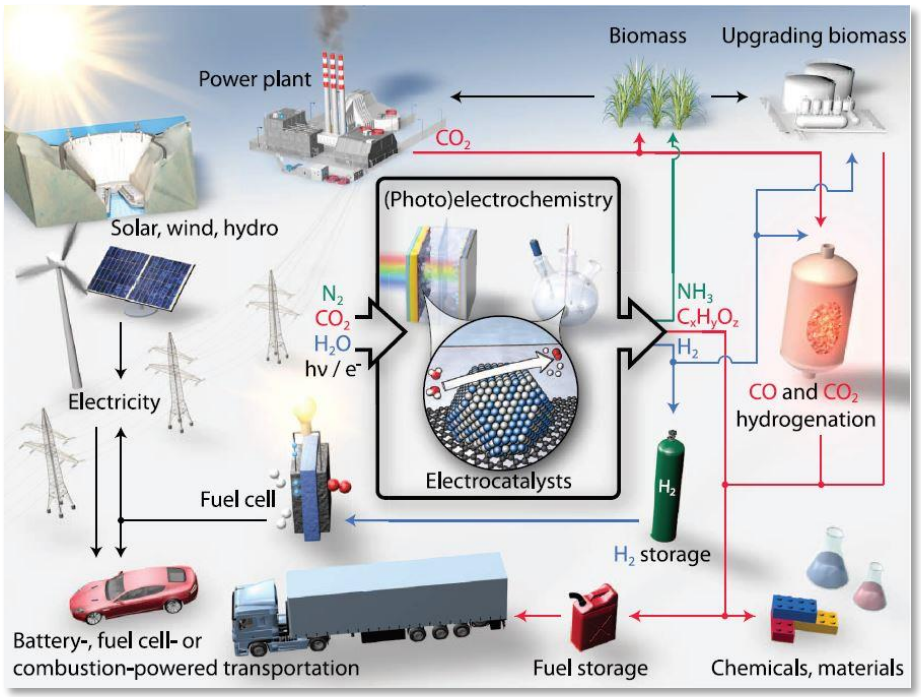

Figure 1.1: Electrochemical energy storage and conversion systems in modern society.

Seeking renewable and cost-effective energy sources is one of the significant challenges for the sustainable development of modern society. To date, considerable expectations have been held for the above-advanced energy technologies, where the

performance strongly depends on electrochemical conversion processes that can generate and store chemical energy through the breaking or formation of chemical bonds (Figure 1.3).[5] For example, the nitrogen reduction reaction (NRR) including $N_2 + 6\ H_2O + 6\ e^- \rightarrow 2\ NH_3 + 6\ OH^-$ and oxygen evolution reaction (OER): $2\ H_2O - 4e^- \rightarrow 4\ H^+ + O_2$ in electrocatalytic nitrogen fixation process.[6] For electrolytic cells, two fundamental electrochemical reactions, the hydrogen evolution reaction (HER) and OER, occur at the cathodic side and the anodic side, generating gaseous hydrogen and oxygen molecules and thus converting electrical energy into chemical energy.[7] Rechargeable metal-air batteries, operating based on oxygen reduction reaction (ORR) $O_2 + 4\ e^- \rightarrow 2O^{2-}$ and OER $2\ H_2O - 4e^- \rightarrow 4\ H^+ + O_2$, corresponding to the discharging and charging processes of batteries, have also stimulated great research attention for their high theoretical energy density and renewable fuel resources as they are empowered by oxygen from the air. However, the kinetics of those half-cell processes is relatively slow, which severely restricts the performance of corresponding energy devices.

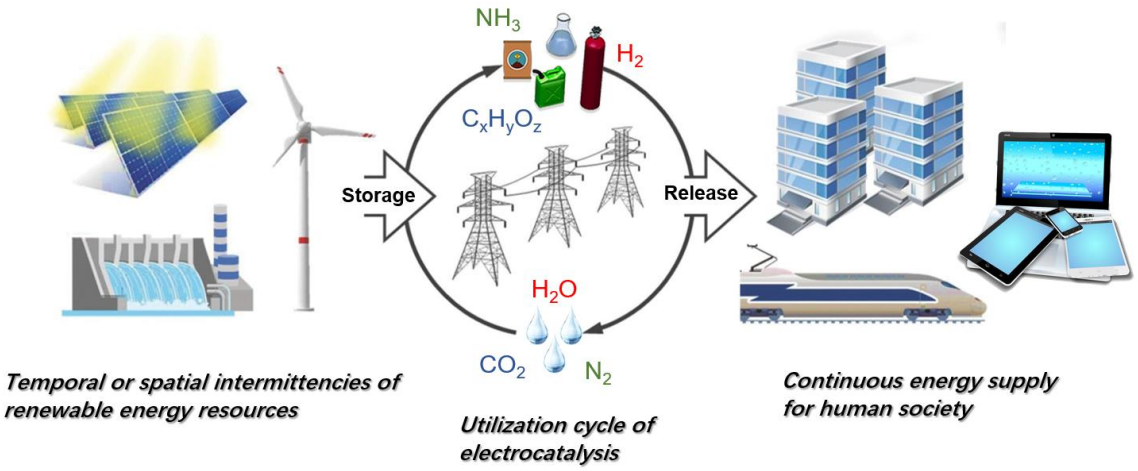

Figure 1.2: Energy conversion can bridge this gap, store this renewable energy as valuable chemicals.

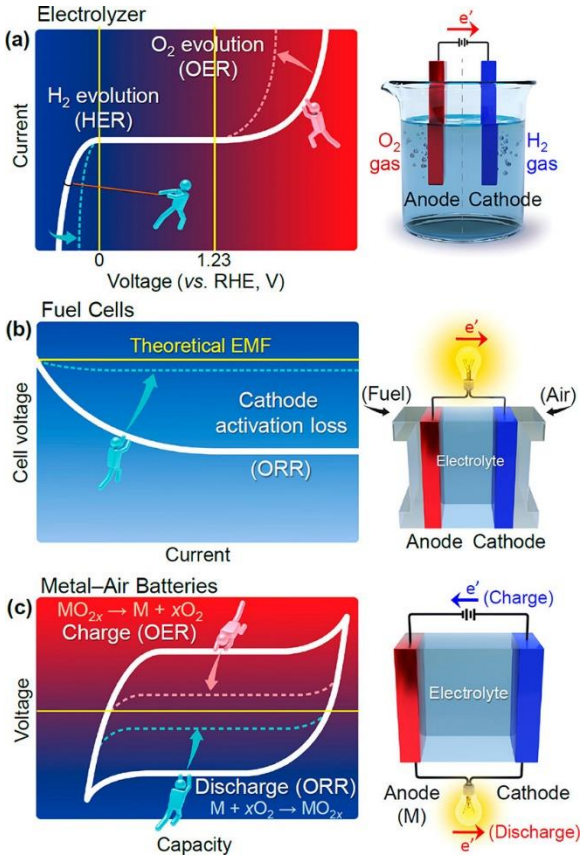

Figure 1.3: Advanced energy conversion technologies: (a) water electrolyzer. (b) fuel cells. (c) Metal-air batteries.

The sluggish kinetics mainly originates from the proton-coupled multi-electron transfer during those reactions, which requires high activation energy to overcome the activation barrier (Figure 1.4a). Catalysis is a process that can accelerate chemical reactions by reducing the energy barrier. Among them, electrocatalysis has prompted intensive efforts in the past several decades, owing to their relatively low thermodynamic requirements, low energy cost, high coulombic efficiency, and reduced carbon footprint. Electrocatalysis is a heterogeneous catalysis of multiple steps of proton-coupled electron transfer reactions. A heterogeneous catalysis reaction, shown in Figure 1.4b, typically start

from the absorption of reactant molecules in the electrolyte, following the chemical reaction, and finally the desorption of reaction products.[8]

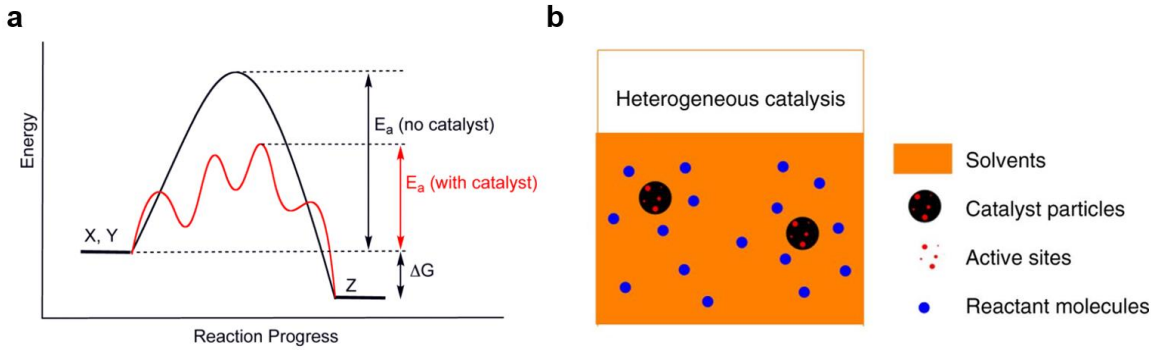

Figure 1.4: (a) Activation energy barrier of a chemical reaction with and without catalyst. (b) heterogenous catalysis.

Among different types of electrocatalysts, nanomaterials, due to their high surface area and abundant edges/defects as active sites to absorb reactant molecules, have become one of the most promising electrocatalysts. Typically, to design an efficient and stable electrocatalyst, intrinsic activity, as well as the electrochemical surface area (ECSA), need to be considered.[5] To increase the intrinsic catalytic activity, one approach is to regulate the electronic configuration by optimizing the chemical composition and crystal structure for the optimal binding energy of reactants and intermediates during electrocatalysis. During the electrochemical reaction, improving the intrinsic electrical conductivity of electrocatalysts is favorable to the charge transfer. Structural design, such as nanoengineering, can increase the ECSA by creating more active sites for adsorption and rapid channel for mass transfer, creating surface defects/vacancies as active sites, introducing structural disorder (amorphism), and modifying surface properties. For

example, gel-based materials with enhanced wettability are beneficial for aqueous electrolyte penetration and maximize the contact between electrode and ions.

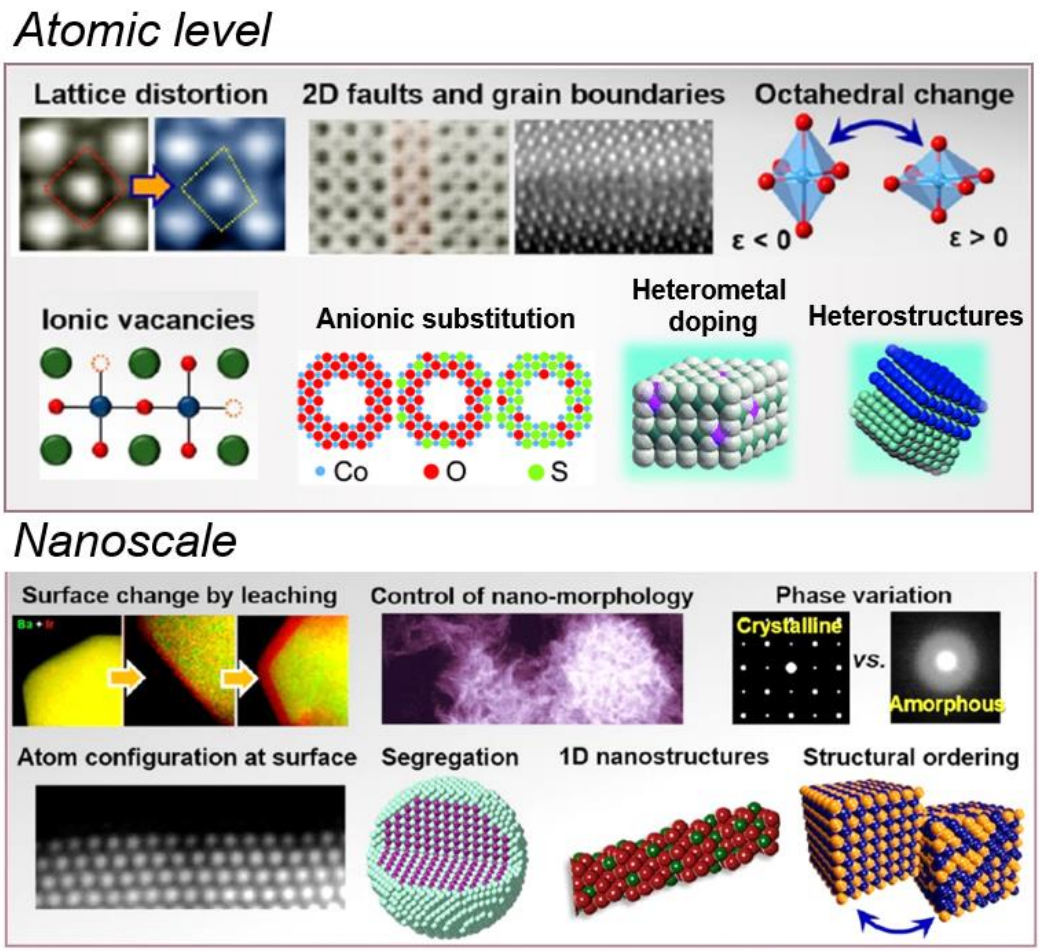

Figure 1.5: Some typical design strategies in electrocatalysts at both atomic level and nanoscale.

Generally, an optimized electrocatalyst should display high catalytic activity, high surface area, good selectivity for target materials, desirable electrical conductivity, and long-term durability.[9] For electrocatalysis, η_{10} is a common index of catalytic performance and is typically referred to as the overpotential required to produce a catalytic current

density of 10 mA cm^{-2} (j_{10}), and Tafel slope is used to evaluate the relationship between j and η. In general, overpotential η can be logarithmically correlated with j and is fit to the Tafel equation:

$$\eta = a + b \log j$$

where a is the intercept of the Tafel plot and b is the Tafel slope. From the Tafel equation, two important parameters can be determined, Tafel slope (b) and exchange current density (j_0). A Tafel slope demonstrates how fast the j can increase with a smaller voltage change, and an effective electrocatalyst usually features a lower overpotential and smaller slope. Besides, the value of the Tafel slope b provides insightful information toward the pathway and mechanism of catalysis, especially for elucidating the rate-determining step (RDS). The activity of electrodes strongly correlates with the physicochemical properties of the surface of electrocatalysts and the interaction between catalyst-modified electrodes and electrolytes. Currently, the best-known catalysts for the above-mentioned electrochemical reactions are precious-metal-based materials, such as Pt and Ir, which can deliver enough reaction rates as they require relatively low overpotential. However, the scarcity and relatively low stability greatly hinder their large-scale commercialization. Thus, the development of equally efficient and economical alternative electrocatalysts has become the focus and frontier of clean energy research.

To effectively replace precious-metal-based catalysts, considerable research efforts have been devoted to non-metal catalysts and low-content noble metal catalysts.[10] There is a gradual shift of research paradigm from materials discovery and property characterization toward materials engineering and property tuning for practical electrocatalysis applications. To maximize the electrocatalytic activity of catalysts, aside from the composition design of electrocatalysts, high active-site accessibility, micro/nanoarchitectures, and high electrical conductivity are all indispensable factors for

the materials design electrocatalyst. Nevertheless, most reported electrocatalysts still suffer from self-agglomeration issues, resulting in a ‘dead’ zone with less active sites and unfavorable electron and mass transport.

Another common issue is the inferior electrical conductivity of electrocatalysts, which hinders the activities of many electrocatalysts by limiting the electron transport between electrodes and electrocatalysts. Many electrocatalysts, such as metal oxides, metal hydroxides, and perovskites, are semiconductors or insulators. Conventional strategies such as adding conductive supports usually are unable to give well-anchored particles, resulting in peeling off, agglomeration, and dissolution. In this regard, multi-dimensional interconnected networks with high porosity and robustness are critically needed to minimize the restacking issue for efficient electrocatalysis.

An overview of this dissertation concerning the dual-tuning strategy combining structural design and electronic tuning of non-noble-metal-based electrocatalysts is briefed as follows. To push the electrocatalytic activity of non-noble meal-based catalysts to meet the requirement of practical applications, strategies including structural design and electronic tuning are applied to transition meta-based nanomaterials, to obtain both efficient and stable electrocatalysts with high active-site accessibility, micro/nanostructures, desirable electrical conductivity, and optimized adsorption. The general experimental methods and characterizations will be described in Chapter 2.

Chapter 3 begins with an introduction of pore engineering, an effective structural design for electrochemical storage and conversion, in the 2D mixed transition metal-based electrocatalysts. Pore/holey engineering offers larger active surface areas and abundant active sites for the adsorption of reactants, to alleviate the restacking issue of the isolated 2D nanomaterials and further facilitate the ion transfer. For another, many electrocatalysts are insulators or semiconductors, such as oxides, hydroxides, and perovskites,[11] which may

inhibit the electron transfer during the electrochemical process. It is critical to apply structural engineering and electronic modification to improve both mass transfer and charge transport in 2D electrocatalyst.

In Chapter 4, gel-based materials, as promising electrocatalysts possessing enhanced mass/charge transfer, are discussed. Conventional electrocatalysts prepared from bulky powders typically suffer from drastic problems on electrolyte penetration and electron transports. The family of gel materials recently provides exciting opportunities for advanced energy conversion technologies, due to their interconnected porous architectures, compositional and structural tunability, ease of functionalization, and high wettability for ion transfer. More intriguingly, gel materials can host other functional materials, serving as an ideal platform to study the fundamental electrocatalytic mechanism and facilitate the electrochemical reaction kinetics.

Chapter 5 focused on the structural design and electronic modification of gel-derived electrocatalysts, especially gel-derived alloys. Many gel-derived frameworks exhibited high catalytic activities for various electrochemical reactions, owing to their optimized composition design, and unique hierarchical structures inherited from nanostructured gels. More importantly, by introducing functional dopants in gels or gel-derivatives, the electronic structure of catalysts can be tailored.

Finally, in Chapter 6, a brief summary of this dissertation is provided, together with possible future work based on previous research works on 2D porous nanosheets and gel-based electrocatalyst and ongoing efforts on more efficient electrochemical energy conversion process.

Chapter 2: General experimental procedures

2.1 MATERIALS SYNTHESIS

The synthesis of non-noble metal-based electrocatalyst in this dissertation is based on the bottom-up methods from zero-dimensional (0D) building blocks. The detailed synthesis and fabrication procedures of the 2D nanomaterials studied in this dissertation are described in each of the following chapters.

2.2 MATERIALS CHARACTERIZATIONS

The general physical and chemical properties of the materials employed in the experiments were characterized by the following techniques. The specific characterization procedures will be described in each chapter.

2.2.1 Scanning electron microscopy

Morphologies and microstructures of the as-obtained samples were characterized with a scanning electron microscope (SEM) (Hitachi s-5500) equipped with a scanning transmission electron microscope (STEM). Dried powders were directly used for SEM characterizations. The STEM tests proceeded on a copper grid with deposition of 2D nanomaterial dispersion in ethanol.

2.2.2 Transmission electron microscopy

Morphologies and microstructures of the as-obtained samples were characterized with a high-resolution transmission electron microscope (TEM) (2010F, JEOL).

2.2.3 Energy-dispersive X-ray spectroscopy

Energy-dispersive X-ray spectroscopy (EDS or EDX) is used to identify the elemental composition and the element distribution of the studied materials. Both SEMs and TEM described in sections 2.2.1 and 2.2.2 are equipped with EDS/EDX.

2.2.4 Raman spectroscopy

Raman spectroscopy of the 2D nanomaterials with different chemical states was conducted with a Raman microscope (Renishaw in Via Raman microscope) with a 532-nm laser and a 2400 lines mm^{-1} grating stage at a 50X objective lens.

2.2.5 Fourier transform infrared spectroscopy

Fourier transform infrared spectroscopy (FTIR) data were obtained with KBr pellets with a PerkinElme Spectrometer (Thermo Mattson, Infinity Gold FTIR) equipped with liquid nitrogen cooled narrow band mercury cadmium telluride (MCT) detector, using an attenuated total reflection cell equipped with a Ge crystal. r IR spectrometer.

2.2.6 Ultraviolet-visible spectroscopy

Ultraviolet-visible (UV-Vis) spectroscopy data and reflectance were conducted using a UV-vis-NIR spectrometer (Cary 5000) with an integrating sphere unit and automation of reflectance measurement unit, and the measurements were corrected by baseline/blank correction with dark correction.

2.2.7 Temperature-dependent electrical resistance test

Temperature-dependent electrical resistance data were obtained by a physical property measurement system (PPMS-9, Quantum Design) using the four-point probe method under high vacuum conditions. Samples were cold-pressed (hydraulically) into pellets with a diameter of 3mm.

2.2.8 Brunauer−Emmett−Teller test

The specific surface area was measured using a Nova 2000 v.6.11 instrument (Quantachrome Instruments, Boynton Beach, FL, USA). The weighed powder was added to a 12 mm Quantachrome bulb sample cell and degassed for a minimum of 3 h. The sample was then analyzed by the NOVA Enhanced Data Reduction Software v. 2.13 using the BET theory of surface area.

2.2.9 Thermogravimetric analysis

Thermogravimetric analysis (TGA) was performed with a PerkinElmer TGA4000 thermogravimetric analyzer from 30 to 900 °C with a ramping rate of 5 °C min^{-1} under air.

2.3 ELECTROCHEMICAL MEASUREMENTS

2.3.1 Electrode preparation

All electrochemical measurements performed on Ni foam electrode for HER and OER tests were under identical conditions with the same catalyst mass loading: 10 mg of catalyst and 100 µL of 5 wt% Nafion solution were dispersed in 0.9 mL ethanol solvent by 30 min

sonication to form a homogeneous ink. 50 μL of the catalyst dispersion (10.0 mg mL^{-1}) were then transferred onto the Ni foam electrode (NF, the pretreated Ni foam with a fixed area of 0.5 cm × 0.5 cm coated with water-resistant silicone glue, double-faced) *via* a drop-casting approach. The mass loading of catalyst on Ni foam is 1.0 mg cm^{-2}. Electrochemical measurements performed on glassy carbon electrode (GCE): 4 mg of catalyst and 40 μL of 5 wt% Nafion solution were dispersed in 1.0 mL ethanol solvent by 30 min sonication to form a homogeneous ink. 5 μL of the catalyst dispersion (4.0 mg mL^{-1}) were then transferred onto the GCE (or glassy carbon rotating disk electrode, RDE, 0.07 cm^2, 1600 rpm, Pine Research Instrumentation, USA). The mass loading of catalyst on GCE is 0.28 mg cm^{-2}.

2.3.2 Cyclic voltammograms and Linear sweep voltammograms

A three-electrode electrochemical cell was applied to perform all the electrochemical measurements, using a saturated Ag/AgCl electrode as the reference electrode, a Pt wire as the counter electrode, and the catalyst material modified glassy carbon (GC) electrode as the working electrode on a BioLogic Instrument (BioLogic VMP-3model). For the HER test, linear sweep voltammograms (LSV) polarization curves were obtained by sweeping the potential from 0 V to 0.8 V at a sweep rate of 5 mV s^{-1} in 1.0M KOH. For the OER test, cyclic voltammograms (CVs) were performed at a scan rate of 50 mV s^{-1} from 0~0.8V (vs. saturated Ag/AgCl electrode). After CV activation for 20 cycles, LSV polarization curves were obtained by sweeping the potential from 0 V to 0.8 V at a sweep rate of 5 mV s^{-1} in 1.0 M KOH solution, corrected by 95% IR-correction.

2.3.3 Electrochemical impedance spectroscopy

Electrochemical impedance spectroscopy (EIS) experiments were carried out at applied potential in the specific frequency range. The equivalent circuit is typically comprised of a resistor (R_s) in series with two parallel combinations of resistors and a constant phase element (CPE). The equivalent circuit can fit the EIS data, regarded as the semicircles in both high- and low-frequency range. Resistors (Ohmic resistance R_s and charge transfer resistance R_{ct}) are well-correlated to electrocatalytic kinetics, attributed to the R_s arising from the electrolyte and all contact, and R_{ct} at the interface between the catalysts and the electrolyte, respectively. It is generally believed that values of R_s correspond to the degree of contact between the current collector and catalysts and that the values of R_{ct} represent the charge transfer kinetics.

2.3.4 Electrochemical surface area

Electrochemical active surface area (ECSA) can be obtained by converting specific capacitance value for a flat standard with 1 cm^2 of real surface area. The double-layer capacitance is obtained by CV curves at different scan rates and plotting charging current density differences against scan rates. The specific capacitance for a flat surface is generally considered to be in the range of 20-60 μF cm^{-2}. Here we use 40 μF cm^{-2}.

2.3.5 Cycling test and stability test

For the chronoamperometric test, a static overpotential was fixed for a certain time during the continuous electrocatalytic process to obtain the curve of the time dependence of the current density. The chronopotentiometric measurement was performed at a current density of 10 mA cm^{-2}.

Chapter 3: Pore engineering and anion effect in 2D mixed-transition-metal-based electrocatalysts for water splitting[1]

3.1 INTRODUCTION TO 2D MATERIALS

Fabrication of single- and few-layered two-dimensional (2D) nanomaterials has shown promise in improving the catalytic activities given that 2D structure significantly increases the electrochemically active area due to their high surface areas and abundant edge sies.[12, 13] Compared to the bulk materials, nanomaterials with particle sizes ranging from several to hundreds of nanometers possess significantly enlarged specific surface areas for electrolyte diffusion and abundant active sites for the adsorption of reactant molecules.[14-16] Owing to the unique 2D structure and a large degree of anisotropy, 2D nanomaterials with thickness down to a few nanometers exhibit large specific surface areas due to the high aspect ratio and provide abundant unsaturated atoms with dangling bonds as active sites.[17, 18] The past decade has witnessed the emergence of graphene and various graphene-like 2D materials, such as layered oxides,[19] transition metal chalcogenides,[20] MXenes[21]. 2D nanocrystals offer exciting opportunities for both fundamental studies and technological applications due to their unique and fascinating properties.

However, irreversible restacking of 2D nanosheets (NSs) during the processing and fabrication results in the decreased surface area and elongated electrolyte diffusion pathway, which is still a significant challenge to date.[22] Moreover, most 2D electrocatalysts

---

[1]**Z. Fang**, L. Peng, Y. Qian, X. Zhang, Y. Xie, J. Cha, G. Yu, "Dual Tuning of Ni-Co-A Nanosheets by Anion Substitution and Holey Engineering for Efficient Hydrogen Evolution", ***J. Am. Chem. Soc.*** 2018, 140, 5241.

Z. Fang, L. Peng, H. Lv, Y. Zhu, C. Yan, S. Wang, P. Kalyani, X. Wu, G. Yu, "Metallic Transition Metal Selenide Holey Nanosheets for Efficient Oxygen Evolution", ***ACS Nano*** 2017, 11, 9550.

Z. Fang†, L. Peng†, J. Li†, L. Wang, A. Bruck, Y. Zhu, K. Takeuchi, A. Marschilok, E. Stach, E. Takeuchi, G. Yu, "2D Holey Nanoarchitectures Created by Confined Self-Assembly of Nanoparticles via Block Copolymers", ***ACS Nano 2018,*** 12, 820.

Z. Fang†, L. Peng†, Y. Zhu†, C. Yan, G. Yu, "Holey Two-Dimensional Nanomaterials for Electrochemical Energy Storage", ***Adv. Energy Mater. 2018,*** *8*, 1702179.

Z. Fang participated in the experimental work and the preparation of manuscripts.

are insulators or semiconductors, such as oxides, hydroxides, and perovskites,[11] which may inhibit the electron transfer during the electrochemical process. It is critical to apply structural engineering and electronic tuning to improve both mass transfer and charge transport in 2D electrocatalyst.

Recent development in heterogeneous catalysis recognizes the importance of active sites and their surrounding microenvironments, which can modulate the reaction chemistry and hence influence the catalytic properties.[23-25] Several effective strategies for engineering 2D nanomaterials to achieve significantly improved properties for energy storage and conversion technologies are shown in Figure 3.1.[23] Conventional aspects of materials engineering, such as phase tuning, defect engineering, heteroatom doping, and their applications in 2D nanomaterials have been largely reported before. Other strategies in structural engineering of 2D nanomaterials based on their unique structural features include surface modification, architecting interconnected networks, and pore engineering. These strategies benefit from both classic 2D intercalation chemistry for exploring interlayer space, and state-of-the-art nanotechnology involving the formation of holey/porous structures and construction of heterostructures.

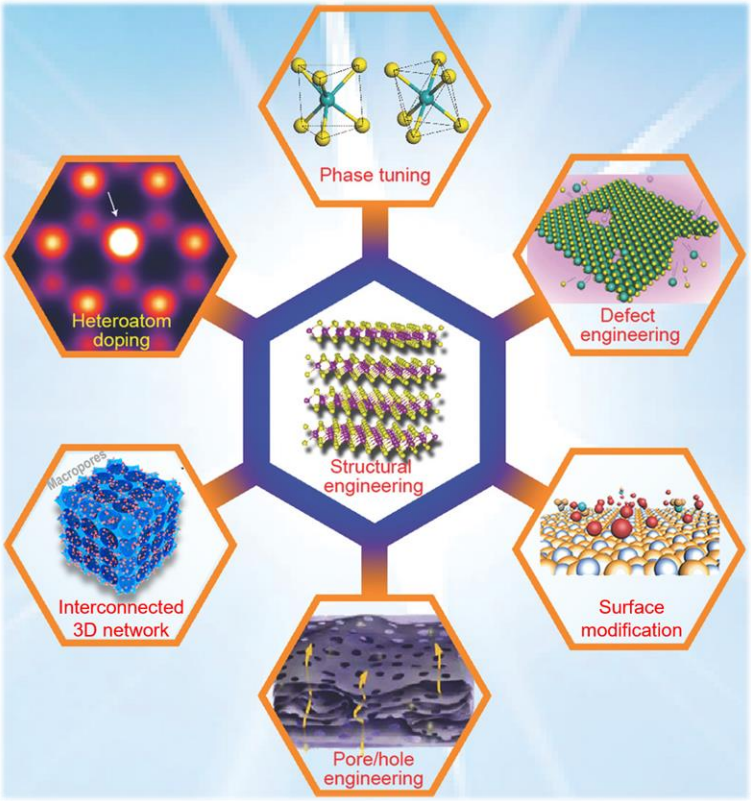

Figure 3.1: Some typical strategies of design 2D nanomaterials for improved electrochemical properties.

3.2 MATERIALS SYNTHESIS AND CHARACTERIZATION DETAILS

3.2.1 Synthesis of graphene oxide (GO) nanosheets

Graphene oxide (GO) was synthesized from purified natural graphite by a modified Hummers' method. Simply, 10 g of graphite powder was first added to 15 mL of concentrated H_2SO_4. 5 g of $K_2S_2O_8$ and 5 g of P_2O_5 were then added slowly. The as-obtained mixed solution was heated to 80 °C and maintained at this temperature for 6 h. After cooling to room temperature, the resultant was carefully diluted with distilled water, filtered, and washed on the filter until the rinse water pH became neutral. The product was dried in air at ambient

temperature overnight. Then the pre-oxidized graphite was added to 230 mL of concentrated H_2SO_4 cooled in an ice-water bath. 30 g of $KMnO_4$ was added very slowly into the mixture with stirring and cooling. All the operations were carried out very slowly in a fume hood. The mixture was then stirred at 35 °C for 30 min. 460 mL of distilled water was slowly added to cause an increase in temperature to 98 °C and the mixture was maintained at that temperature for 15 min. The reaction was terminated by adding 1.4 L of distilled water followed by 10 mL of 30% H_2O_2 solution. The solid product was separated by centrifugation, washed repeatedly with 5% HCl solution, and then dialyzed for a week.

3.2.2 Synthesis of $NiCo(OH)_x$/rGO hybrid

0.4 mg/mL of GO suspension was synthesized by adding 30 mg of GO into 75 mL EG and was ultrasonicated for 2 h. After 0.5 mmol $Ni(Ac)_2 \cdot 4H_2O$ and 1.0 mmol $Co(Ac)_2 \cdot 4H_2O$ were added to 25mL EG, Ni^{2+} /Co^{2+} mixed solution was added to GO suspension and refluxed at 170 ℃ for 2 h. After the reaction, the final products were centrifuged at 7800 rpm for 10 min, and washed with water and ethanol. The hybrid intermediate was dried by the freeze-drying method. All chemicals were used without further purification and purchased from commercial sources.

3.2.3 Synthesis of $NiCoO_x$ holey nanosheets

$NiCo(OH)_x$/rGO hybrid intermediate is annealed at 400 ℃ in the air for 2 h with a heating rate of 0.5 ℃ min^{-1} from room temperature, and the final product is $NiCo_2O_4$ (NCO). The synthesis of NCO holey nanosheets with different Ni/Co ratios was similar to that of the NCO holey nanosheets except for the different amounts of $NiAc_2$ and $CoAc_2$ before the reaction.

Samples	$Ni(Ac)_2 \cdot 4H_2O$ / mmol	$Co(Ac)_2 \cdot 4H_2O$ / mmol	Molar ratio of Ni in oxide (Ni/Ni+Co)/%
Co_3O_4	0	1.5	0
$NiCo_2O_4$	0.5	1.0	33
$NiCoO_x$	0.75	0.75	50
$Ni_2Co_1O_x$	1.0	0.5	67
NiO	1.5	0	100

Table 3.1: Synthesis of NCO holey nanosheets with different Ni/Co ratios in the precursor.

3.2.4 Synthesis of $Ni_xCo_{3-x}Se_4$ Holey Nanosheets

$NiCo_2Se_4$ (NCS) holey nanosheets were synthesized by a solution-based phase transformation: 0.04mmol oxide precursor (around 10mg) was added into 25mL EG was ultrasonicated for 2h, and 0.20mmol Na_2SeO_3 (around 29mg, a little excess) was dissolved into 15mL EG. And then $NiCo_2O_4$ EG dispersion was added to Na_2SeO_3 EG solution under vigorous stirring. After dropping 1mL N_2H_4 into the solution, the mixture was refluxed at 180°C for 2 h. The possible transformation reactions are as follows:

$$SeO_3^{2-} + N_2H_4 = Se + N_2 + 2OH^- + H_2O$$

$$Se + 6OH^- = 2Se^{2-} + SeO_3^{2-} + 3H_2O$$

$$2Co^{3+} + N_2H_4 + 2OH^- = 2Co^{2+} + N_2 + 2H_2O$$

$$Se + 3Se^{2-} + Ni^{2+} + 2Co^{2+} = NiCo_2Se_4$$

Due to the smaller size and high surface area of nanoparticles, the transformation reaction for holey nanosheets is easier compared with the bulk phase, Synthesis of other selenides is similar to that of the NCS holey nanosheets except for the oxide precursor with a different composition.

3.2.5 Synthesis of NiCoP holey Nanosheets

NiCoP (NCP) holey nanosheets were synthesized by a chemical vapor deposition phase transformation: 0.04mmol oxide precursor(~10mg) and 264mg $NaHPO_2 \cdot H_2O$ (molar ratio: ~1:30) are placed at two porcelains. NaH_2PO_2 at the upstream side of the furnace. Subsequently, the samples were heated at 300°C for 2 h with a heating speed of 10 °C min^{-1} in Ar atmosphere. The product was collected after cooled to ambient temperature under Ar. The possible transformation mechanism:

$4NaH_2PO_2 \cdot H_2O = 2PH_3 + 5H_2O + Na_4P_2O_7$ (Decomposition, T >250℃）

$PH_3 + NiCo^{(II,III)}O_x \rightarrow NiCo^{(II)}O_2 + P + H_2O$ (Reduction)

$4PH_3 + 3NiCoO_2 = 3NiCoP + P + 6H_2O$ (Phosphidation)

The synthesis of other phosphides is similar to that of the NCP holey nanosheets except for the oxide precursor with a different composition.

3.2.6 Materials characterization

Powder XRD patterns were collected on a Philips Vertical Scanning diffractometer to identify the phase of the as-synthesized samples. SEM, EDX, STEM, and TEM were used to characterize the morphology of the samples. For electrical transport property measurement, holey nanosheet powders were cold-pressed into pellets with a diameter of

3mm by a physical property measurement system using a four-point probe method under high vacuum conditions.

3.2.7 Electrochemical measurement and calculation

All of the HER measurements performed on Ni foam electrodes were under identical conditions with the same catalyst mass loading: 10 mg of catalyst and 100 μL of 5 wt% Nafion solution were dispersed in 0.9 mL ethanol solvent by 30 min sonication to form a homogeneous ink. 50 μL of the catalyst dispersion (10.0 mg mL^{-1}) were then transferred onto the Ni foam electrode (NF, the pretreated Ni foam with a fixed area of 0.5 cm × 0.5 cm coated with water-resistant silicone glue, double-faced) *via* a drop-casting approach. The mass loading of catalyst on Ni foam is 1.0 mg cm^{-2}. The HER measurements performed on glassy carbon electrode (GCE) were also under identical conditions with the same catalyst mass loading: 4 mg of catalyst and 40 μL of 5 wt% Nafion solution were dispersed in 1.0 mL ethanol solvent by 30 min sonication to form a homogeneous ink. 5 μL of the catalyst dispersion (4.0 mg mL^{-1}) were then transferred onto the glassy carbon rotating disk electrode (RDE, 0.07 cm^2, 1600 rpm, Pine Research Instrumentation, USA) *via* a controlled drop-casting approach.

All the electrochemical measurements for the HER and OER test were conducted in a three-electrode electrochemical cell using saturated Ag/AgCl electrode as the reference electrode, a platinum wire as the counter electrode and the sample modified glassy carbon electrode as the working electrode on a BioLogic Instrument (BioLogic VMP-3model). For the HER test, linear sweep voltammograms (LSV) polarization curves were obtained by sweeping the potential from 0 V to 0.8 V at a sweep rate of 5 mV s^{-1} in 1.0M KOH. For the OER test, cyclic voltammograms (CVs) were performed at a scan rate of 50 mV s^{-1}

from 0~0.8V (vs. saturated Ag/AgCl electrode). After CV activation for 20 cycles, LSV polarization curves were obtained by sweeping the potential from 0 V to 0.8 V at a sweep rate of 5 mV s^{-1} in 1.0 M KOH solution, corrected by 95% IR-correction. For the chronoamperometric test, a static overpotential was fixed for a certain time during the continuous electrocatalytic process to obtain the curve of the time dependence of the current density. The chronopotentiometric measurement was performed at a current density of 10 mA cm^{-2}.

The potentials were converted to a reversible hydrogen electrode (RHE) scale according to the Nernst equation:

$$E_{RHE} = E_{Ag/AgCl} + 0.059\ pH + 0.197$$

the overpotential (η) was calculated according to the following formula:

$$\eta\ (V) = E_{RHE} - 1.23\ V.$$

The values of TOF (turnover frequency) were calculated by assuming that every atom (Ni, Co, P) is involved in the catalysis (lower TOF limits were calculated):

$$TOF = \frac{j \times A}{2 \times F \times n}$$

where j (mA cm^{-2}) is the measured current density at η = 200 mV, A (0.5 cm^{-2}) is the geometry surface area of Ni foam electrode, the number 2 means 4 electrons mol^{-1} of O_2, F is Faraday's constant (96485C mol^{-1}), and n is the moles of coated metal atom on the electrode calculated by assuming the sample is composed of solid 10 nm particles.[26]

3.3 RESULTS AND DISCUSSION

3.3.1 Pore engineering in 2D nanostructured Ni/Co-oxide/selenide/phosphide

Although possessing many advantages for the electrochemical energy conversion process, 2D nanomaterials still suffer from several severe problems when utilized in

practical energy conversion devices. For example, when fabricated into electrodes for practical applications, the isolated single- or few-layered nanosheets tend to restack into densely packed structures or films, which will lead to drastically decreased active surfaces and prolonged ion diffusion pathways during the reactions.

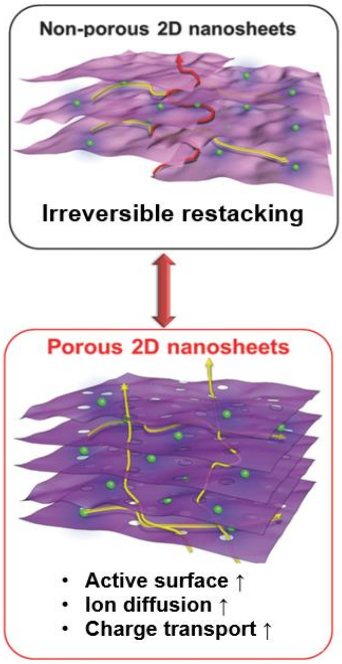

Figure 3.2: Schematic illustration of the key features of 2D holey structures during the electrochemical process.

Over the past decade, porous nanomaterials with unique surface structures and morphological stability have found promising applications in energy storage, catalysis, sensors, water purification, and gas separation and storage. Porous/holey nanomaterials, sparked by their interconnected open structures and structural stability, can alleviate the restacking issue of nanomaterials, enable faster ion transport into the inner structure of the electrodes, and improve ion transport kinetics. Thus, by integrating the advantages of 2D architecture and porous structure, porous 2D nanomaterials may offer a number of

structural advantages for efficient electrochemical energy conversion applications, compared to the 2D nanosheets with smooth and flat surfaces (Figure 3.2). First, the porous 2D nanostructures provide large effective surface areas and abundant active sites for electrochemical reactions, favorable for the adsorption of reactants. Second, porous 2D nanomaterials ensure the effective wetting and penetration of electrolyte to the electrode surface, facilitating rapid ion/charge transfer across the electrode-electrolyte interface during the heterogeneous catalysis. Third, porous 2D nanomaterials can also alleviate the restacking issue of the isolated 2D nanomaterials, considering the internal open structures generated in porous nanomaterials are able to open up the blocked active surfaces for improved mass transfer. Even though ions can diffuse in the vertical direction near the edge or junction of nonporous nanosheets (indicated by the red and yellow arrow in Figure 3.2), the length of the ion diffusion pathway becomes much longer than that of ion diffusion directly through the porous nanosheets. In this regard, holey/porous nanomaterials possess more active sites and a continuous mass/charge transport pathway.

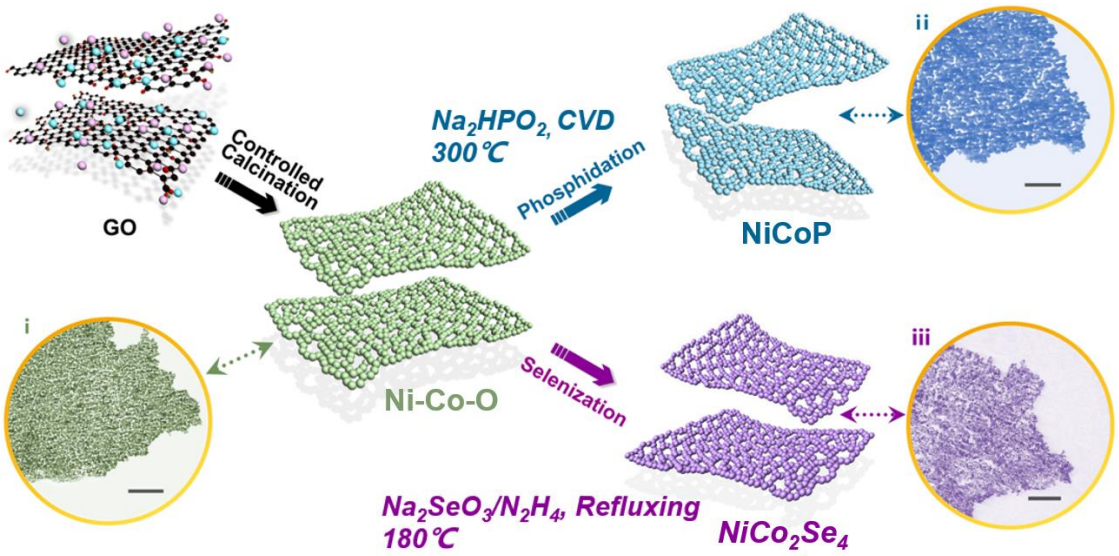

Figure 3.3: Scheme of synthesis of Ni/Co-based oxide/selenide/phosphide holey nanosheets

The scheme of synthetic process of mixed-transition-metal (MTM)-based oxide/selenide/phosphide 2D holey nanosheets is demonstrated in Figure 3.3. Unlike classical layered transition metal dichalcogenides, the preparation of Ni/Co-selenide and phosphide nanosheets, due to the relatively strong bonds between the layers, remains a great challenge. $NiCo_2O_4$ (NCO) holey nanosheets are first obtained via a template-directed approach based on GO nanosheets followed by controlled calcination. GO nanosheets serve as flexible 2D substrates for uniform anchoring of metal ions. After the calcination, 2D holey oxides composed of the interconnected nanoparticles (8−12 nm) were obtained, and meanwhile the rGO was removed. The synthesis of selenide and phosphide can be synthesized through the transformation process from the oxide precursor.

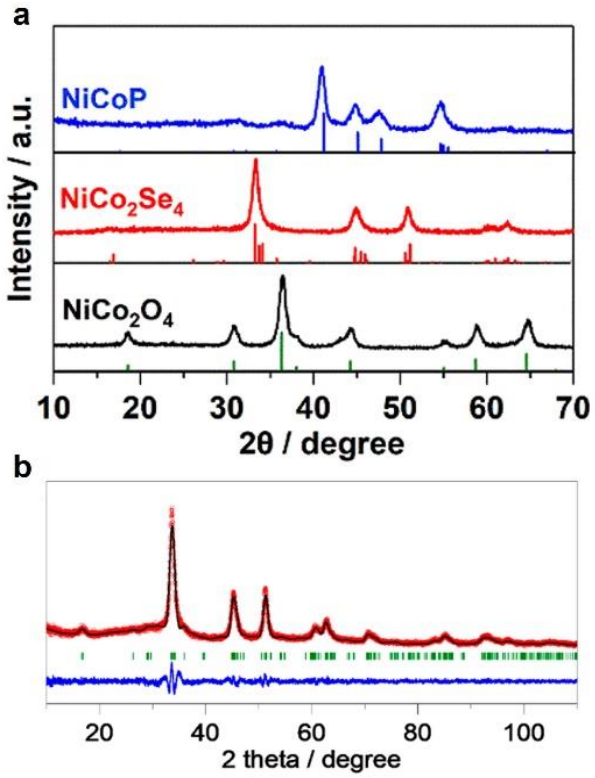

Figure 3.4: XRD of a series of Ni/Co-based holey nanosheet samples and Rietveld refinement of the XRD data of $NiCo_2Se_4$ (black line, data points; red line, calculation line; green vertical line, marker points; blue line, difference line).

The phase purity of the series of Ni/Co-based electrocatalysts is first characterized by X-ray diffraction (XRD, Figure 3.4a). The peak positions of the XRD patterns of the as-prepared NCA (A=O, Se, P) holey nanosheets match well with those of the standard PDF cards. The phase purity of $Ni_xCo_{3-x}Se_4$ indicates the pure monoclinic selenide phases (except for $Ni_{1-y}Se$ with hexagonal NiAs structure) are formed. Figure 3.4b shows the XRD patterns and corresponding Rietveld analysis of the NCS sample.

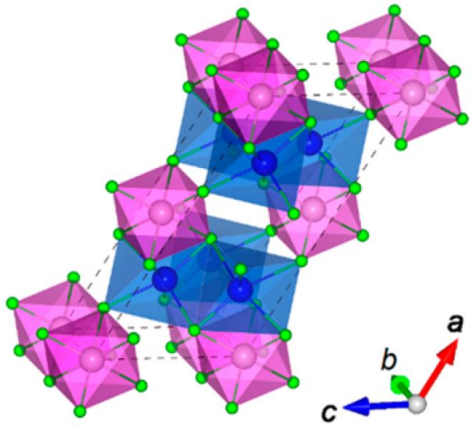

Figure 3.5: Crystal structure of $NiCo_2Se_4$ showing a monoclinic structure.

Figure 3.3 inset i shows the scanning transmission electron microscopy (STEM) image of the 2D oxide holey nanosheet precursor, consisting of interconnected nanoparticles (5−10 nm) with no obvious aggregation. Holey architecture in NCS and NCP is inherited from the NCO holey nanosheet precursor. According to the microscopic images, the holey nanostructure can be maintained after phase transformation (ii and ii in Figure 3.3, Figure 3.6). The lateral size of the nanosheets is between 2 and 3 μ m, and the thickness is around 20 nm, made up of interconnected nanoparticles (about 15 nm) with no obvious aggregation. The average diameter of holes is about 15 nm. Notably, this route can

be generally applied to other metal selenides (such as Co_3Se_4, NiSe, etc.) and phosphides (including CoP, Ni_2P).

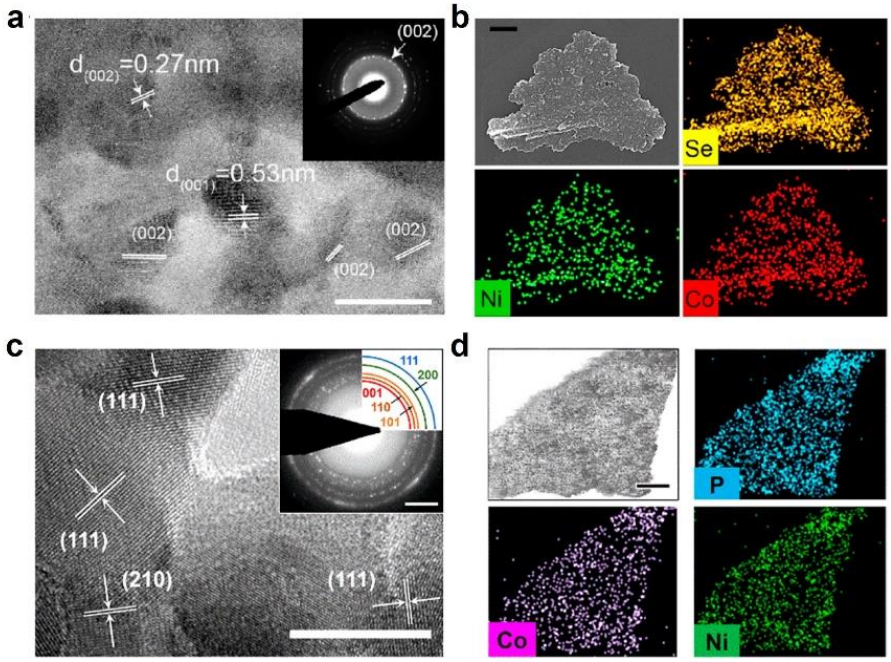

Figure 3.6: (a) HRTEM and SAED of a NCS holey nanosheet. (b) EDX images of NCS holey nanosheets. (c) HRTEM and SAED of a NCP holey nanosheet. (d) EDX images of NCP holey nanosheets. Scale bars: (a) 20 nm, (b) 200 nm, (c) 10 nm, 10 nm^{-1} in the inset of (c), (d) 200nm.

The high-resolution transmission electron microscopy (HRTEM) image in Figure 3.6a shows that the clear lattice fringes of 0.27 and 0.53 nm correspond well to the (002) and (001) facets of the monoclinic NCS, respectively. The diffused concentric rings displayed in the selected area electron diffraction (SAED) pattern (Figure 3.6a inset) indicate the polycrystalline structure. The diffraction rings can be indexed to monoclinic NCS, in agreement with the XRD analysis. Similarly, the HRTEM image of NCP holey nanosheets in Figure 3.6c, shows that the clear lattice fringes correspond well to the (111),

(210), and (300) facets of the hexagonal NCP, respectively, while the SAED pattern (Figure 3.6c, inset) also shows a diffuse set of concentric rings, demonstrating the formation of polycrystalline structure. Moreover, energy-dispersive X-ray spectroscopy (EDX) analysis (Figure 3.6b and d) confirms the uniform distribution of Ni, Co, and Se in NCS, Ni, Co, and P in NCP, respectively, and the formation of bimetallic selenide/phosphide.

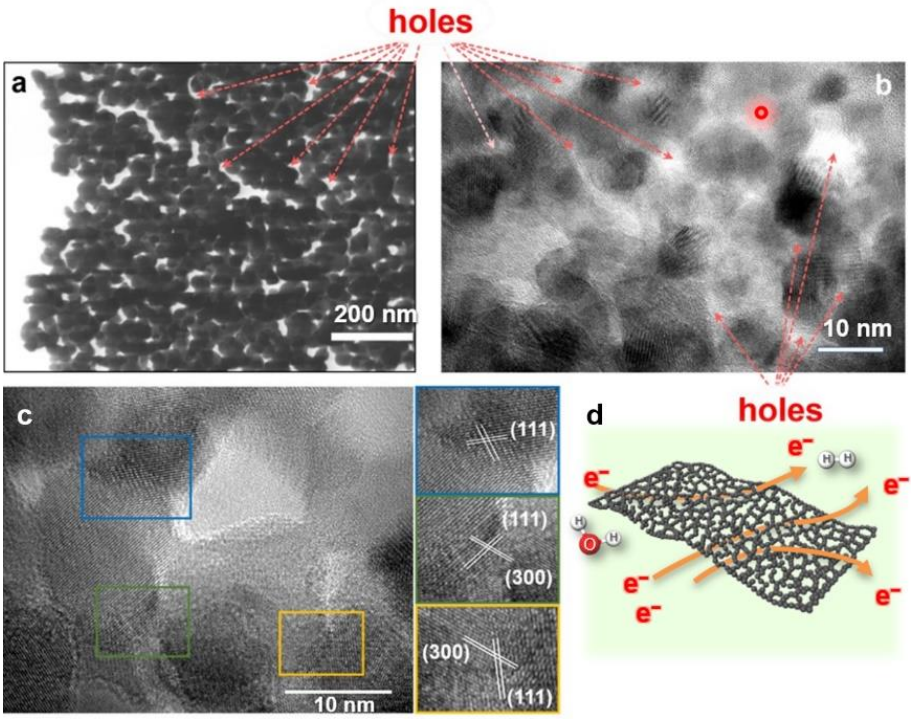

Figure 3.7: Chemically interconnected nanoparticles in holey nanosheet: (a)(b) TEM images and (c) HRTEM images of the holy structure. (d) Hole structures for enhanced mass and charge transfer during electrocatalysis.

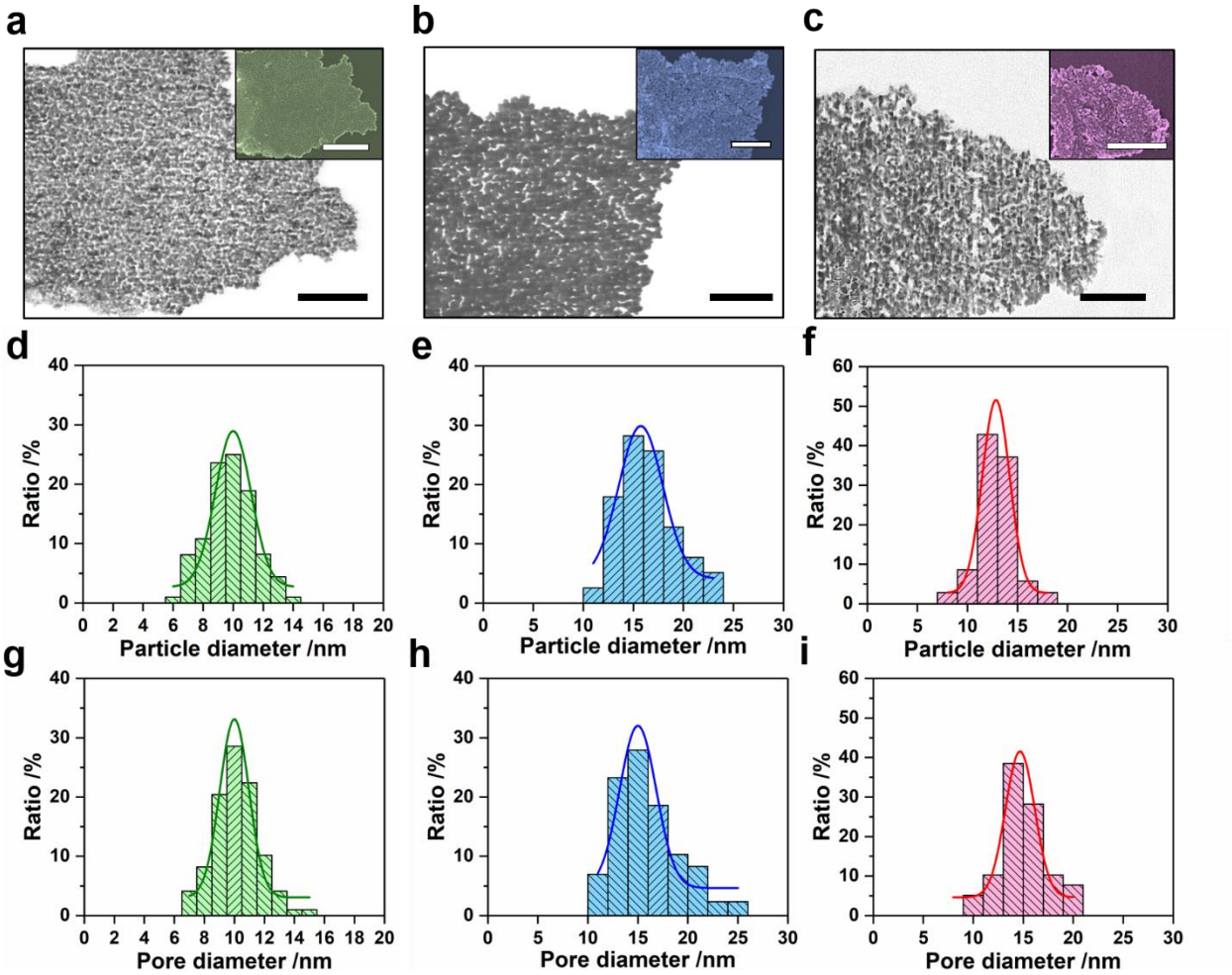

Figure 3.8: STEM and SEM (inset) images of (a) NCO, (b) NCP and (c) NCS holey nanosheets (scale bar: 200 nm, inset: 500 nm). Particle size distribution in (d) NCO (8-12 nm) (e) NCP (12-18 nm) and (f) NCS (10-15nm) holey nanosheets. Hole size distribution in (g) NCO (8-12 nm) (h) NCP (12-18 nm) and (i) NCS (12-18 nm) holey nanosheets.

The particle distribution and pore distribution of NCO, NCP, and NCS are measured from TEM images, as shown in Figure 3.8. Particle size distribution of NCO (8-12 nm) in Figure 3.8d, NCP (12-18 nm) in Figure 3.8e, and NCS (10-15nm) in Figure 3.8f holey nanosheets are similar even after phase conversion. Holey selenide and phosphide

nanosheets possess relatively larger particles size than oxide precursors owing to the partial fusion of particles during the phase conversion from holey oxides.

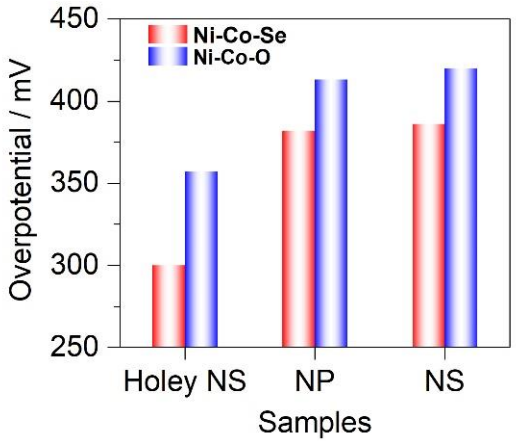

Figure 3.9: Comparison of overpotentials requires j = 10 mA cm^{-2} of NCS and NCO with different morphology in 1.0 M KOH.

To verify that 2D holey nanosheets could serve as an effective structure for electrocatalytic oxygen evolution, I compare the OER performance of as-prepared oxide and selenide holey nanosheets with other reference samples, including nanoparticles (NP) and nanosheets with no holes (NS). The electrodes are first activated in O_2-saturated 1.0 M KOH aqueous electrolyte at a scan rate of 50 mV s^{-1}. Figure 3.9 shows that the overpotentials of both selenide and oxide require lower overpotential to reach the current density of 10 mA cm^{-2}, compared with other control samples. NCS holey nanosheets require an overpotential of only 300 mV, which is around 80 mV lower than that of the NCS NPs. NCS NSs exhibit inferior electrocatalytic activity with an overpotential of 385 mV. We can learn from the improved activity of holey nanocatalysts that pores/holes can alleviate the restacking issue of nanomaterials, enable faster ion transport into the inner structure of the electrodes, and improve ion transport kinetics.

3.3.2 Metallic $NiCo_2Se_4$ holey nanosheets for electrocatalytic oxygen evolution

To design highly efficient electrocatalysts, catalyst materials must possess abundant active sites for adsorption/desorption, desirable electrical conductivity for fast charge transport, and robust structure for long-term electrocatalysis. For instance, to improve the electron transfer in oxides, spinel Co_3O_4 nanocrystals grown on N-doped graphene exhibit high OER activities in alkaline solution, due to electrical coupling effects between wide-band-gap semiconducting Co_3O_4 and conductive graphene. However, low intrinsic electrical conductivity still hinders the fast electron transport, leading to poor O_2 generation kinetics. To date, considerable efforts have been made to tune the physical and chemical properties for improved electrocatalytic characteristics. Strategies such as heterometal doping and surface treatment have been successfully applied to enhance electrocatalytic activity.[27-29] For instance, mixed-metal oxides have shown improved electrocatalytic properties due to the introduction of heteroatoms, offering enhanced charge transfer between different ions to lower the energy barrier.[29] Typically, some transition metal chalcogenides and phosphide may possess metallic characteristics due to their unique metal-anion bonding. Here I try to introduce metallic characteristics into transition metal compounds to improve their intrinsic electric conductivity and boost the electron transfer during the electrochemical reaction.

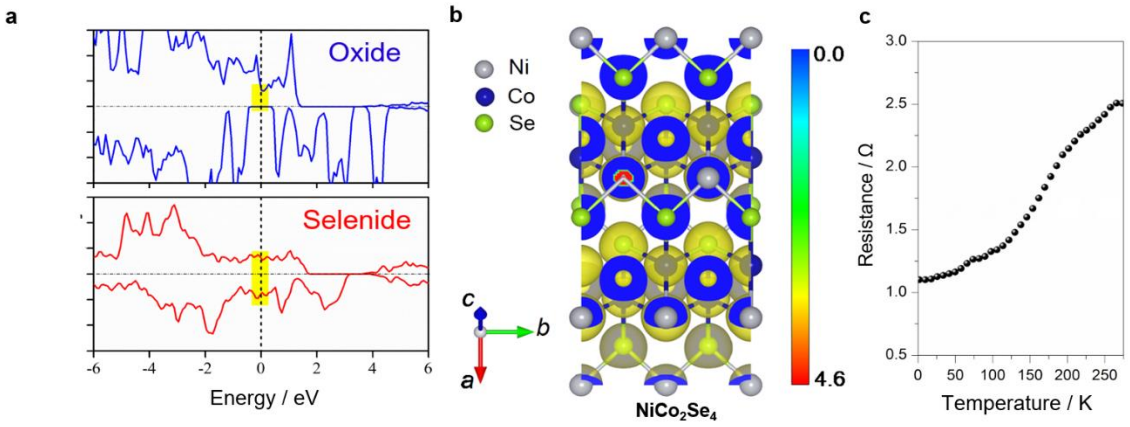

Figure 3.10: (a) Density of states (DOS) of Ni/Co-oxides (NCO) and selenides (NCS) across the Fermi level. (b) Charge density wave (isosurface: 0.07 e/Bohr3) and (c) Temperature-dependent electrical resistance of NCS.

DFT calculation (Figure 3.10a and b) reveals that the density of states (DOS) of selenide across the Fermi level is more intense than that of oxides. This suggests the electrical property of selenides, in particular, the carrier concentration and electrical conductivity, can be enhanced when transformed from oxides to selenides. The metallic behavior of NCS can be further revealed by a temperature-dependent electrical resistance test (Figure 3.10c), where the electrical resistance of NCS keeps increasing as temperature increases, displaying the metallic feature. Previous studies uncovered the metallic behavior for the $A_xB_{3-x}X_4$ (A, B = Fe, Co, Ni...; X = S, Se, Te) compounds, which could correspond to partially filly bands formed as a result of d electron delocalization. Goodenough proposes a model to interpret the electrical properties of AB_2X_4, which includes both direct cation t_{2g} interaction and indirect interactions between cation e_g and anion s, p_σ orbitals. In this regard, metallic NCS is able to facilitate the electron transfer between the surface of the catalyst and current collector, beneficial for electrocatalytic water oxidation kinetics.

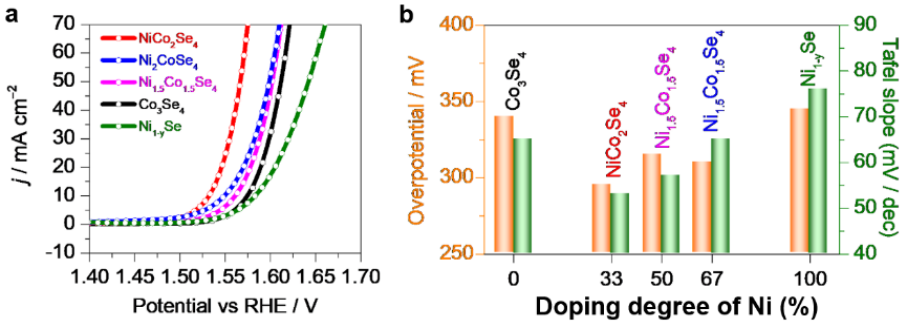

Figure 3.11: (a) 95% IR-corrected polarization curves, (b) overpotential @ 10 mA cm^{-2} and Tafel slop of NCS holey nanosheets with different compositions heteroatom doping degree.

To further investigate the effect of composition on electrocatalytic properties for oxygen evolution, I also evaluate the OER performance of as-obtained ternary selenide holey nanosheets with different Ni/Co ratios, and commercial RuO_2 electrocatalyst. The polarization curves of Ni/Co selenides with different Ni:Co ratios in 1.0 M NaOH are demonstrated in Figure 3.11a. Binary selenide Co_3Se_4 and $Ni_{1-y}Se$ exhibit inferior electrocatalytic activity with the overpotentials of 349 and 345 mV, respectively. Remarkably, after the introduction of heteroatom, the catalytic activities of ternary metal selenides are improved. All Ni-Co mixed selenide catalysts deliver a desirable catalytic activity for oxygen evolution with the overpotential of 295−310 mV (Figure 3.12b). Among them, $NiCo_2Se_4$ yields the highest activities with the lowest operation overpotential of 300 mV after 20-cycled activation. The corresponding Tafel slopes of ternary selenides are between 50 and 60 mV/dec, smaller than that of Co_3Se_4 (65 mV/dec) and $Ni_{1-y}Se$ (76 mV/dec), indicating faster OER kinetics can be achieved in applications using mixed selenide holey nanosheets. The performance difference between bimetal selenides and

monometal selenides primarily derives from the synergistic effect of Co and Ni, due to their modified electronic structure and mixed-valence state in bimetal compounds.

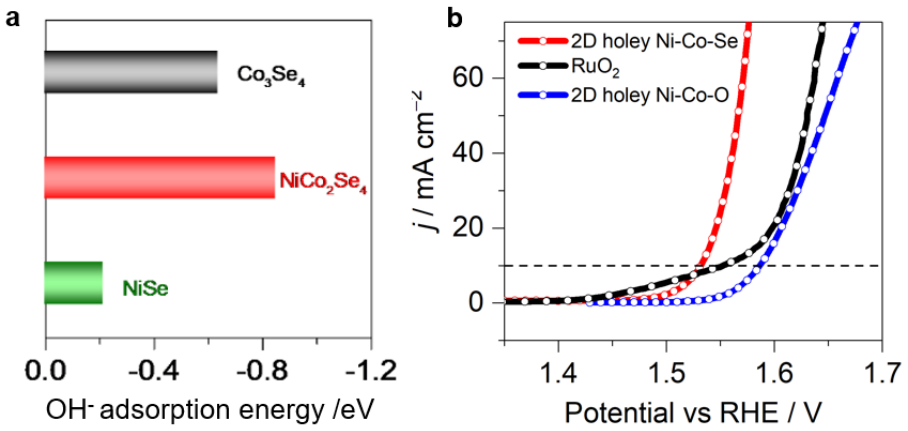

Figure 3.12: (a) OH^- adsorption energy of Co_3Se_4, $NiCo_2Se_4$, and NiSe (010) facets. (b) 95% IR-corrected polarization curves of a series of $NiCo_2Se_4$, $NiCo_2O_4$, and RuO_2.

We further applied DFT simulation modeling to calculate the hydroxide adsorption energy of catalysts in an alkaline medium (Figure 3.12a). It is generally accepted that hydroxyl ions (OH^-) are firstly adsorbed on the surface of selenide catalysts during the OER process in basic media. Generally, the adsorption energy of OH− molecules plays an essential role in the OER activity.[30] Large adsorption energy is in favor of the decomposition of reactant, the formation of an O_{ads} intermediate ($OH_{ads} \rightarrow O_{ads} + H^+ + e^-$), and the overall reaction kinetics. To investigate the synergistic effect of Ni/Co on adsorption energy of OH−, the (010) facet of NCS holey nanosheets is chosen as the surface model. In Figure 3.12a, it is clear that ternary NCS holey nanosheets possess adsorption energy (E_{ads}, absolute value) of 3.71 eV, significantly larger than that of Co_3Se_4 (3.56 eV) and NiSe (3.62 eV). The above-calculated results indicate bimetallic selenide is more

advantageous to adsorbing OH− than monometal selenides and thus promoting OER kinetics, which is in accord with the experimental results.

Figure 3.12b shows 95% IR-corrected polarization curves and their corresponding overpotentials of 2D holey NCS and NCO samples. NCS holey nanosheets require an overpotential of less than 300 mV, which is 60 mV lower than that of the NCO precursor and even better than that of the conventional commercial RuO_2 electrocatalyst. This result suggests the phase conversion from metal oxides to metal selenides can significantly improve the catalytic activity. The intrinsic activity of holey selenide nanosheets is further confirmed by the Brunauer−Emmett−Teller (BET) surface normalized polarization curves and turnover frequency (TOFs). NCS holey nanosheet catalysts exhibit TOFs of 0.016 s^{-1} per total 3d metal atoms at an overpotential of 300 mV, which is much larger than that of NCO holey nanosheets. To sum up, the superior electrocatalytic oxygen evolution activity of 2D transition metal selenide holey nanosheet is synthesized. Based on the above studies including metallic characteristics of selenide samples and the heteroatom effect, the enhanced performance of NCS can be attributed to the synergistic effects of metallic characteristics, holey nanosheet architecture, and synergistic interaction between mixed transition metal atoms.

3.3.3 Anion effect in 2D nanostructured Ni/Co-oxide/selenide/phosphide for electrocatalytic hydrogen evolution

It is generally believed that anions in dichalcogenides and phosphides act as the base to adsorb protons during the hydrogen evolution process and meanwhile modify the electronic structure of electrocatalyst, but the correlation between the anion species in the electrocatalysts and catalytic properties is still not well understood. Although substantial

efforts have been made to the rational design of efficient HER electrocatalysts, in-depth research into the electronic structures and adsorption properties of MTM-based electrocatalysts is still lacking.

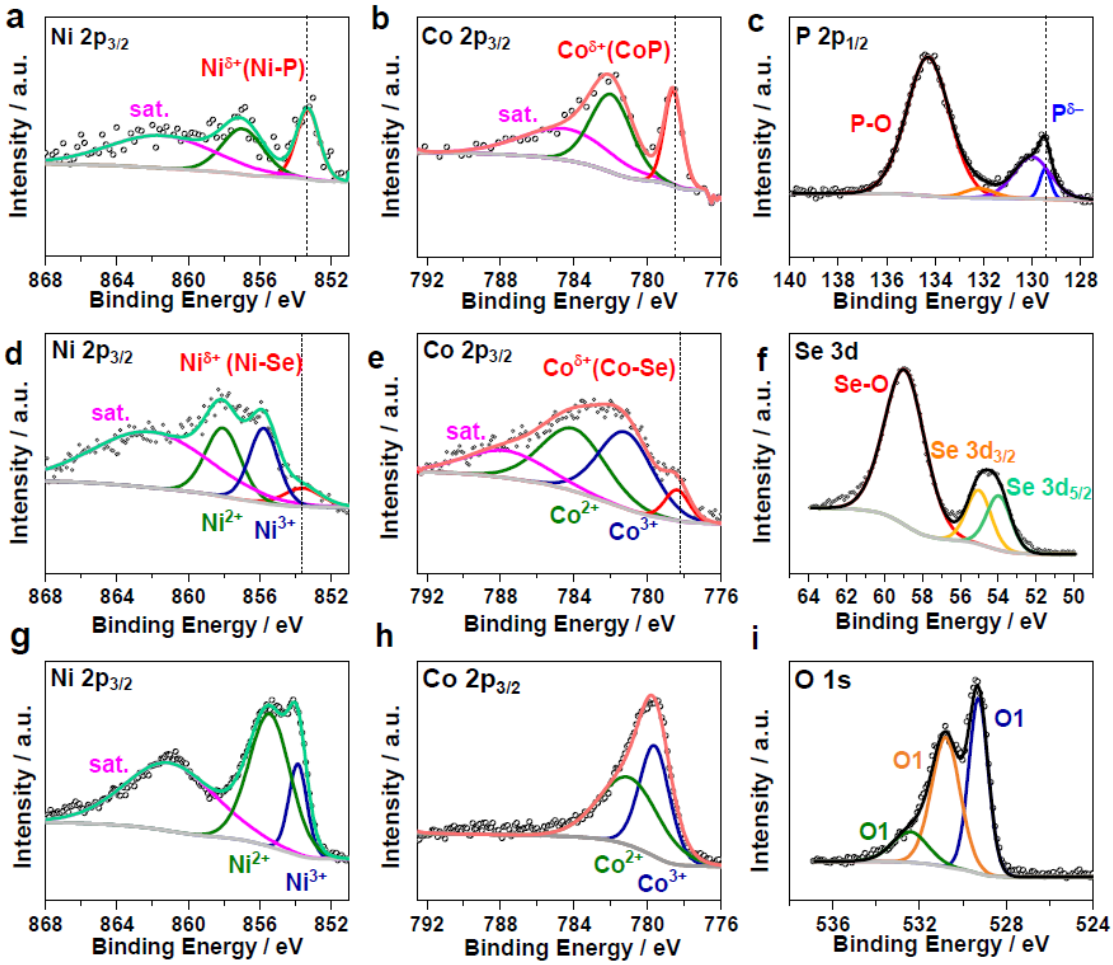

Figure 3.13: XPS test of a series of NCA holey NSs: (a) Ni $2p_{3/2}$ spectrum, (b) Co $2p_{3/2}$ spectrum, and (c) P $2p_{1/2}$ spectrum of NCP holey NSs. (d) Ni $2p_{3/2}$ spectrum, (e) Co $2p_{3/2}$ spectrum, and (f) Se 3d spectrum of NCS NSs. (h) Ni $2p_{3/2}$ spectrum, (h) Co $2p_{3/2}$ spectrum, and (i) O 1s spectrum of NCO holey NSs.

Thanks to the tunable chemical composition (via heterometal doping and anionic substitution), high electrical conductivity (owing to their metallic property), and optimized adsorption energy, MTM-based electrocatalysts can serve as an ideal platform to study anionic effect in electrocatalysis. In this regard, I choose Ni/Co-based oxide, selenide, and phosphides with 2D holey nanostructure as the studying materials.

X-ray photoelectron spectroscopy (XPS) test (Figure 3.13) is first conducted to study the composition of NCA and the transition metal-anion bonds. In the holey NCP nanosheet sample, the binding energy at 853.2 eV can be assigned to Ni−P bonding, which is close to that of metallic Ni (852.6 eV), suggesting the presence of partially charged Ni species ($Ni^{\delta+}$, $0< \delta <1$).[31] The peak at 857.0 eV can correspond to Ni−PO_x with its shakeup satellite peak at 861.3 eV. Similarly, the binding energy at 778.6 eV in Co 2p3/2 spectra can be correlated to Co−P bonding, which is also close to that of metallic Co (778.2 eV). For the P 2p region, the peak at 129.1 eV corresponds to the formation of metal phosphides, slightly lower than that of elemental P (130.0 eV), which suggests that the P atom is partially negatively charged ($P^{\delta-}$). It should be noted that the peak at 132.9 eV is assigned to the phosphate species (PO_4^{3-}, etc.), mainly due to the partial oxidation of the surface layer after air exposure according to previous studies.[26] Similarly, $Ni^{\delta+}$ and $Co^{\delta+}$ bonding can be confirmed in NCS (Figure 3.13d and e). However, $Ni^{\delta+}$ and $Co^{\delta+}$ composition is missing in the oxide sample, indicating the most localized electron in Ni-Co-O.

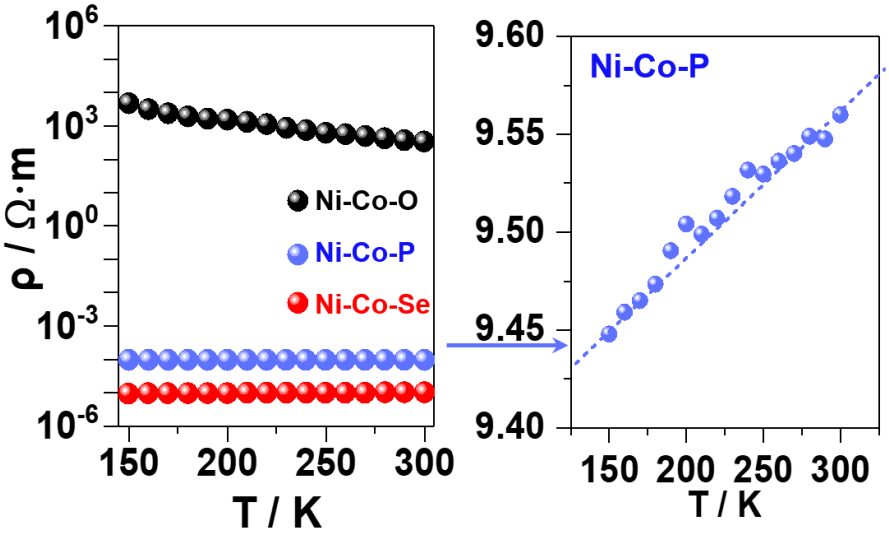

Figure 3.14: Electrical resistance plotted as a function of the temperature of Ni-Co-O, Ni-Co-P, and Ni-Co-Se.

The electrical properties of the three samples are further studied. From the Electrical resistance plotted as a function of the temperature of Ni-Co-O, Ni-Co-P, and Ni-Co-Se, the electrical resistance of NCP and NCS keeps increasing as temperature increases, displaying the metallic-like behavior and electron delocalization (Figure 3.14), which is in good consistency with the density of states for NCP and NCS in other recent studies.[15, 28, 31, 32] In comparison, the electrical resistance of mixed transition metal oxide decreases as the temperature increases with about six orders of magnitude higher than that of the corresponding phosphide and selenide at room temperature. The electron transport results indicate that phosphorus/selenium substitution of oxygen can result in the enhanced electron delocalization, which is an agreement with the peaks of $Ni^{\delta+}$, $Co^{\delta+}$, and $X^{\delta-}$ ($P^{\delta-}$, $Se^{\delta-}$) in the XPS data.

Typically, moderate electron delocalization is expected to be advantageous to the HER kinetics. Electron delocalization can lower the charge transfer resistance between

catalysts and the current collector, but too strong electron delocalization may decrease the electron density on anion species (the smaller value of δ in $X^{\delta-}$), leading to the less affinity for protons. Additionally, the electrical conductivity is highest in selenide electrocatalyst, indicating stronger electron delocalization, which may slow the kinetics of proton trapping. Therefore, moderate electron delocalization in NCP could facilitate the charge transfer and meanwhile reduce the barrier of proton binding on $P^{\delta-}$ to boost the overall kinetics.

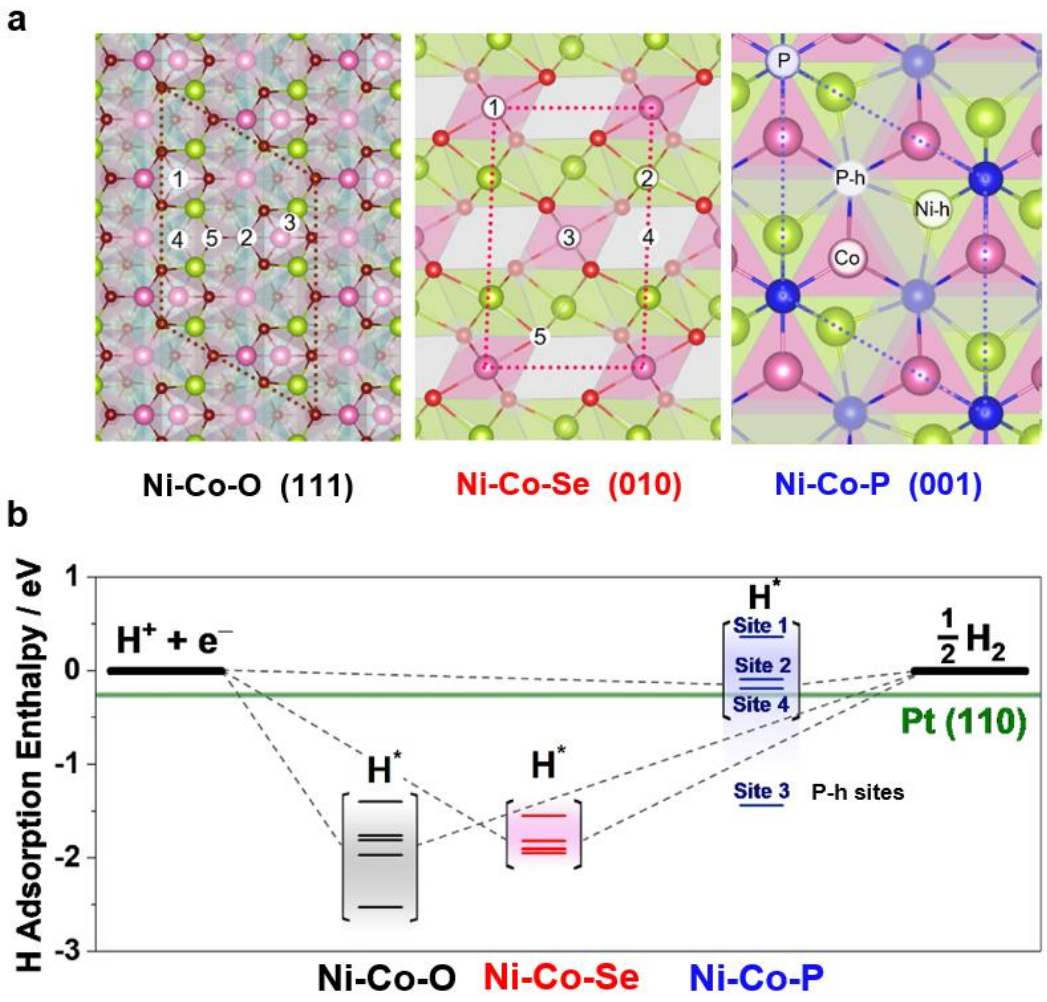

Figure 3.15: (a) Atomic structure of the H-covered surfaces and (b) the corresponding H adsorption/desorption enthalpy diagram.

NCO	Bridge (Ni-Co)	Co4	Co8	Hollow	O8
Site*	3	1	2	4	5
Adsorption Enthalpy/eV	-1.80	-1.39	-1.96	-1.75	-2.52

Table 3.2: Hydrogen adsorption enthalpy on NCO (111).

*Site numbers are corresponding to the numbers shown in Figure 3.12.

NCS	Bridge (Se-Se)	Co	H	Ni	Se
Site	3	1	4	2	5
Adsorption Enthalpy/eV	-1.55	-1.91	-1.90	-1.95	-1.82

Table 3.3: Hydrogen adsorption enthalpy on NCS (010).

NCO	P	Co	Hollow (P)	Hollow (Ni)
Site	1	2	3	4
Adsorption Enthalpy/eV	0.36	-0.09	-1.44	-0.19

Table 3.4: Hydrogen adsorption enthalpy on NCP (001).

To understand the trend of the hydrogen evolution kinetics of NCA (A=O, Se, P) holey nanosheets, the electrocatalytic HER performance and hydrogen adsorption/desorption modeling are studied. The HER process in an alkaline electrolyte, at the atomic level, can be demonstrated from the initial catalyst-water (hydroxyl ion) state to the catalyst-H intermediate state, and the final catalyst-H_2 state.[33] To further obtain mechanistic aspects of the HER on the surface of the MTM-based electrocatalysts, the reaction pathways on NCA catalysts for HER are studied by applying the DFT method to calculate the hydrogen adsorption enthalpy of catalysts. The (001) facet of NCP, (010) facet of NCS, and (111) facet of NCO are chosen as the surface model, because of their highest catalytic properties based on the previous studies.[34, 35] The first-principles calculations based on the DFT method are conducted within the spin-polarized generalized gradient approximation. Based on the calculation results, bimetallic phosphide holey nanosheets possess the smallest hydrogen adsorption enthalpy (absolute value) compared to that of NCS and NCO at almost all sites. For Ni/Co-oxides, hydrogen will be first adsorbed on the oxygen site to form $O{-}H_{ads}$ owing to the largest adsorption. However, the bond between O and H is too strong, leading to the low energy of $O{-}H_{ads}$ intermedia and increased energy barrier toward the desorption of H_{ads} from the oxygen site. This result shows the same trend with the anion-hydrogen bonding strength and electronegativity. Compared with P−H, 322 kJ/mol and Se−H, 276 kJ/mol, O−H bonding possesses the largest energy 463 kJ/mol. Also, the electronegativity of oxygen (3.5) is larger than Se (2.6) and P (2.2). From electron transport measurement, electron delocalization selenide is stronger than phosphide, indicating a smaller value of δ in selenide, which is not favorable to adsorb atomic hydrogen.

According to the calculation modeling result, the hydrogen atom prefers to be first adsorbed on a Co 3-fold hollow site with the phosphorus atom beneath (site 3, P-hollow

site, Ph site), owing to its largest adsorption energy among all possible sites. After all Ph sites are occupied with hydrogens, the rest of the sites will start to adsorb protons. Considering the moderate absorption energy of atomic hydrogen, desorption of Co, Nh, and P sites is significantly easier than the active sites in comparative selenides and oxides. The above-calculated results indicate that NCP is more advantageous to facile desorbing hydrogen and thus facilitating the HER kinetics.

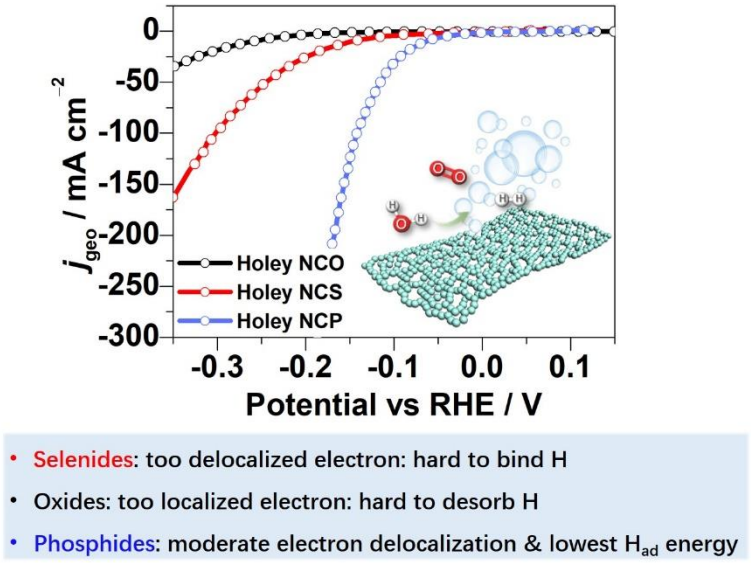

Figure 3.16: HER performance of a series of NCA holey nanosheets in 1.0 M KOH aqueous solution and the correlation between electron localization and hydrogen binding.

Based on the above understanding, the HER performances of NCP holey nanosheets and control samples (c-NCP, nanosheets without holes) are investigated. The NCP control sample (no-holes) requires an additional overpotential of 130 mV to reach the same current density of holey NCP, as shown in Figure 3.17a. The difference can be ascribed to the holey nanostructure into the NSs. Tafel slopes of 2D holey NCP and control samples are also investigated in Figure 3.17b. The Tafel slope of NCP holey NSs is 57

mV/dec, much smaller than that of the NCP control sample (109 mV/dec), indicating the improved kinetics in holey structures. The unique holey structure, due to the higher surface area and open structure, possesses a higher wettability than the control sample, which could improve the electrolyte penetration and enlarge the contact degree between electrolytes and active sites on the catalyst-modified electrode and thus facilitate the HER kinetics.

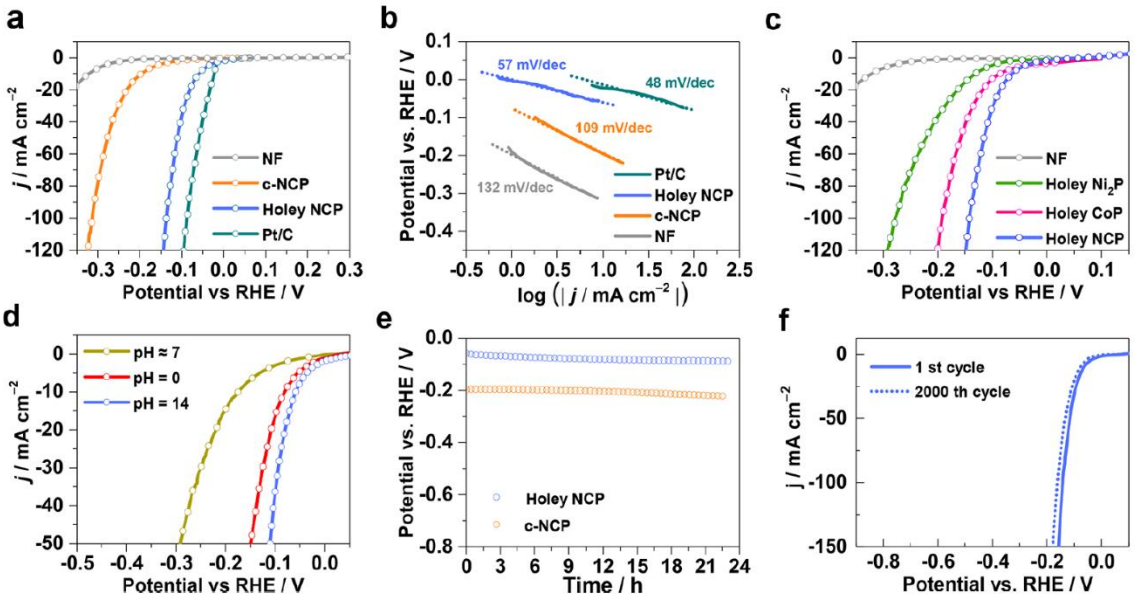

Figure 3.17: (a) LSV curves of NCP holey NSs. (b) Tafel plots of NCP holey NSs, c-NCP (control NSs, no holes), and bare Ni foam. (c) LSV curves of phosphide holey NSs. (d) HER performance of NCP holey NSs in acidic, neutral, and alkaline media. (e) Chronopotentiometric measurement of NCP holey NSs and c-NCP at the current density of 10 mA cm^{-2}. (f) Cycling stability of NCP holey NSs.

Additionally, a series of phosphide holey NSs, including CoP, Ni_2P, and NiCoP, are also tested for hydrogen evolution in a 1.0 M KOH solution (Figure 3.17c). Compared with binary phosphide holey NSs, NiCoP shows significantly increased HER performance after the introduction of heteroatom Co. The difference can be ascribed to the synergistic effect of bimetal atoms in MTM-based phosphides with an enhanced hydrogen adsorption

energy of the bimetallic compound and greater electron delocalization (similar to NCS in Chapter 3.3.2).

Catalysts	Overpotential (mV)		Substrate	Tafel Slope ($mVdec^{-1}$)	Electrolyte	Ref.
	onset	10mA cm^{-2}				
Holey NiCoP NS	~0	58	Ni foam	57	1M KOH	our work
Co_2P@NPG	61	170	GC	96	1M KOH	[36]
CoP NW array	115	209	CC	129	1 M KOH	[26]
CoP/rGO-400	--	150	GC	38	1 M KOH	[37]
CoP_2/RGO		88	GC	50	1 M KOH	[38]
Co_2P nanorods	70	134	Ti	71	1M KOH	[39]
c-$CoSe_2$		190	CC	85	1M KOH	[40]
CoN_x/C	75	170	GC	75	0.1 M KOH	[41]
Nest-like NiCoP		68	CC	62	1M KOH	[42]
NiCoP hollow NCs	--	150	GC	61	1 M KOH	[43]
$No_{0.51}Co_{0.49}P$	--	82	Ni foam	43	1 M KOH	[44]
NiCoP hollow polyhedra	74	124	GC	42	1M KOH	[45]
NiCoP NS		32	Ni foam	37	1M KOH	[46]
NiCoP/rGO		209	CFP	124	1M KOH	[47]
Ni_2P/Ni		98	Ni foam	72	1M KOH	[48]
Ni_5P_4		49	Ti	98	1 M KOH	[49]
NiS		131	Ni foam	83	1M KOH	[50]
NiSe		96	Ni foam	120	1 M KOH	[51]
Nanoporous-CoP NWs	48	100	Ti	71	1 M KOH	[52]

Table 3.5: Comparison of HER performance for holey NCP with other non-noble-metal HER electrocatalysts in alkaline solution.

Remarkably, 2D NCP holey nanosheets could serve as the HER electrocatalyst over a wide range from acidic to neutral and alkaline electrolytes. The catalytic activity toward HER is investigated in pH=0, 7, and 14, as shown in Figure 3.17d. Elemental Ni, Co, and their corresponding oxides are known as chemically unstable metals in acidic media. In the phosphide sample, NiCoP only needs an overpotential of 80 mV in 0.5 M H_2SO_4 solution, thanks to the enhanced chemical stability of phosphides in acid solution. Compared with commonly used acidic and alkaline solutions for hydrogen reduction, the neutral solution serves as a more environmentally benign media with practical perspectives, but the applications in neutral media still suffer from the low current density and relatively low kinetics. The MTM-phosphide holey nanosheet electrocatalyst can achieve the current density of 10 mA cm^{-2} at a cell voltage as low as 170mV, with a low onset overpotential of 50 mV, in 1.0 M phosphate-buffered saline (PBS).

Catalysts	Overpotential (mV) @10mA cm^{-2}			Substrate	Ref.
	alkaline	neutral	acidic		
Holey NiCoP NS	58	170	80	Ni foam	our work
Co_2P@NPG	170	130	103	GC	[53]
$Co_{0.59}Fe_{0.41}P$ nanocubes	92	--	72	GC	[54]
Nanoporous-CoP NWs	100	178	78	Ti foil	[52]
Co_2P nanorods	~150	--	134	Ti	[39]
CoP/rGO-400	150	--	105	GC	[37]
NiCoP/rGO	209	124	31	CFP	[34]
Co_9S_8@C	250	280	240	GC	[55]
Co-NRCNTs	370	540	260	GC	[56]
CoN_x/C	170	247	133	GC	[41]
CoP nanowire	209	106	67	CC	[26]
Ni_3S_2	223	170	ineffective	Ni foam	[57]
Mn-Co-P	76	86	49	Ti	[58]

Table 3.6: Comparison of HER performance for holey NCP with other non-noble-metal HER electrocatalysts at all-pH values.

Stability is another important indicator to evaluate the overall performance of electrocatalysts. Chronopotentiometric measurement as well as and long-term cycling tests are conducted in pH=14 alkaline electrolyte to investigate the electrocatalytic stability of NCP holey nanosheet. Figure 3.17e shows that NCP holey nanosheets can maintain less than 90 mV over 24 h, which is as stable as the NCP nanosheets without hole structures. Additionally, after the long-term cycling measurement of 2000 cyclings, no obvious degradation can be detected from the current density (Figure 3.17f).

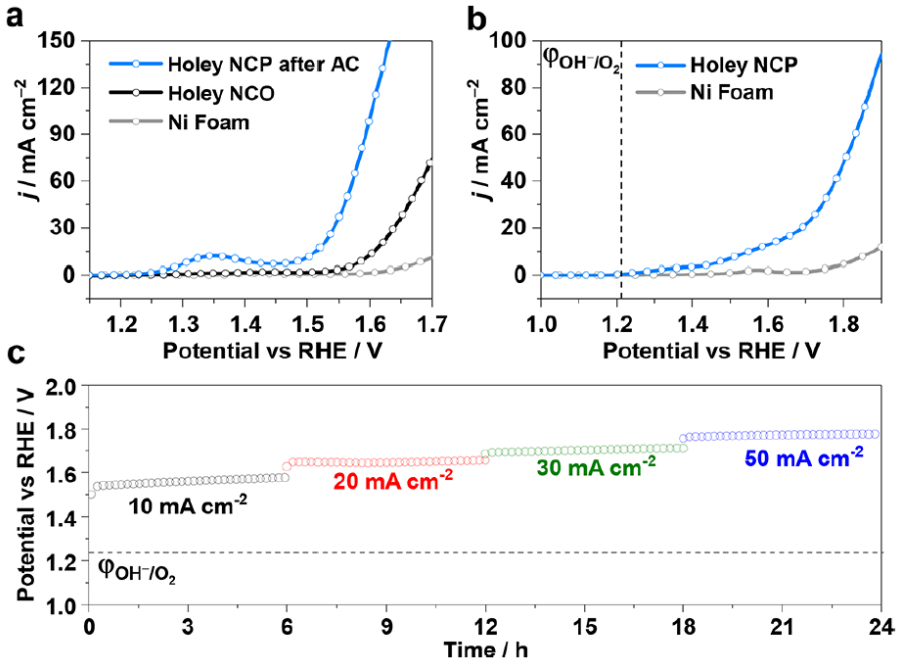

Figure 3.18: (a) OER performance of NCP and NCO holey NSs on Ni foam. (b) LSV curve of NCP holey NSs for overall water splitting. (c) Stability test of water splitting for NCP holey nanosheets.

After the assessment of the exceptional HER performance of NCP, I further evaluated the OER performance of NCP holey NSs in 1.0 M KOH electrolyte. Recently, Ni/Co-based oxygen-evolving catalysts have shown potential electrocatalytic activity for

alkaline oxygen evolution after the electrochemically anodic condition treatment, which involves the formation of an amorphous oxide layer on the surface of electrocatalyst.[19, 34, 59] After activation for 20 cycles, the surface-oxidized NCP holey nanosheets only require an overpotential of only 280 mV for OER (Figure 3.18a). Compared with control samples, NCP shows 80 mV overpotential lower than that of the NCO and 30 mV lower than that of the commercial RuO_2 electrocatalyst (310 mV).

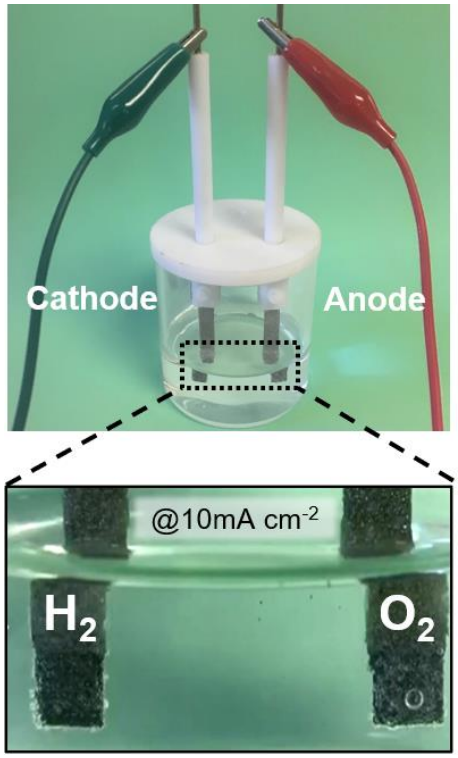

Figure 3.19: Digital photos of NCP/NCP holey NS-modified electrode couple for water electrolyzer showing H_2 and O_2 release on cathode and anode electrode, respectively.

Catalysts	Potential (V) @10 mA cm^{-2}	Substrate	Ref.
Holey NiCoP NS	1.56	Ni foam	Our work
Co_3Se_4	1.59	Co foam	[60]
Co_1Mn_1CH	1.68	Ni foam	[61]
Co_2B-500-NG	1.81	CC	[62]
Co_9S_8@NOSC	1.6	Ni foam	[63]
$CoSe_2$	1.63	CC	[40]
Fe-CoP/Ti	1.6	Ti foil	[64]
$Ni_{0.51}Co_{0.49}P$ film	1.57	Ni foam	[44]
Ni_2P	1.64	Ni foam	[65]
Ni_5P_4	1.63	Ni foam	[49]
Ni_5P_4	1.7	Ni foam	[66]
NiCoP	1.524	CC	[42]
NiCoP	1.58	Ni foam	[32]
NiCoP/rGO	1.59	CFP	[34]
NiFe LDH	1.7	Ni foam	[7]
Ni-P	1.63	CFP	[67]
NiSe	1.63	Ni foam	[51]

Table 3.7: Comparison of overall water splitting application for holey NCP with other non-noble-metal electrocatalysts at basic media.

The improved OER performance suggests that NCP holey nanosheets can be applied as a potential bifunctional catalyst for overall water splitting. To further explore the usability of holey NCP NSs in water electrolyzer, an alkaline electrolyzer based on the NiCoP holey NSs as both anode and cathode catalyst is assembled for both HER and OER applied on Ni foam electrodes. Figure 3.18b shows the polarization curve of this electrolyzer in a two-electrode system. A current density of 10 mA cm^{-2} can be obtained at about 1.56 V, which corresponds to a combined overpotential of only 340 mV for OER and HER, while using Ni foam required a combined overpotential of 640 mV, for comparison. The potential can be maintained at 1.56 V without obvious degradation during a 16-hour- galvanostatic water electrolysis when employing the electrolyzer of a NCP/NCP holey NS-modified electrode couple. Remarkably, as demonstrated in Figure 3.18c, this electrolyzer is able to maintain the current density of 20 mA cm^{-2} at a cell voltage as low as 1.63 V and 50 mA cm^{-2} at 1.78 V over 6 hours, respectively. Thus, NCP holey nanosheets enabled a high-performing water electrolyzer with excellent bifunctional electrocatalytic activity and durability.

To sum up, controlling the anionic effect offers a general design protocol for HER electrocatalysts with moderate electron delocalization, abundant active sites (as both water acceptor and proton-acceptor center), and lowest hydrogen adsorption energy. The anion tuning strategy in the holey NS HER electrocatalysts can achieve the above goals for efficient hydrogen production.

3.4 CONCLUSIONS

The superior electrocatalytic oxygen evolution activity of 2D transition metal selenide holey nanosheets can be attributed to the synergistic effects of metallic

characteristics, holey nanosheet structure, and synergistic interaction between mixed transition metal atoms. First, the metallic features favor the electron transfer kinetics between the catalyst and current collector. Second, holey nanoarchitecture could enhance the electrolyte diffusion and augment the contact degree between the electrolyte and catalyst-modified electrode. This unique structure provides a shortened pathway to facilitate electrolyte penetration and facile release of evolved O_2 bubbles. Lastly, the synergistic effect of Ni/Co atoms can enhance the electrocatalytic activity, owing to their modified electronic structure and mixed-valence states for faster OER kinetics. Due to these synergistic characteristics, metallic NCS holey nanosheets show superior catalytic activity for OER, including low overpotential of 295 mV, low Tafel slope, and enhanced cycling stability.

For another, we applied a novel approach to tuning the anion-dependent electrocatalytic characteristics in the MTM-based HER electrocatalyst, using a holey NCA nanosheet as the model materials. Extensive electrochemical characterizations, combined with electron transport test and DFT calculations, suggest that P substitution can modulate the electronic configuration and lower the hydrogen adsorption energy on active sites. The superior electrocatalytic performance of MTM phosphide holey nanosheets can be attributed to the synergistic effects of the lowest hydrogen adsorption energy, desirable electron configuration, and two-dimensional holey nanoarchitecture. Thanks to these advantageous features, NCP holey nanosheets are demonstrated to be one of the best electrocatalysts with exceptional electrocatalytic performance for hydrogen generation and overall water splitting among the reported Ni/Co-based dichalcogenides. Based on the above understanding, I fabricate the NCP holey nanosheet catalyst with a low overpotential of 58 mV at 10 mA cm^{-2} and a low Tafel slope of 57 mV/dec to catalyze HER. In addition,

NCP holey nanosheets exhibit an ultralow applied potential of 1.56 V at 10 mA cm^{-2} and long-term durability.

Through the rational structural design and electronic tuning of transition metal selenide/phosphide-based holey nanosheets, the reported nanomaterials serve as highly efficient and stable electrocatalyst towards water-splitting electrocatalysis, due to their metallic behavior, holey nanoarchitecture, as well as abundant electrochemically active surface. The above works not only present a deeper understanding of the OER/HER electrocatalytic properties for MTM-based electrocatalysts with various anion species, but also offer new insights to better design highly efficient, durable, and earth-abundant water splitting electrocatalysts.

Chapter 4: Hybrid organic−inorganic hydrogels for electrocatalytic acidic water oxidation[2]

4.1 INTRODUCTION TO GELS FOR ELECTROCATALYSIS

Gel materials are nonfluid colloidal or polymer networks saturated with liquid, yet behave like solids due to a 3D crosslinked network within the liquid. Gel-based functional materials have so far become one of the most extensively investigated soft materials in the twenty-first century and currently continue to spark intensive research.[68] The progress made in medicine[69, 70], biologies[71], and environmental fields[72] has prompted tremendous research efforts on exploring novel gel-based systems applicable in wide ranges of energy-related fields. Recently, nanostructured gels have emerged as a unique material platform for various applications in energy storage, because of their porous frameworks with abundant defects for mass transport, controllable chemical composition, and ease of synthesis and functionalization.[73-77] Gel materials exhibit exceptional features including low mass density, high specific surface areas, and hierarchical porous architectures, allowing gel frameworks to potentially host different kinds of active electrocatalysts within their porous architectures, thus facilitating mass transport during electrocatalysis.[73, 78-80]

The use of gel-based electrocatalysts can alleviate many critical issues encountered in the solid-stated electrocatalysts and meanwhile lead to materials with new physicochemical properties.[81] To date, most reported electrocatalysts are still severely restricted by the low efficiency, selectivity, or poor durability of electrocatalysis.

[2] **Z. Fang**, P. Wu, K. Yu, Y. Li, Y. Zhu, P. J. Ferreira, Y. Liu, G. Yu, "Hybrid Organic-Inorganic Gel Electrocatalyst for Stable Acidic Water Oxidation", ***ACS Nano*** 13, 14368 (2019).
Z. Fang, P. Li, G. Yu, 'Gel Electrocatalysts: An Emerging Material Platform for Electrochemical Energy Conversion', **Adv. Mater**. 32, 2003191 (2020).
Z. Fang, A. Zhang, P. Wu, G. Yu, "Inorganic Cyanogels and Their Derivatives for Electrochemical Energy Storage and Conversion", **ACS Mater. Lett**. 1, 158 (2019).
Y. Guo†, J. Bae†, **Z. Fang**†, P. Li†, F. Zhao, G. Yu, 'Hydrogels and Hydrogel-Derived Materials for Energy and Water Sustainability', **Chem. Rev.** 120, 7642 (2020).
Z. Fang participated in the experimental work and the preparation of manuscripts.

Conventional electrocatalysts prepared from bulky powders typically suffer from drastically problems on mass and charge transports, such as self-agglomeration, resulting in decreased active sites and unfavorable electron and mass transport, and inferior electrical conductivity (such as metal oxides, hydroxides, and perovskites), which also impedes the electrocatalytic activities by restricting the electron transport between electrodes and electrocatalysts. Moreover, traditional conductive supports usually are unable to give well-anchored particles, leading to peeling off, agglomeration, and dissolution of electrocatalyst materials. Concerning mass transfer and catalyst durability, multi-dimensional interconnected networks with high porosity and robustness are critically required.

Owing to the interconnected porous architecture, compositional and structural tunability, and ease of functionalization, the family of gel materials opens exciting opportunities for advanced energy conversion technologies.[79, 82] Unique advances in gel materials based on tunable compositions and functionalities enable gel electrocatalysts to potentially break the limitations of current electrocatalyst materials, enhancing the device performance of electrochemical energy. For one thing, the use of gel materials can alleviate problems usually encountered in the solid-state and meanwhile lead to materials with new physicochemical properties. Compared with bulk electrocatalysts and conventional porous materials, gel-based materials can offer larger numbers of active sites thanks to their hierarchical architectures with large specific surface areas for the adsorption/desorption of reactant/intermediate molecules. For another, many conductive gel frameworks can serve as a conductive platform to promote electron transport and facilitate the electrochemical reaction kinetics (Figure 4.1).

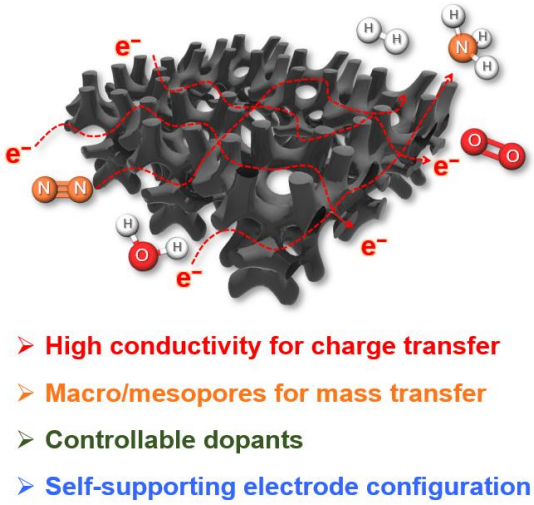

Figure 4.1: Schematic illustration of the key features of gel materials for electrocatalysis.

Gels are usually considered as a 'non-fluid colloidal network or polymer network that is expanded throughout its whole volume by a fluid'.[83] Most gels can be formed through the gelation process that is the formation of 'jelly-like' solids with the interconnected framework from the solvents or suspensions containing certain molecular precursors. Based on the precursors, gel materials can be made of organic molecules,[84] metal oxides/hydroxides/alkoxides,[85] metal complexes,[86] and carbon-based materials (such as graphene,[87] carbon nanotubes[88]). Based on the mechanism of gelation (polymerization to jelly-like products), the synthetic methods for gels can be categorized into radical polymerization, hydrothermal/solvothermal method, sol-gel method, ligand-substitution method, and more. The synthesis of organic polymer gels, such as e.g., polypyrrole (PPy),[88] polyaniline (PANI),[84] is generally performed by the radical polymerization of organic monomers, which involves the complex chain reactions triggered by initiators. Staring from organic monomers, one monomer is oxidized to generate a radical cation that couples with another radical cation to form a dimer after losing two protons. Then, the dimers will

be oxidized and couples with other radical cations to generate oligomers, which are further propagated via the sequence of oxidation, coupling, and deprotonation. This propagation can be terminated until the polymer with desired long chains is formed. The oxidation step is generally induced by chemical oxidations, the electrochemical process, photochemical initiations, etc.[89] During the radical polymerization, crosslinkers are normally introduced to form the polymer hydrogels with interconnected polymer chains via the chemical/physical interaction between the polymer chains and functional groups of crosslinkers. Hydrothermal/solvothermal reactions, considered as a type of heterogeneous reaction, can be conducted in an enclosed system with the temperature above the boiling point at high vapor pressures.[87] Water or organic solvents are typically used as the reaction fluid in hydrothermal and solvothermal reactions. Traditional sol-gel method is usually applied to prepare inorganic polymers or ceramics with 3D networks through hydrolysis and condensation of metal alkoxide precursors.[90] This process involves the transformation from precursor solutions to sols and further to interconnected gels. Currently 'sol-gel method' has been extended to many other routes covering the synthesis of solid materials from solution-state precursors.

Cyano-bridged coordination polymers (CCPs), as a type of inorganic gel (cyanogel) synthesized via ligand-substitution method, contain alternating main-group-metals and transition-metals bridged by cyanide ligands.[82] CCPs have recently sparked increasing research interests due to their structural tunability and attractive electrochemical properties. The gel-like features, because of the abundant coordinated solvent molecules and lattice vacancies caused by the introduction of main group metals, such as In, Sn, etc., allow the homogeneously dispersed multimetal phase and hydrophilic property.[91] Moreover, thanks to the large surface area and porous structure with hydrophilic features, the 3D open structure allows easier electrolyte penetration and thus facilitates the overall

electrocatalytic kinetics. Cyanogel can be synthesized by a coordination−substitution polymerization between chlorometalates (metal chlorides, such as $InCl_3$, $SnCl_4$, $RuCl_3$, $PdCl_4^{2-}$, etc.) and cyanometalates (metal cyanides, such as $Fe(CN)_6^{4-}$, $Ni(CN)_4^{2-}$).[86, 92, 93] In a typical cyano-polymerization reaction, the nitrogen end of the cyano ligand in cyanometalates replaces the chloride ligand in chlorometalates, forming the bridges between the M' (main group metals or noble metals)and transition metal (M'') side and side (M''−C≡N−M'), such as Fe−C≡N−In. This cyano reaction (coordination−substitution) proceeds consecutively in all three dimensions and eventually forms a three-dimensional cyano-bridged coordination polymer with a high variety of chemical compositions and uniform multimetal distribution— the transition metal (M'') side can be controlled by changing the ratio of cyanometalates, the same for the M' side, forming homogeneous elemental distribution in the polymer gel solution. In this Chapter, we use an InFeCo-cyano-based coordination polymer (InFeCo-CCP, containing Fe−C≡N−In and Co−C≡N−In) as a model material.

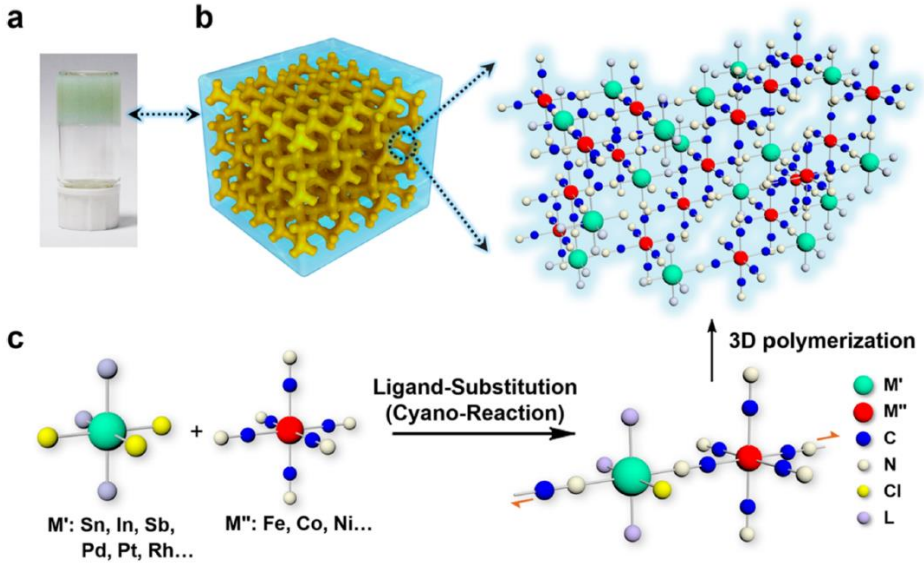

Figure 4.2: (a) Photograph of a typical Sn−Fe cyanogel. (b) Structural model of cyanogels. (c) Ligand-substitution reaction.

More importantly, similar to other nanostructured gel materials, it is worthwhile mentioning the compositional tunability of cyanogels. Due to the large pore volume and interconnected structures, the tailoring of the physicochemical properties of catalysts can be achieved by introducing functional dopants in gels. As shown in Figure 4.3, various materials, including carbon-based materials (graphene, GO, CNTs), polymers, and nanoparticles with different dimensionality can be uniformly anchored into cyanogels in the nanoscale. For example, conductive polymer gels, including polypyrrole (PPy) and polyaniline (PANI), exhibit desirable electrical conductivities, large surface areas, 3D interconnected porous nanostructures, and strong structural integrity.[94] Compared with the commonly used carbon-based composites synthesized by physical mixing or weak chemical interaction, highly penetrated conductive polymer gel in an inorganic polymer gel framework can facilitate both mass transfer and charge transport significantly, contributing to their high performance when applied for potential energy conversion devices.

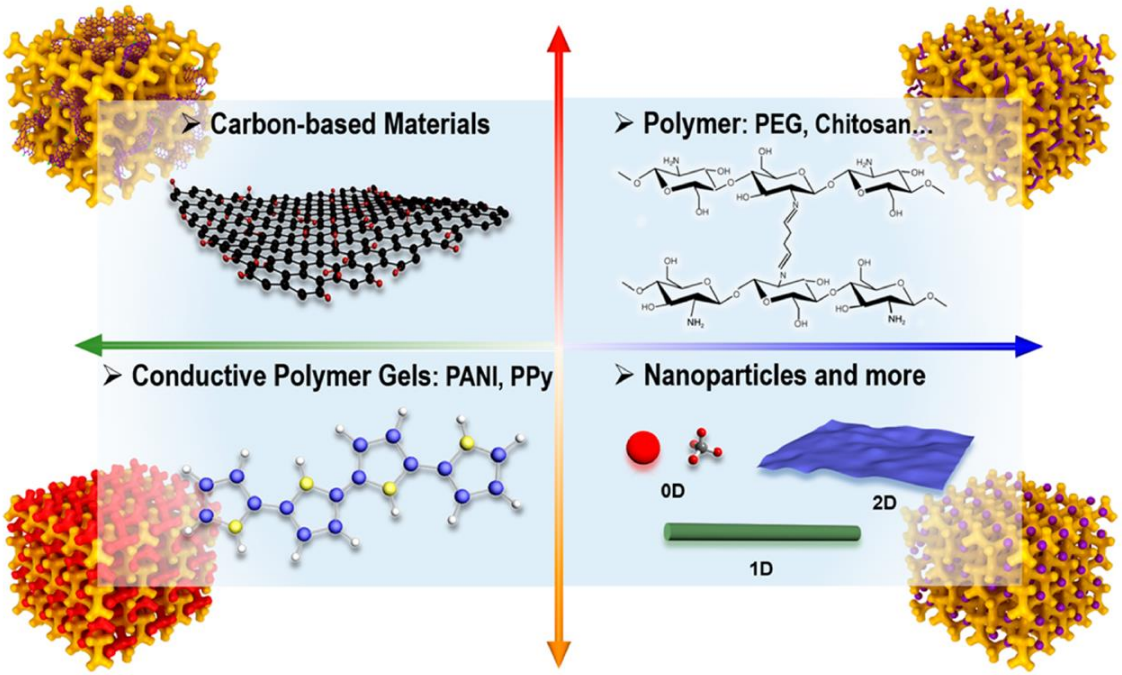

Figure 4.3: Diagram of the functionalization of cyanogel by adding carbon-based materials, polymers, and nanomaterials into cyanogel host.

As mentioned in the previous chapters, precious-metal-free materials, such as earth-abundant transition metal oxides,[5] metal carbides,[95] metal sulfides,[10] metal phosphides,[34], etc., have emerged as promising candidates for alternative electrocatalysts for oxygen evolution, but the electrochemical instability remains a major issue for WOCs especially under strongly acidic conditions. Acidic water oxidation is highly desirable in many advanced electrochemical devices, as discussed in Chapter 1, such as polymer electrolyte membrane (PEM) electrolyzers and fuel cells, due to the higher ionic conductivity in acidic electrolytes has and fewer amounts of carbonates as contaminants, which usually occurs in alkaline electrolytes. Unfortunately, the acid can react with most non-noble metal oxide catalysts to protonate the oxide framework, weakening metal−oxygen bonds and thus

facilitating the dissolution of catalysts.[96] For another, carbides, selenides, phosphides and many others suffer from low thermodynamic stability under oxidizing potentials.[97] One recent work reported that water-insoluble cobalt-containing polyoxometalate salts showed potential catalytic activity on carbon-paste conducting support in acidic electrolytes.[98] Similarly, manganese oxides, owing to their self-healing features, can be applied as electrocatalysts for acidic OER, but r low OER kinetics limit their application.[99]

Among the non-noble-metal-based electrocatalysts, Prussian blue analogue (PBA) catalysts, owing to their unique d electron structures, high corrosion nature, and earth-abundant feature, have been recently investigated as a hot topic for diverse energy-related applications.[100-103] For instance, Fe-Co-PBA thin films show excellent stability and desirable OER activity with the homogeneous catalytic feature under acidic conditions, holding significant promise as active materials for the alternative acidic OER electrocatalyst.[101] However, the electrical conductivity of PBA is poor, and it is still challenging to add conductive additives uniformly to maximize the electron transfer.

4.2 MATERIALS SYNTHESIS AND CHARACTERIZATION DETAILS

4.2.1 Synthesis of cyano coordination polymers

Cyano-bridged coordination polymers (CCPs) were made at room temperature (R.T.) from 1.0 M aqueous solutions of chlorometalate ($InCl_3 \cdot 4H_2O$) and 1.0 M cyanometalate ($K_3Fe(CN)_6$ and $K_3Co(CN)_6$) with 1:1 volume ratio. Different volume ratios of potassium hexacyanoferrate were included in the initial cyanometalate solution. The mixtures were allowed to react until hydrogel formed and then aged for one hour.

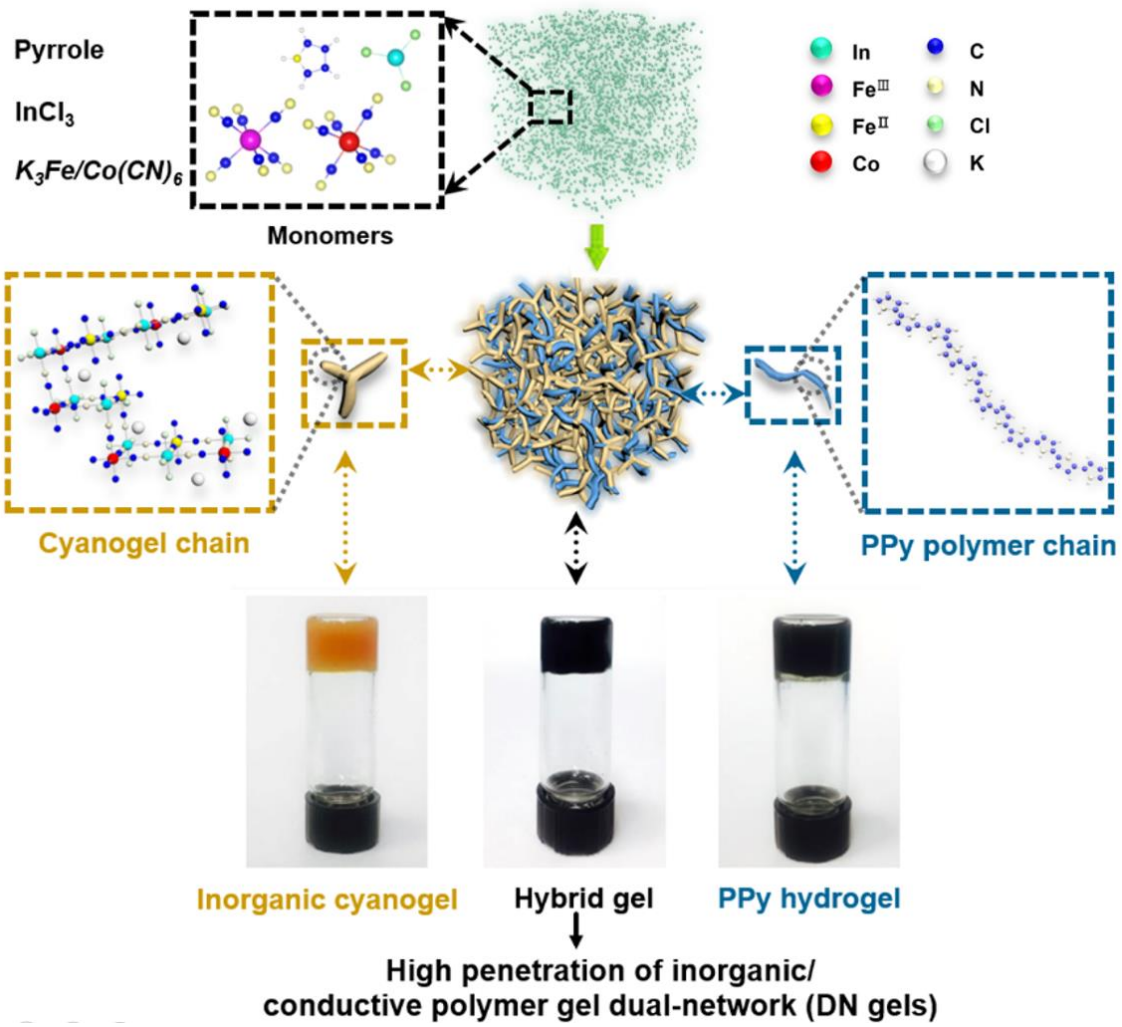

Figure 4.4: Scheme of the formation of PPy/CCP gel dual-network (DN gels) and their digital photos.

4.2.2 Synthesis of organic-inorganic hybrid hydrogels

Hybrid double-network gels were made from 1 M aqueous solutions of chlorometalate, 1M cyanometalate, and 0.5 M pyrrole or aniline with the same volume ratio. For the PPy/InFeCo-CCP hydrogel dual-network, solution A was the aqueous

solution containing 0.5 M pyrrole (C_5H_4N) and 1 M $InCl_3$. Solution B was the aqueous solution containing 1 M ($K_3Fe(CN)_6$ and $K_3Co(CN)_6$. Then the mixture was kept still for one hour to complete the polymerization and gelation. After freeze-drying, the PPy/InFeCo-CCP DN aerogel is synthesized. The synthesis of PANI/InFeCo-CCP DN gel is similar to that of the PPy/InFeCo-CCP DN gels except for replacing the pyrrole monomers with aniline monomers before the polymerization.

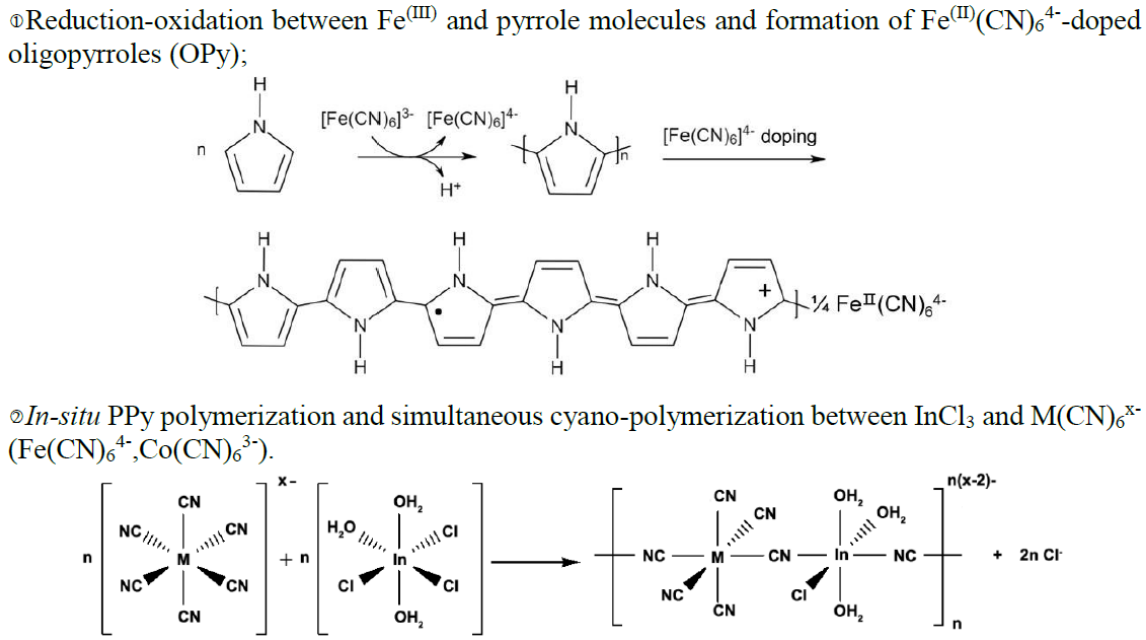

Figure 4.5: Mechanism of the simultaneous formation of PPy/CCP DN gels.

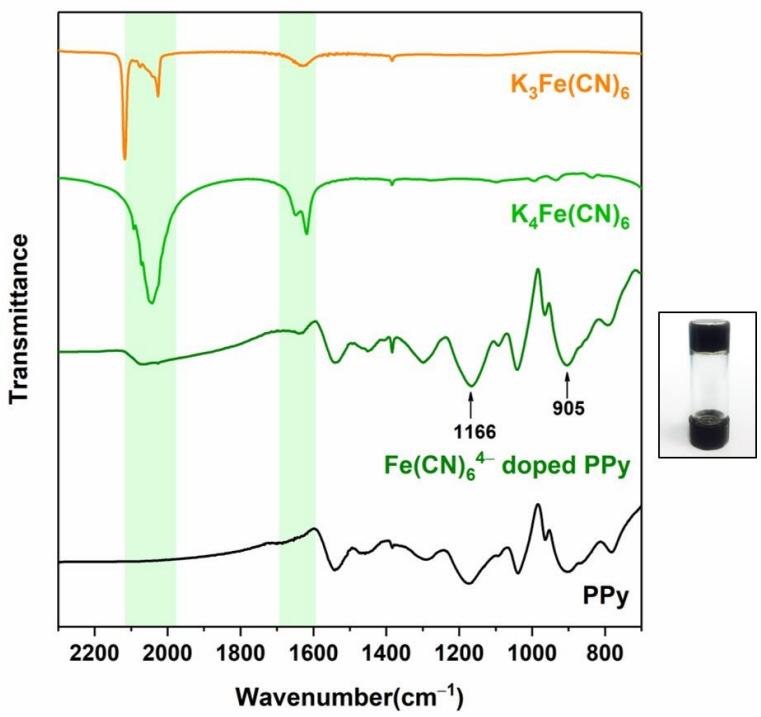

Figure 4.6: FTIR spectra of $K_3Fe(CN)_6$, $K_4Fe(CN)_6$, $Fe(CN)_6^{4-}$-doped PPy and undoped PPy.

From FTIR spectra in Figure 4.6, the $Fe(CN)_6^{4-}$ dopants are anchored to the PPy chains due to the strong chemical affinity between Fe and electronegative N atoms in the pyrrole ring.[104] The peak at 1166 cm^{-1} and 905 cm^{-1} is due to the C–N^+ stretching and C–N^+–C stretching respectively, and have been attributed to the bipolaron bands which are characteristic of the doping.[105]

4.2.3 Synthesis of control samples for acidic OER

PPy/Fe-PBA composite was synthesized in a similar method but only using $FeCl_3$ to replace $InCl_3$. The PPy hydrogel was synthesized via the oxidative polymerization of pyrrole monomers by ammonium persulfate. The $Fe(CN)_6^{4-}$ doped PPy hydrogel was

facilely obtained through the oxidative polymerization of pyrrole monomers by $K_3Fe(CN)_6$. $InFeCoO_x$ was synthesized *via* the direct heat treatment of InFeCo-CCP in the air at 700°C.

4.2.4 EXAFS experimental details

2 mg dried gel sample was homogeneously mixed with 100 mg graphite and then pressed into circular pellets with a diameter of 10 mm. Then, the XAFS measurements were 4 performed under ambient conditions. Fe *K*-edge XAFS spectroscopy was recorded in the fluorescence mode at U7C beamline in the National Synchrotron Radiation Laboratory, China, 1W1B beamline of Beijing Synchrotron Radiation Facility. The storage rings of BSRF were operated at 2.5 GeV with a maximum current of 450 mA. Si(111) double-crystal monochromator crystals were used to monochromatize the X-ray beam. The acquired EXAFS data were processed using the ATHENA module implemented in the IFEFFIT software packages. The EXAFS $\chi(k)$ spectra were obtained by subtracting the post-edge background from the overall absorption and then normalized with respect to the edge-jump step. Subsequently, *k*-weighted $\chi(k)$ data in the *k*-space were Fourier transformed to real (*R*) space using a Hanning window (d*k*=1.0 $Å^{-1}$) to separate the EXAFS contributions from different coordination shells.

4.2.5 Electrochemical measurements

All the electrochemical measurements were performed on the glassy carbon electrode were under similar conditions in Chapter 3. For the OER test, the polarization

curves were obtained by sweeping the potential from 1.2 V to 1.8 V (*vs.* Ag/AgCl electrode in saturated KCl) at a sweep rate of 5 mV s^{-1} in 0.5 M H_2SO_4.

4.3 RESULTS AND DISCUSSION

4.3.1 Structural design in hybrid organic−inorganic hydrogel catalysts

The anticorrosion resistance in strong acids of cyanogel was first studied in pH = 0 H_2SO_4 over seven days. Long-term electrochemical oxidized potential (1.70 V vs RHE) was also applied to the cyanogels to study the electrochemical stability in acid. All the peaks of cyanogels can be maintained, and no new phase is generated according to the post-XRD data, suggesting the high anticorrosion stability in acidic OER.

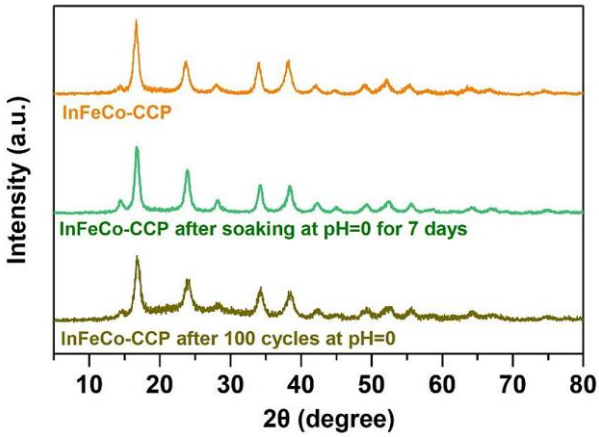

Figure 4.7: Stability of InFeCo-CCP: XRD patterns of InFeCo-CCP before and after soaking in strong acid for 7 days, and after 100 OER cycles (1.23-2.00V vs. RHE).

Because of the high electronic conductivity and electrochemical stability, polypyrrole conducting polymer is selected to increase the electrical conductivity and thus improve the electron transfer through the entire 3D inorganic coordination polymer and

promote catalytic stability. The inorganic coordination polymer/organic conductive polymer dual-network hydrogels (DN gels) were constructed through simultaneous oxidative polymerization and cyano-polymerization, as demonstrated in Chapter 4.2. We expect that the DN gels possessing abundant active sites can act as active and stable water oxidation catalysis even in strong acids.

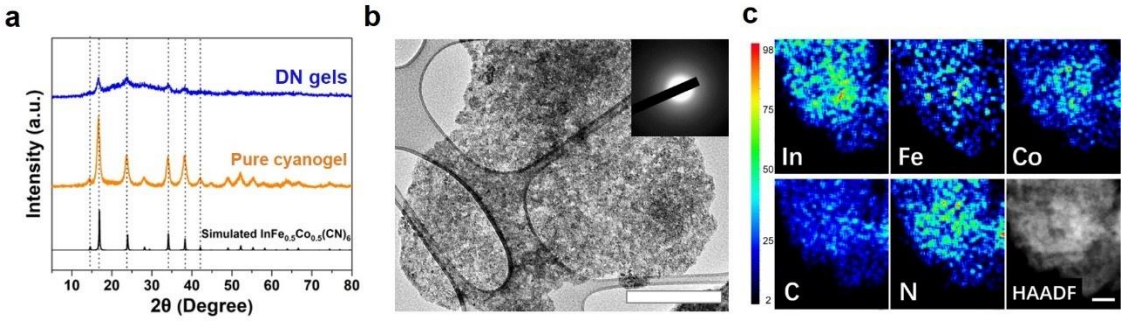

Figure 4.8: (a) XRD results of double-network gels and pure InFeCo-cyanogels and the simulated XRD pattern. (b) TEM image (scale bar: 1 μm; inset: SAED pattern, scale bar: 10 nm in the inset of (b) and (c) STEM-HAADF image of double-network gels and corresponding elemental mapping with a pixel size of 1.5 Å (scale bar: 20 nm in c).

The crystallographic characteristics of the as-synthesized DN gels were first characterized by XRD (Figure 4.8a). The peak positions of DN gels match well with the simulation data and pure InFeCo-CCP, while DN gels show a lower degree of crystallinity which indicated the increased structure disorder in DN gels due to the introduction of the intertwined PPy polymer chains. A porous structure can be observed from low magnification TEM images shown in Figure 4.8b. The selected area electron diffraction (SAED) pattern (Figure 4.8b, inset) shows the diffuse rings, implying the amorphous feature of the low-crystalline gels. On the other hand, few areas in the HRTEM image show

crystallinity, in which the interplanar distance of 0.52 nm is identified in the TEM image, which can be ascribed to the (200) facets of the $InFe_{0.5}Co_{0.5}(CN)_6$ Phase.

High-angle annular dark-field scanning transmission electron microscopy (HAADF-STEM) imaging coupled with EDX was utilized to study the spatial elemental distribution of inorganic polymer and organic polymer. First, the EDS spectra of a 60 nm by 80 nm area confirmed the coexistence of non-metals (C and N) main-group metal (In), and transition metals, (Fe and Co) elements (n_{Fe}:n_{Co} = 1:1). Besides, the STEM-HAADF image and its EDS elemental mapping (Figure 4.8c) indicated the uniform distribution of both main-group metals (In) and transition metals (Fe, and Co) in the whole area in DN gels. Unlike the separation into two noninteracting phases caused by precipitation, the gel-like double network possesses a homogeneously dispersed multimetal phase.

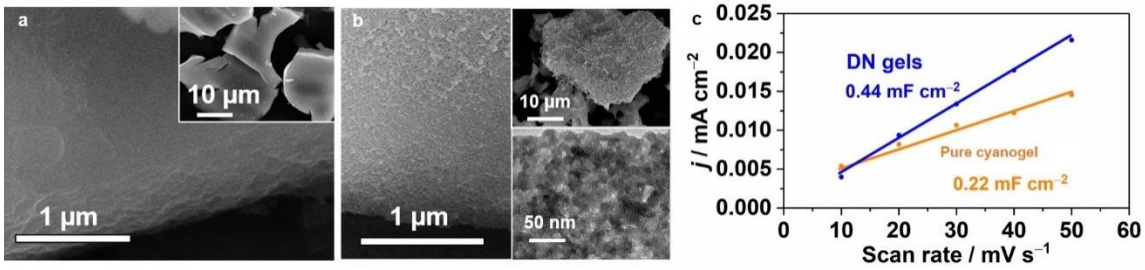

Figure 4.9: SEM images of (a) InFe-CCP and (b) double-network gels. (c) ECSA of DN gels and InFeCo-CCP.

Figure 4.9a and b show the SEM images of InFeCo-CCP, DN gels, and PPy gel. Unlike the smooth surface of InFeCo-CCP, a 3D hierarchically porous structure can be observed. HRTEM images from the inset of Figure 4.9b displayed the interconnected nanoparticles and nanopores in DN gels, which is beneficial for improved mass transfer and enhanced electrochemical surface area. Electrochemical surface area (ECSA) is

measured by the electrical double-layer capacitor method, demonstrating an increased ECSA in DN gels, compared with the pure cyanogel.

4.3.2 Electronic modification in hybrid organic−inorganic hydrogel catalysts

To unravel the chemical configuration between Fe centers in CCP and conductive polymer chains after the polymerization, XPS and X-ray absorption fine structure (XAFS) were applied. As shown in Figure 4.10a, the Fe 2p3/2 binding energy value in the range 708−711 eV is typical for compounds containing iron atoms at valence states Fe^{II} or/and Fe^{III}. In pure $InFe^{III}Co$-CCP, Fe 2p3/2 spectra give maxima at 708.0 eV (corresponding to the Fe^{III}–CN), and the peak in DN gels is 706.9 eV. Also, peaks of double-network gels in Fe $2p_{1/2}$ spectra exhibit similar features with $InFe^{II}Co$-CCP.

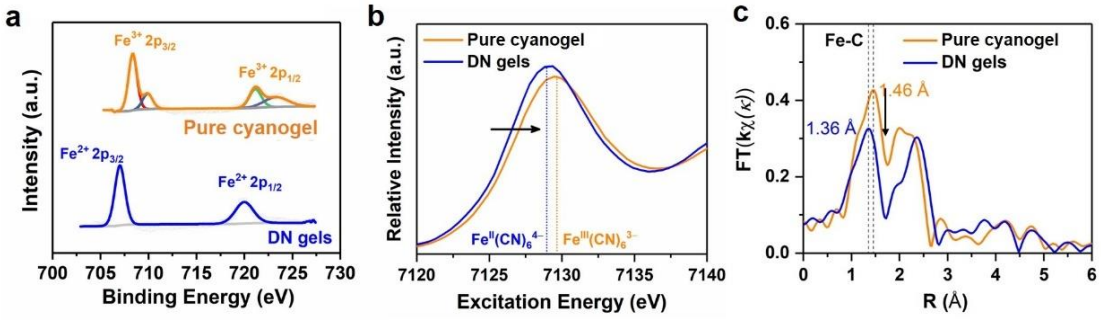

Figure 4.10: (a) XPS spectra of InFeCo-CCP (InFeCo-cyanogels) and double-network gels. (b) XANES and (c) EXAFS of double-network gels, InFeCo-CCP.

Synchrotron-based X-ray absorption spectroscopy, an advanced characterization sensitive to the partial electronic structure and the local geometry around the selected absorber, is quite helpful to monitor the change of the chemical state and atom configuration. Figure 4.10b shows the iron K-edge X-ray absorption near-edge

spectroscopy (XANES) of the InFeCo-cyanogel and the double network gels, using the standard iron foil and Fe_2O_3 as the control references. The Fe edge shifts to the lower energy in DN gels, compared with pure cyanogel. The shift in Figure 4.10b reveals the decreased valence of iron after the introduction of PPy, confirming the oxidation reaction with pyrrole molecules and in situ polymerization of pyrrole molecules.

The change of valence was further confirmed by the pre-edge feature of the XANES. The pre-edge profile observed below 7125 eV in Figure 4.11 is replotted on an expanded scale. The XANES of the DN gels presents two pre-edge peaks at 7112.8 and 7116 eV that are the typical fingerprints of the Fe^{2+} oxidation state of $Fe(CN)_6^{4-}$. To maintain the electroneutrality, K^+ will be incorporated after the reduction of Fe.

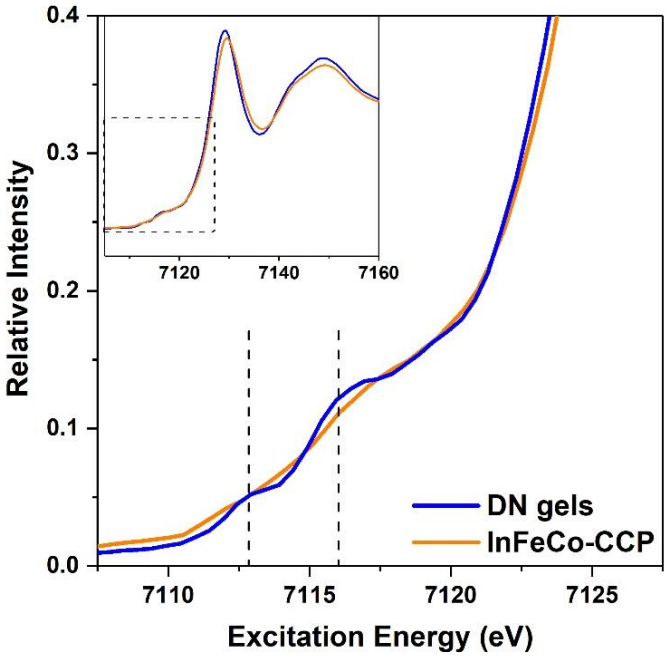

Figure 4.11: The pre-edge structures of DN gels and InFeCo-CCP in Fe K-edge absorption spectra. The XANES of double-network gels shows two pre-edge peaks at 7112.8 eV and 7116 eV are the typical fingerprints of the Fe^{2+} oxidation state of $Fe(CN)_6^{4-}$.[15]

Fourier transforms (FTs) of the extended X-ray absorption fine structure (EXAFS) in Figure 4.10d was performed to investigate if there exists any rearrangement in the local Fe coordination environment. The first peak at about 1.4 Å corresponds to Fe−C bonding in Fe−C≡N−In. The intensity of the Fe−C peak of the DN gels significantly decreases, and the peak position shifts to a lower value compared with pure InFeCo-cyanogel. The amplitude reduction of peaks at 1.4 and 2.0 Å demonstrates the increased atom distortion of Fe−C≡N bonds and the surface structural disorder after the introduction of PPy in DN gels, suggesting the less coordinated −C≡N and more coordinated water on Fe atoms. The decreased crystallinity is in accord with XRD and SAED data.

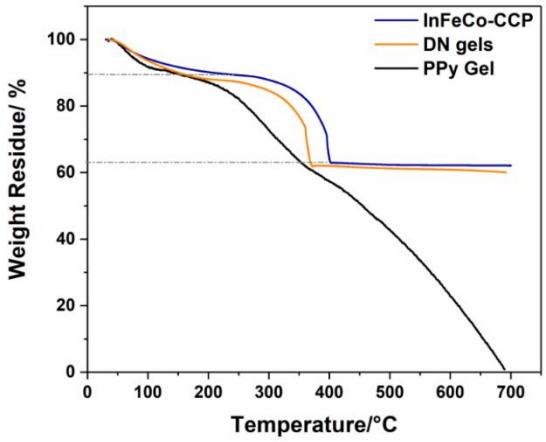

Figure 4.12: TGA curves of DN gels, InFeCo-CCP, and DN gels testing from room temperature to 700 ℃.

TGA was conducted to measure the composition of PPy and cyanogels in DN gels. Staring from the temperature of 25°C to 200°C, all three samples show an initial weight loss, which can be attributed to the evaporation of water molecules and the removal of unreacted monomers from their surface. The second weight loss starts from 320°C to 400°C for InFeCo-CCP and DN gel samples, while 230°C to 700°C for PPy sample,

corresponding to the decomposition of the backbone of the polymer chain. According to the difference in the final weight between DN gels and CCP, the weight percentage of conductive polymers is about 2.5%. The inorganic CCP gel is the dominant part and PPy mainly acts as the conductive additive. It should be noted that the decomposition rate of DN gels is faster than pure CCP (around 50 °C), suggesting more reactive CCP polymer chains in DN gels owing to its high penetration with PPy chain, consistent with our FTIR and ED results.[106]

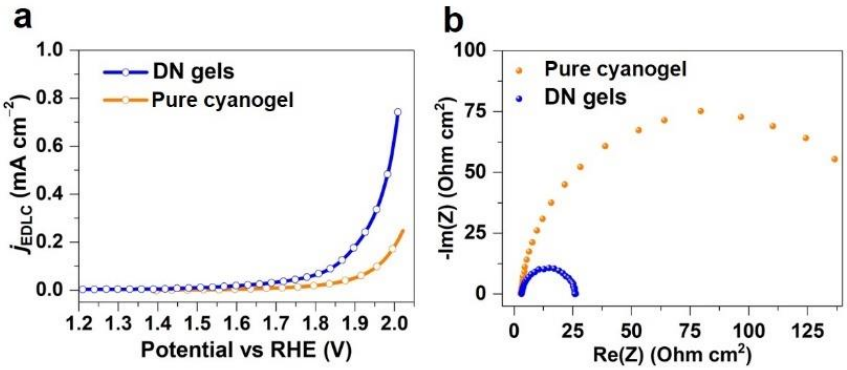

Figure 4.13: (a) LSV (polarization) after the ECSA normalization and (b) EIS curves of double-network gels and pure InFeCo cyanogel.

To study the conductive effect of PPy conductive polymers, EIS was conducted on InFeCo-CCP and DN gels in Figure 13a. DN gels show less than 25 Ω cm^{-2} under 1.8 V, significantly smaller than pure cyanogel, implying improved mass transport within the 3D continuous nanostructured framework.

The intrinsic catalytic activity of pure cyanogel and DN gels is further studied based on the normalized OER catalytic activity. The current density in the electrochemical double-layer capacity (EDLC) test was normalized by the electrochemically active surface area (ECSA). DN gels exhibit a more intrinsically active catalytic property with the

normalized current density of 0.2 mA cm^{-2}@1.9 V vs RHE. From the above EIS and electrochemical double-layer capacity investigation, though possessing lower crystallinity, DN gels show higher conductivity and faster ion transfer kinetics, in comparison to the pure inorganic polymer, resulting in the enhanced ESCA and intrinsic catalytic activity.

4.3.3 Acidic OER of hybrid organic−inorganic hydrogel electrocatalysts

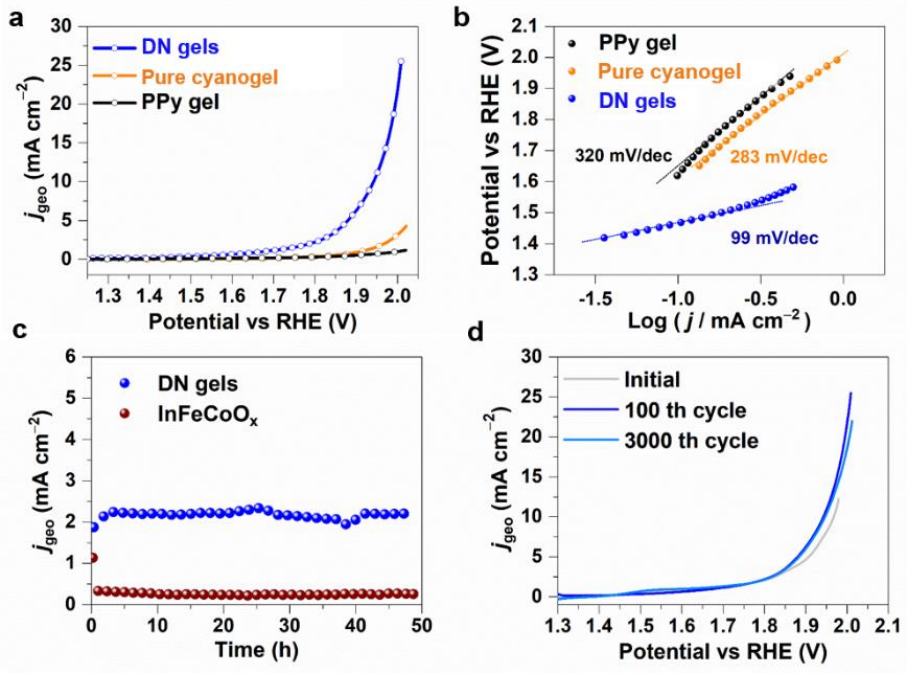

Figure 4.14: (a) LSV curves and (b) Tafel slopes of double-network gels, InFeCo-cyanogel, and PPy gel. (c) Chronoamperometric measurement of double-network gels and InFeCo- cyanogel for 50 h. (d) Cycling stability test.

Based on the above modification of cyanogels, oxygen evolution catalysis in the acidic medium is investigated to evaluate the activity and stability of DN gel electrocatalysts. The pure cyanogel sample and PPy/CCP gels via mechanical mixing require additional overpotential of 220 mV and 180 mV, respectively, to reach the same

current density of the DN gels (1.68 V@1 mA cm^{-2}), as displayed in Figure 4.14a. The difference in catalytic activity can be ascribed to the more active sites arising from the highly penetrated conductive polymer in the cyanogel. Tafel slopes, as shown in Figure 4.14b, also exhibit improved electrocatalytic water oxidation activity in DN gels with the Tafel slope of 98 mV/dec. A smaller Tafel slope is an indicator of good electrocatalytic kinetics, since a small value of Tafel slope means current density can increase faster with faster reaction kinetics.

Stability is another important indicator to evaluate electrocatalysts especially in the case of acid OER catalysis. The long-term test in pH=0 H_2SO_4 was conducted to study the stability property of the DN gel materials. As shown in Figure 4.14c, the DN gel electrocatalyst could maintain no less than 2.0 mA cm^{-2} under 1.75 V (vs RHE) over 50 hours, which retains 93.4% of the highest current density, while the corresponding oxides exhibit poor electrocatalytic stability with less than 0.2 mA cm^{-2} current density (Figure 4.14c, the current density is mostly contributed by glassy carbon electrode). Additionally, after the long-term cycling test of over 3000 cycles, no detectable degradation is observed (Figure 4.14d). Typically, earth-abundant elemental Fe, Co, and their oxides are considered unstable in acidic electrolytes. The ultrahigh acidic stability of the DN gel materials can be attributed to the −C≡N− bonding with both ultrahigh chemical and electrochemical stability, along with the good electrochemical compatibility of PPy.

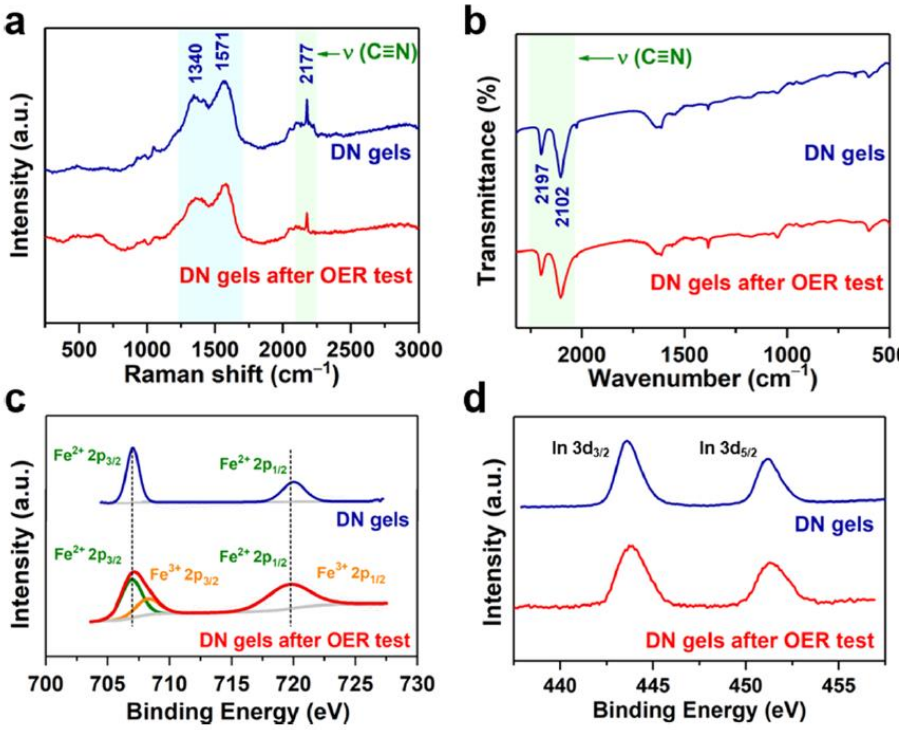

Figure 4.15: (a) Raman, (b) FT-IR, and (c) Fe 2p and (d) In 3d XPS spectra of the double-network gel electrocatalyst before and after OER cycling in the pH = 0 aqueous electrolyte.

The composition stability of DN gels was investigated by a series of surface analyses before and after oxygen evolution electrocatalysis in strong acid. Raman spectroscopy is a high precision technique to study cyanide-based complexes of Fe−C≡N−M type thanks to a very strong signal in the 2000−2200 cm^{-1} range. In the ex-situ Raman test, no peak shift is detected for DN gels after the OER test under an acidic medium, which is similar to other PBA electrocatalysts.[101] On the other hand, double peaks at 1340 and 1571 cm^{-1} are maintained, attributed to the antisymmetric in-ring C−N stretching and C≡C vibrations of PPy, indicating the chemical composition of the cyano-bridged coordination polymer and the conductive polymer under oxidative potential is

maintained. Ex-situ FT-IR and XRD data of the DN gel electrocatalyst (Figure 4.15) were also measured, showing no significant differences between fresh and post-OER catalysts in the comparative analysis, demonstrating the bulk stability of DN gels. For oxygen evolution catalysts, the question about the true species is usually raised. XPS, a surface-sensitive characterization, revealed no notable change at the Fe and In edges after catalysis, with only a small amount of Fe^{3+} being detected. The comparative XPS demonstrates the DN gels after water oxidation maintain all Fe 2p3/2 peaks before 708 eV and Fe 2p1/2 peaks before 721 eV, without showing any peak that can be assigned to iron oxide-type structures. Therefore, the formation of new mixed metal oxide ($InFeCoO_x$) can be precluded, and the Fe 2p peak shift can be attributed to the oxidation of the surface Fe^{II}–C≡N–In to Fe^{III}–C≡N–In after electrocatalytic cycling, which is also correlated with the enhanced activities after 100 cycles shown in Figure 4.14d. Similarly, Co 2p, In 3d (Figure 4.15d), and O 1s show no detectable difference between original and post-OER DN gels. N 1s spectra without a visible oxidized N peak indicates the good electrochemical stability of PPy polymer chains, consistent with other recent works on conductive polymers applied for WOCs and other energy-related devices.[84, 107, 108]

ICP-OES was further performed to study the compositional stability of DN gels. The electrolyte at 0-hour, 10-hour, and 20-hour-OER electrocatalysis for both InFeCo-DN gels and $InFeCo_x$ (@1.75 V *vs.* RHE) were collected and properly concentrated to 5.0 mL. The ICP-OES of electrolytes was then conducted. Note that since ICP-OES only give the total concentration of metal iron ($[Fe]_{total}= [Fe^{III}(CN)_6^{3-}]+ [Fe^{II}(CN)_6^{4-}]+[Fe^{3+}]$), unreacted precursor ($Fe(CN)_6^{3-}$) and intermediate ($Fe(CN)_6^{4-}$) will also be included in dissolved Fe concentration. Meanwhile, due to the redox reaction between Fe^{III} and pyrrole and *in-situ* polymerization of PPy, the coordination environment of Fe shows more structural disorder than Co (less coordination number of –C≡N and more coordination number of

water/hydroxy groups at Fe sites, supported by EXAFS), possibly leading to the relatively higher Fe dissolution rate than Co. The ICP result shows that the dissolution of Fe and Co from gels is significantly slower than that of $InFeCo_x$. From all the above post-characterizations, we can conclude no obvious composition change or chemical etching of the DN gels, in terms of bulk phase and surface composition, implying the high durability of hybrid gel double network during long-term OER.

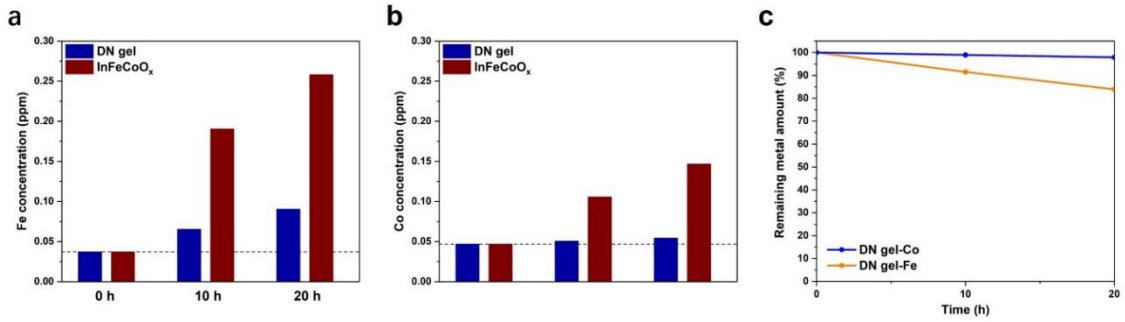

Figure 4.16: ICP-OES measurement of the concentration of (a) Fe and (b) Co from the electrolytes of DN gels and $InFeCo_x$. (c) The remaining metal amount for DN gels and $InFeCoO_x$ during the OER electrocatalysis based on ICP-OES analysis.

To gain fundamental insights into the fundamental catalytic mechanism for InFeCo-CCP gels, DFT calculations were performed to investigate the reaction pathway and corresponding free energy changes during the water oxidation process. Since the potentially most active sites for water oxidation in the inorganic cyano-bridged coordination polymer are Fe/Co atoms exposed on the surface with coordinated water molecules (Figure 4.17a, $(H_2O)_x{-}Fe{-}(CN)_{6-x}$, $(H_2O)_x{-}Co{-}(CN)_{6-x}$, in situ/ operando experiments would be more useful for a deeper understanding of the catalytic mechanism on PBA-type electrocatalysts), only In- $Fe^{II}_{I0.5}Co^{III}_{0.5}(CN)_6$ crystal was considered in calculations to reduce the computing burden, and both $(H_2O){-}Fe(CN)_5$ and $H_2O{-}Co(CN)_5$

were studied as active sites to verify which metal atom has a better catalytic activity in this system (Figure 4.17b and Figure 4.18).

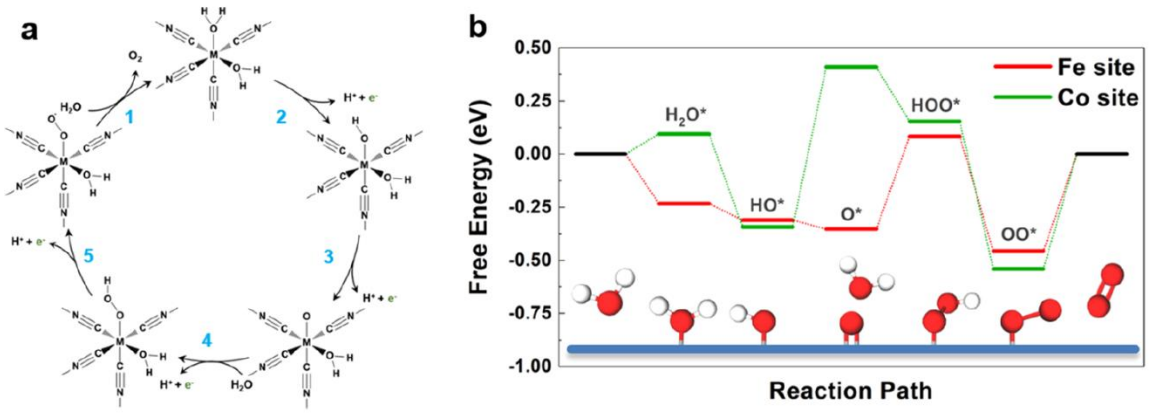

Figure 4.17: (a) Proposed OER mechanism for defect-rich cyano-based OER electrocatalyst and (b) corresponding calculated free energy diagram at the equilibrium potential on Fe and Co sites in InFeCo-CCP.

The OER process involves the following multiple steps starting from the free water molecules: $H_2O \rightarrow H_2O^* \rightarrow HO^* \rightarrow O^* \rightarrow HOO^* \rightarrow OO^* \rightarrow$ free O_2, and four of them are proton−electron coupled reactions as shown in Figure 17a, exhibiting the similarity of the OER reaction pathway on PBA and other homogeneous catalysts, where the O−O bond formation occurs through nucleophilic attack of a water molecule to the electron-deficient oxo/oxyl species generated. The result of the free energy changes for these six steps at the equilibrium potential (U_{RHE} = 1.23 V) is shown in Figure 4.17b, suggesting Fe sites exhibit a mediated adsorption−desorption feature, compared with Co sites. The RDS on Fe is the desorption process of OO* to O_2 and the theoretical onset potential is calculated to be 0.457 V which is close to the experimental results. Since the theoretical onset potential is increased to 0.752 V for oxygen evolution on Co sites with a

different rate-limiting step (HO* → O*), it is the clear-cut conclusion that the Fe sites in InFeCo-CCP have a better catalytic performance for OER and are more likely to be the active sites in the practical catalytic process.

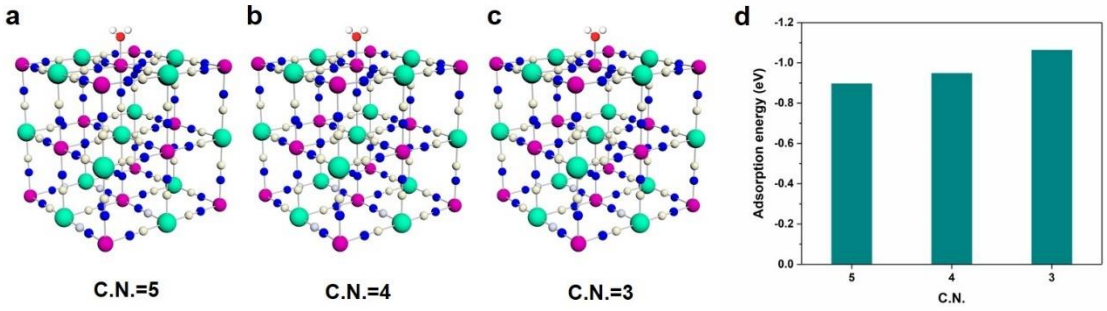

Figure 4.18: Calculated adsorption energies for H_2O molecules on Fe sites (top center) with different coordination numbers.

To unravel the potential correlation between the coordination number of Fe atoms and OER catalytic activity in cyano-based materials, DFT calculations were performed on Fe atoms with various coordination numbers (Figure 4.18 a-c. For clarity, coordinated water is omitted except for the adsorbed water). To reduce the computational burden, the (200) crystal face of InFeCo-CCP crystal was chosen as it is proved in XRD results as the most dominant surface in the CCP. Figure 4.18d demonstrated that H_2O molecules exhibited the higher adsorptive energies (absolute values) at a lower-coordinated Fe site (0.947 eV for C.N. = 4 and 1.063 eV for C.N. = 3, Figure 4.18d). This suggested that water molecules prefer to adsorb at low coordinated Fe sites (less than 6), and hence these unsaturated Fe sites can potentially act as OER active sites.

4.4 CONCLUSIONS

The enhanced acidic OER activity of the dual network gel electrocatalysts can be ascribed to the strong synergistic effects of cyno-coordinated cyanogels and conductive polymers. First, owing to the M''−C≡N−M' unit, the nonnoble-metal-based cyano-bridged coordination polymer displays ultrahigh electrochemical stability for acidic OER. Second, gel characteristics, caused by the abundant coordinated water/-OH and lattice vacancies/defects after the main group metal incorporation, enable the homogeneously dispersed multimetal phase in the electrocatalyst materials, and the 3D hierarchical porous structure allows the enhanced electrolyte diffusion, giving rise to an easier release of evolved molecular oxygen. Third, because of the in-situ polymerization of PPy and simultaneous cyano-polymerization, the interpenetrated dual network increases the structural disorder and generates more unsaturated transition metal atoms as the OER active sites. Meanwhile, the highly penetrated conductive polymer in the cyanogel matrix facilitates the electron transfer through the 3D open structure, enlarging the over ECSA and thus favoring OER activity on DN gels.

To summarize, a hybrid organic−inorganic polymeric dual-network gel electrocatalyst is demonstrated in this chapter. XAFS and XPS spectra indicate a synergistic interplay between the inorganic coordination polymer and the organic polypyrrole polymer in the high penetration of the double network with unsaturated atoms and more dangling bonds for water oxidation catalysis. The enhanced water oxidation properties can be ascribed to the increased electrochemical surface area induced by the structural disorder and enhanced electron transport. The dual-tuning strategy including structural design and electronic modification applied in hybrid gel catalysts demonstrates an alternative insight into seeking for efficient and stable WOCs as alternatives to noble metal catalysts and opens up opportunities to develop cost-effective acid water electrolysis.

From the above example of hybrid gel electrocatalysts, the advantages of gel electrocatalysts are highlighted. Compared with conventional electrocatalysts suffering inferior electrolyte penetration and electron transports, gel electrocatalysts provide promising opportunities for advanced electrocatalysis, combining the features of interconnected porous architectures, compositional and structural tunability, ease of functionalization, and high wettability for ion transfer in aqueous electrolyte.

Chapter 5: Structural engineering and electronic tuning of Gel-Derived Alloys for Electrocatalytic Ammonium Synthesis[3]

5.1 INTRODUCTION TO HYDROGEL-DERIVED MATERIALS

Nanostructured gel networks have recently been investigated as an ideal platform to develop novel material systems. As discussed above, nanostructured cyanogels open up opportunities to develop technologically and economically viable acid water oxidation electrolysis. Moreover, since starting materials can be uniformly mixed at molecular or nanoparticle levels before the gelation/polymerization, gel materials are considered as ideal precursors to synthesize the complex materials, such as binary/ternary/quaternary metal oxides,[109] complex alloys,[110] and carbon materials[78] (Figure 5.1). Many gel-derived frameworks exhibited high catalytic activities for various electrochemical reactions, owing to the optimized composition design and unique hierarchical structures inherited from nanostructured gels. More importantly, due to the high compositional tunability of gels and their derivatives by introducing functional dopants in gels or gel-derivatives, the modulation of the electronic structure of catalysts can be achieved.

[3]**Z. Fang**, Y. Qian, P. Wu, G. Yu, 'Boosting Nitrogen Reduction to Ammonia on Gel-Derived 3D Bismuth by Optimizing Nitrogen Adsorption and Desorption', ***Angew. Chem. Int. Ed.*** 60, 4275 (2021).
Z. Fang†, H. Shi†, X. Zhang, F. Li, Y. Tang, Y. Zhou, P. Wu, G. Yu, "Double-Network Nanostructured Hydrogel-Derived Ultrafine Sn–Fe Alloy in 3D Carbon Framework for Enhanced Lithium Storage", ***Nano Lett.*** 18, 3193 (2018).
Y. Guo†, J. Bae†, **Z. Fang**†, P. Li†, F. Zhao, G. Yu, 'Hydrogels and Hydrogel-Derived Materials for Energy and Water Sustainability', ***Chem. Rev.*** 120, 7642 (2020).
Z. Fang participated in the experimental work and the preparation of manuscripts.

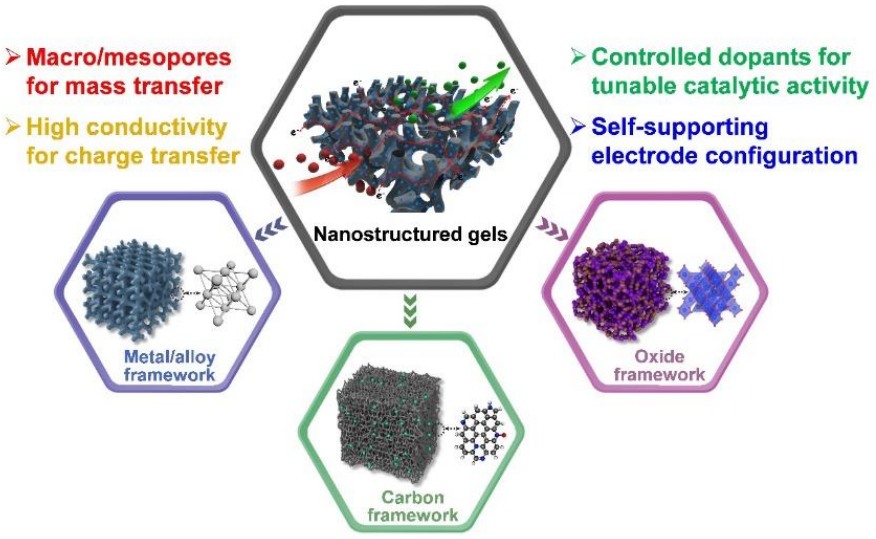

Figure 5.1: Schematic illustration of the key features of gels and their derivatives for electrocatalysis, including macro/mesopores for mass transfer, good electrical conductivity for charger transfer, controlled dopants for tunable catalytic activity, and self-supporting electrode features.

Strategies to fabricate functional gel derivatives typically involve the drying process, calcination/thermal treatment, or chemical activation. Some special drying techniques, such as freeze-drying and supercritical drying process, are frequently employed to preserve the hierarchical structure of gels. By controlling annealing time, temperature, and atmosphere, heat treatment can alter the physical and chemical properties of products, such as the crystallinity and particle size of metal oxides or alloys, the graphitization of carbon frameworks, the porosity and surface areas of final materials, and heteroatom dopants in gel-derived networks. The derivatives incorporate the advantageous features of highly porous structure with large surface area, uniformly distributed active species, effective mass/charge transfer, rationally controlled dopants, etc., making them promising materials for HER, OER, ORR, and more.

Among these gel derivatives, metals and alloy compounds containing one or more metal or non-metal elements, displayed the improved properties of strength, toughness, corrosion resistance, and conductivity for various applications.[79, 82, 109] Compared with conventional approaches (such as high-temperature melting, electrochemical deposition, and electroless plating) mostly yielding bulky and compacted solids with low surface areas and insufficient active sites, gel-derived alloys have been considered as promising electrocatalysts due to the intrinsic advantages. Those metals/alloys inherit many features from aerogel precursors, including 3D interconnected backbones, the decreased particle size with more defects and strain sites, as well as highly porous structure with large surface area and effective mass transfer. Moreover, metallic characteristics of gel-derived metals/alloys allow faster electron transfer.

Although noble metals are regarded as the most efficient electrocatalysts for diverse important reactions including oxygen reduction, hydrogen evolution, oxygen evolution, and nitrogen reduction, it is increasingly important to design more cost-effective catalysts with a minimum amount of expensive noble metals. Alloying noble metals with early transition metals provides the possibility to both decreases the noble-metal composition and further improve the electrocatalytic activity and durability owing to the modified electronic structures of noble-metal atoms.[111] On cyanogel scaffolds, noble metals (M''= Pd, Pt) and transition metals (M''= Fe, Co, Ni) can be incorporated in the form of M'−N≡C−M''. Using Pd−M'' and Pt−M'' cyanogels as precursors, the wet-chemical reduction process could serve as a facile and general route toward advanced Pd- and Pt-based alloy electrocatalysts with favorable framework structures and high alloying degrees.[112]

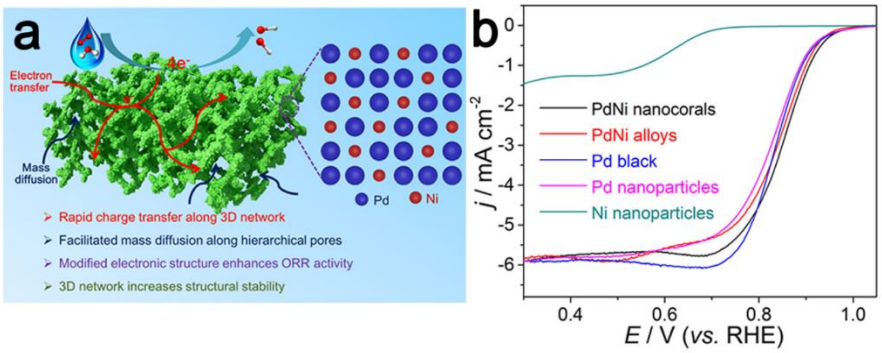

Figure 5.2: Electrocatalytic oxygen reduction activity of the cyanogel derived Pd−Ni nanocorals.

As mentioned in the previous chapters, cyanogel can serve as a host to contain various functional materials. Wu et al. developed a wet-chemical reduction method to synthesize Sn-Ni alloys using a cyanogel/ graphene oxide (GO) double-network hydrogel as the precursor.[113] The cyano-bridged Sn(IV)-Ni(II) coordination polymer hydrogels were highly interpenetrated with GO gels, which were simultaneously reduced to produce Sn-Ni/C double framework. In the final product, the Sn-Ni alloy scaffold and graphene architecture were physically intertwined via hydrogen bonds and meanwhile chemically bonded via Sn-O-C bonds. Sn(IV)-Ni(II) cyanogel network can be uniformly integrated into GO network in Sn(IV)-Ni(II)/GO aerogel. The microscopic structure of the Sn-Ni/G double framework exhibited that Sn-Ni alloys were composed of nanodendrites with a diameter of around 10 nm and firmly attached to graphene sheets. In this case, metal alloys were supported on graphene networks to achieve a high surface area and thus realize the uniform dispersion of the active sites. Pure metallic aerogels, as unsupported materials, achieve integrated catalyst layers via the direct contact of the electroactive species with the conductive substrates, resulting in satisfactory stability upon electrochemical cycling.

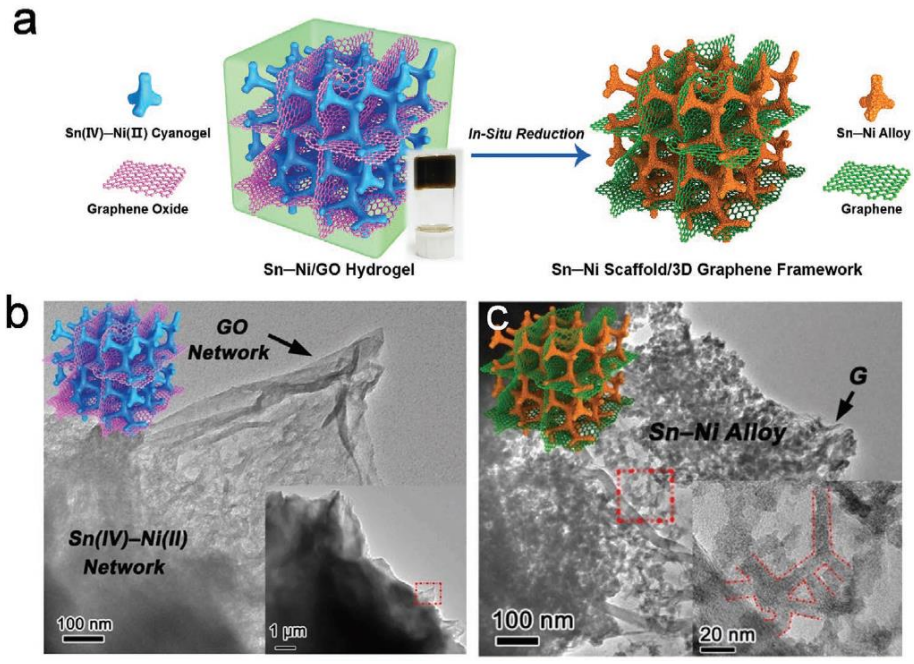

Figure 5.3: Synthetic routes for gel-derived metal/alloys. (a) Synthesis of Sn-Ni/graphene gels. (b) TEM images of Sn-Ni/GO double-network aerogels and (c) Sn-Ni/graphene dual framework.

Besides aqueous solutions, the ligand-substitution reactions and following alloy formation could also occur in organic solvents. For example, the coordination reaction between $SbCl_3$ and $K_2Ni(CN)_4$ in dimethylformamide (DMF) generates an Sb−Ni cyanogel with green semi-transparent nature, and graphene oxide is in situ immobilized within the gel framework to construct a hybrid cyanogel. The uniformly distributed GO, Sb, and Ni species in the hybrid cyanogel are concurrently reduced, ensuring the formation of homogeneous Sb−Ni−C ternary frameworks.

5.2 INTRODUCTION TO ELECTROCATALYTIC NH_3 SYNTHESIS AND BI-BASED NRR CATALYSTS

Ammonia (NH_3) is an essential chemical for the agricultural industry and a convenient hydrogen carrier as a carbon-free fuel.[114] However, industrial ammonium production process, Haber-Bosch reaction (1st artificial nitrogen fixation process), is an energy-intensive process (high temperatures, 350–550 °C, and high pressures, 150–350 atm), consuming 1%–2% of global energy and producing 3% global CO_2.[6, 115] The electrochemical nitrogen reduction reaction (NRR) is a sustainable strategy that can generate NH_3 from air and water when powered by sustainable electricity.[116] Unlike the industrial Haber-Bosch process, electrocatalytic NRR serves as an alternative, renewable, and less energy-intensive approach to producing NH_3 under ambient conditions. In this regard, NH_3 synthesis driven by renewable energy has sparked widespread research interests in recent years. Nevertheless, to date, the NH_3 yield rate and Faradaic efficiency of electrochemical nitrogen fixation are still low in most recent relevant articles, mostly due to the high energy required for the activation of N≡N bond with high bond energy and the severe competition with the H_2 evolution reaction. Some noble-metal-based catalysts (Au, Ru, Ag, etc.) are proved to be active for NRR electrocatalysis, but the prohibitive costs seriously impede their widespread use in practical applications.[117] Thus, seeking effective and economical precious-metal-free NRR electrocatalysts currently attracts much research attention.

Bismuth, as the most metallic element in the N(VA) group, has recently been reported for efficiently catalyzing N_2 fixation. Density functional theory (DFT) modeling has revealed that the potential-determining step (PDS) for nitrogen fixation on Bi is the protonation of adsorbed $*N_2$ ($*N_2 + H^+ + e^- \rightarrow *NNH$), which can provide a lower free-energy change for PDS than typical transition metal catalysts, and even small than Au.

More importantly, different from most transition metals, Bi with weak binding with H_{ad} atoms allows HER process less active on the surface of Bi, and thus Bi exhibits desirable intrinsic electrocatalytic activity towards NRR. However, as a semi-metal with the semiconductive feature, the inferior electrical conductivity of Bi inhibits the electron transfer during electrocatalysis. To improve the electrocatalytic activity of Bi-based materials in electrochemical energy storage and conversion, hybrid with more conductive materials (such as conductive carbon black) is an effective method to enhance electrical conductivity. For another, developing Bi alloys is another potential strategy to improve the intrinsic activity of Bi-based electrocatalysts. The utilization of alloying or introducing surface strain can also optimize the adsorption/desorption energy of reactants on alloy-based nanocatalysts. Alloying Bi with other more conductive metals not only can enhance the intrinsic electrical conductivity but also possibly facilitate the electron transfer during the electrochemical reaction. Furthermore, in the aspect of the binding ability with N_2, despite the stronger bonding between *NNH intermediate and Bi, Bi cannot absorb N_2 in the first step of nitrogen fixation, which significantly increases the energy barrier of nitrogen reduction. Substitution of Bi with heteroatoms is able to tune the electronic configuration of elemental Bi, and thus optimize the N adsorption energy of Bi-based electrocatalysts.

To design highly efficient electrocatalysts, apart from the improvement of the intrinsic activity by electronic tuning, it is also critical to increase the number of active sites. Amorphous catalysts in a metastable state with disordered structure have currently attracted increasing attention. Modulation of the crystallinity may create unusual atomic arrangements, and meanwhile, introduce defective sites (vacancies) and under-coordinated dangling bonds. Consequently, amorphous catalysts usually exhibit better catalytic activities compared with their high-crystalline counterparts, owing to more active sites on

the surface vacancies. For example, amorphous Au nanoparticles hybrid with reduced graphene oxides are reported to show enhanced NRR activities compared with its crystalline counterpart.[118, 119] Our previous work reported an amorphous $Bi_4V_2O_{11}$ electrocatalyst induced by CeO_2. Thanks to the improved active sites, amorphous $Bi_4V_2O_{11}$ can catalyze NRR with an NH_3 yield rate of 23.21 mg h^{-1} mg_{cat}^{-1}.[120] However, due to the instability of the metastable amorphous materials and the low tunability during the synthetic process of nanostructured alloys, few amorphous alloy catalysts, especially Bi-TM alloy catalysts, have been reported.[121-124]

As an emerging material over the past decade, metal-organic framework (MOF)-based material possesses high compositional tunability, high porosity, and good thermodynamic structural stability, allowing its wide applications from energy storage, energy conversion, to sensors, and water purification.[125] MOF-derived functional materials usually maintain the original structure of MOF, exhibiting nanoporous features for various electrochemical applications after the loss of organic moieties. In this regard, Bi-based CCP can serve as an ideal template (or precursor) to generate a 3D interconnected framework including Bi metals and other metals with uniform distribution. Compared with traditional Bi-based MOFs under higher temperature or organic synthetic conditions, Bi-based CCPs can be quickly synthesized at room temperature.[126, 127] Even more intriguingly, Bi-CCPs and their derivatives show high controllability with different M' with-[Bi-N≡C-TM]- (M'=Ni, Co, Fe, etc.), enabling the synthesis of alloys with uniform atom distribution.

5.3 MATERIALS SYNTHESIS AND CHARACTERIZATION DETAILS

5.3.1 Synthesis of cyano coordination polymers

The general synthesis of metal cyano coordination polymers (CCPs) have been discussed in Chapter 4.2 For the synthesis of Bi-Ni-CCP (unit: -[Bi-N≡C-Ni]-), 0.25 M $Bi(NO_3)_3 \cdot 5H_2O$ and 0.25 M $K_2Ni^{II}(CN)_4$ diethylene glycol (DEG) solution were used. For the synthesis of Bi-$Fe^{(III)}$-CCP (unit: -[Bi-N≡C-Fe]-), 0.25 M $Bi(NO_3)_3 \cdot 5H_2O$ and 0.25 M $K_3Fe^{III}(CN)_6$ DEG solution were used.

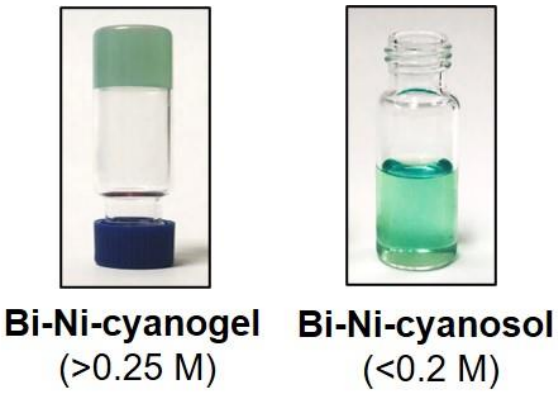

Figure 5.4: Digital images of Bi-Ni-cyano-gel and sol by controlling the concentration in DEG solvent.

5.3.2 Synthesis of 3D amorphous BiNi electrocatalyst

The 3D porous amorphous BiNi alloy framework was synthesized through a $NaBH_4$ reduction process by using Bi-Ni-CCP as precursors. Specifically, a DEG solution of 1 M $NaBH_4$ was added to Bi-Ni-CCP DEG-gel, and the resulting reaction systems were allowed to stand for different reaction times. The black products were washed using deionized water and ethanol and dried, yielding the a-BiNi frameworks. It should be noted that although the reaction time of fully-amorphized alloy is around seven days, the productivity of this

reaction is very large, and can be scaled up to gram-scale per batch. For comparison, amorphous Ni and crystalline Bi were synthesized through similar $NaBH_4$ reduction processes by replacing Bi-Ni-CCP DEG-gel with $Ni(NO_3)_2$ DEG solution and Bi-Fe-CCP DEG-gel, respectively.

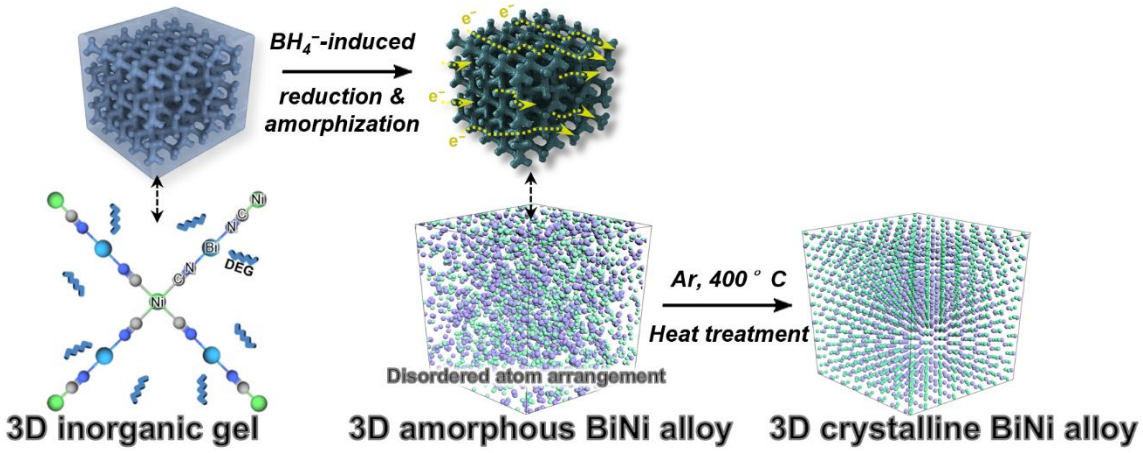

Figure 5.5: Schematic illustration of the synthesis of 3D amorphous BiNi and 3D crystalline BiNi.

5.3.3 Synthesis of 3D crystalline BiNi electrocatalyst

3D crystalline BiNi was synthesized by heat treatment of 3D amorphous BiNi in Ar at 400°C for 2 hours. Similarly, crystalline Ni was synthesized by heat treatment of amorphous Ni in Ar. As a control experiment, physically mixed crystalline Bi and amorphous Ni were annealed in Ar at 400°C with a reaction time of 2 hours.

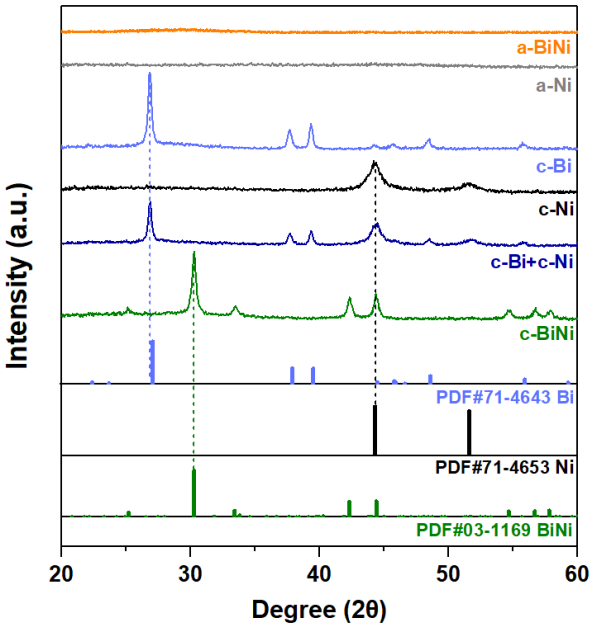

Figure 5.6: XRD patterns of amorphous BiNi (a-BiNi), amorphous Ni (a-Ni), crystalline Bi (c-Bi), crystalline Ni (c-Ni), physically mixed high-crystalline Bi and Ni (c-Bi + c-Ni), crystalline BiNi (c-BiNi).

	Precursor	*Synthetic method*
a-BiNi	Bi-Ni-CCP	$NaBH_4$ reduction in DEG
a-Ni	$Ni(NO_3)_2$	$NaBH_4$ reduction in DEG
c-Bi	Bi-Fe-CCP	$NaBH_4$ reduction in DEG
c-Ni	a-Ni	Heat treatment in Ar, 400°C, 2h
c-Bi + c-Ni	c-Bi + a-Ni	Heat treatment in Ar, 400°C, 2h
c-BiNi	a-BiNi	Heat treatment in Ar, 400°C, 2h

Table 5.1: Synthesis of amorphous BiNi alloy, crystalline BiNi alloy, and other metals.

5.3.4 Materials characterization

Powder X-ray diffraction (XRD) patterns were collected on a Philips vertical scanning diffractometer to identify the phase of the as-synthesized samples. Scanning electron microscopy (SEM), energy-dispersive X-ray spectroscopy (EDS), high-resolution transmission electron microscopy (HRTEM, JEOL JEM-2010F coupled with an energy-dispersive X-ray spectrometer), and selected area electron diffraction (SAED) were used to characterize the composition and morphology of the samples. The FEI G3 Titan Themis transmission electron microscope is utilized for the elemental mapping operated.

5.3.5 Electrochemical measurement

All the electrochemical measurements were performed on the carbon fiber paper (CFP) electrodes (0.25 cm^2 x 2, double-sided area) under identical conditions with the same catalyst mass loading (0.5 mg cm^{-2}): 5 mg of catalyst and 40 µL of 5 wt.% Nafion solution was dispersed in 0.96 mL ethanol solvent by 30 min sonication to form a homogeneous ink with a concentration of 5 mg mL^{-1}.

To avoid contamination from electrodes, CFP was washed using 0.1 M H_2SO_4 and deionized water to remove possible contaminants before the electrochemical test. Nafion 117 membrane was pretreated by heating it in 5% H_2O_2 aqueous solution at 80 °C (1 h) and deionized water at 80 °C (1 h), followed by treatment in 0.5 M H_2SO_4 (1 h) and deionized water for another (1 h). 50 µL of the catalyst dispersion was then transferred onto the CFP electrode *via* a controlled drop-casting approach. NRR electrochemical measurements, cyclic voltammetry (CV), and linear sweep voltammetry (LSV) were conducted in an H-cell using a saturated Ag/AgCl electrode as the reference electrode, a carbon rod electrode as the counter electrode, and the sample modified CFP electrode as

the working electrode on BioLogic VMP-3model. For the LSV test, the polarization curves were obtained by sweeping the potential from -0.61 V to –1.51 V (*vs.* Ag/AgCl electrode in saturated KCl) at a sweep rate of 5 mV s^{-1} in a 0.1 M N_2-saturated Na_2SO_4 aqueous electrolyte. For the general NRR test, a static overpotential was fixed for a certain time during the continuous electrocatalytic process to measure the current density as a function of time. The potentials in this work were converted to a reversible hydrogen electrode (RHE) scale according to the Nernst Equation ($E_{RHE} = E_{Ag/AgCl} + 0.059\ pH + 0.197\ V$; in our case, $E_{RHE} = E_{Ag/AgCl} + 0.610\ V$: the calibration of the reference electrode to the RHE was performed in 0.1 M Na_2SO_4 electrolyte saturated with H_2). To test the electrochemical surface area (ECSA) of catalysts, a rotating disk electrode (RDE) was used as the working electrode (0.071 cm^2, 1600 rpm, Pine Research Instrumentation, USA). The alternating cycling tests were proceeded by switching electrolysis between Ar- and N_2-saturated 0.1 M Na_2SO_4 electrolyte at −0.6 V (vs RHE) with alternating 2-hour cycles. To avoid contamination from the previous cycles, the CFP electrode loaded with a-BiNi catalysts was washed using deionized water after each 2-hour cycle. N_2 and Ar gas (ultra-high purity, 99.999%, Airgas) were cleaned by dilute H_2SO_4 solution (1 mM) to eliminate NO_x and NH_3. To avoid possible contamination, all catalysts and electrolytes were processed at fume hoods with ventilation. Also, masks and gloves were required all the time to prevent interference from human respiration and skin contaminates.

5.3.6 Determination of ammonia

The concentration of produced ammonia was spectrophotometrically determined by the indophenol blue method with modification. 2 mL post-NRR electrolyte was firstly removed from the electrochemical reaction vessel. Then, 2 mL of a 1 M NaOH solution

containing 5wt% salicylic acid and 5 wt% sodium citrate was added, followed by 1mL of 0.05 M NaClO and 0.2 mL of an aqueous solution of 1 wt % $C_5FeN_6Na_2O$ (sodium nitroferricyanide). After 2 h at room temperature, the absorption spectrum was measured using a UV-Vis spectrophotometer. The formation of indophenol blue was determined using the absorbance at a wavelength of 655 nm. The concentration-absorbance curves were calibrated using standard ammonia chloride solutions, which contained 0.10 M Na_2SO_4 as used in the electrocatalysis experiments.

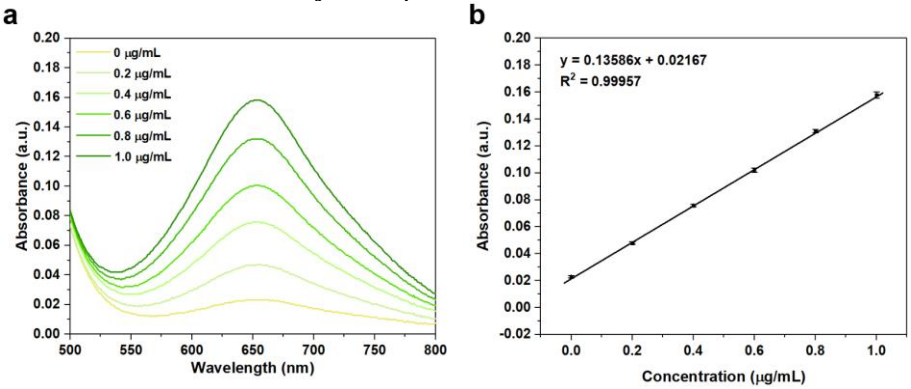

Figure 5.7: Calibration curves in 0.10 M Na_2SO_4 using NH_4Cl solutions of different concentrations from 0 to 1.0 μg mL^{-1}: (a) UV-vis of indophenol assays after incubated for 1 hour and (b) calibration curve used for estimation of NH_3 concentration. The absorbance at 655 nm was measured by UV-Vis spectrophotometer, and the fitting curve shows good linear relation of absorbance with NH_3 concentration.

5.3.7 Determination of hydrazine

The hydrazine presented in the electrolyte was estimated by the method of Watt and Chrisp. A mixture of para-(dimethylamino) benzaldehyde (5.99 g), HCl (concentrated, 30 mL), and ethanol (300 mL) was used as a color reagent. The calibration curve was plotted as follows: A series of reference solutions were prepared by pipetting suitable volumes of

the hydrazine hydrate-nitrogen 0.1 M HCl solution in colorimetric tubes, and then diluted 0.1 M Na_2SO_4 electrolyte to 5 mL. The above-prepared color reagent was then added. The absorbance of the resulting solution was measured at 457 nm, and the yields of hydrazine were estimated from a standard curve using 5 mL residual electrolyte and 5 mL color reagent. Absolute calibration of this method was achieved using hydrazine monohydrate solutions of known concentration as standards, and the fitting curve shows good linear relation of absorbance with $N_2H_4 \cdot H_2O$ concentration.

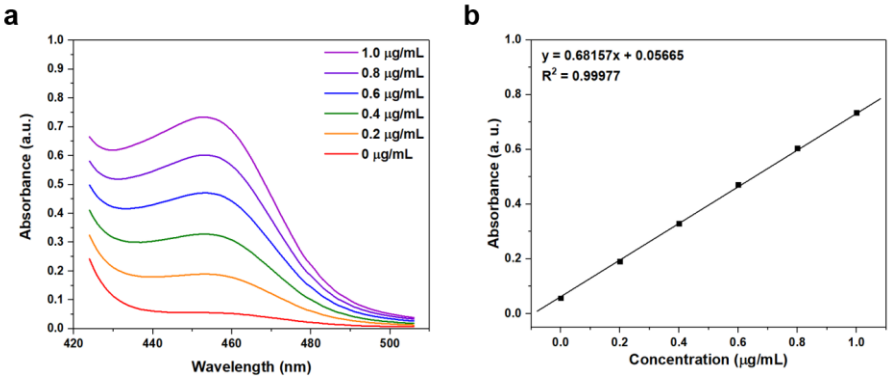

Figure 5.8: (a) UV-vis spectra and (b) calibration curve of N_2H_4 with different concentrations from 0 to 1.0 μg mL^{-1} using p-$C_9H_{11}NO$ as the indicator.

5.3.8 Estimation of the maximum amount of NH_3 impurity from N_2 flow

To calculate the maximum amount of NH_3 that can be possibly introduced to the electrolyte, here we assume all of the impurities are ammonia in 99.999% ultra-high purity of N_2. For a 2-hour NRR test, the total flow time is 130 min (including 10 min pre-saturation). Based on ideal gas law, the flow rate (the average flow rate is about 3 sccm) can be converted to 103225 Pa × (3 × 0.000001) m^3/min / (8.3144 $J \cdot K^{-1} \cdot mol^{-1}$ × 298.15 K) = 0.1248 mmol min^{-1}. The total mol of N_2 flowed through the cell can be calculated to be 16.2 mmol. For 99.999% ultra-high pure N_2, the total impurity is less than 1.62 × 10^{-7}

mol. If we assume all of the impurities are ammonia, then the amount of ammonia per test is 2.77 ×10^{-6}g, corresponding to 2.77 × 10^{-6}g / (2 h × 0.25 mg) = 5.51 μg h^{-1} mg_{cat}^{-1}. The result is significantly different from our measurement (0.12 μg h^{-1} mg_{cat}^{-1}), which might be due to the overestimation of the amount of impurity in the gas flow.

5.4 RESULTS AND DISCUSSION

5.4.1 Facilitating electron transfer by alloying Bi with Ni

After substituting half of the Bi atoms with Ni atoms, the rhombohedral structure of elemental Bi transforms into a hexagonal crystal structure. X-ray photoelectron spectroscopy (XPS) was firstly used to study the electronic effect of alloying effect.

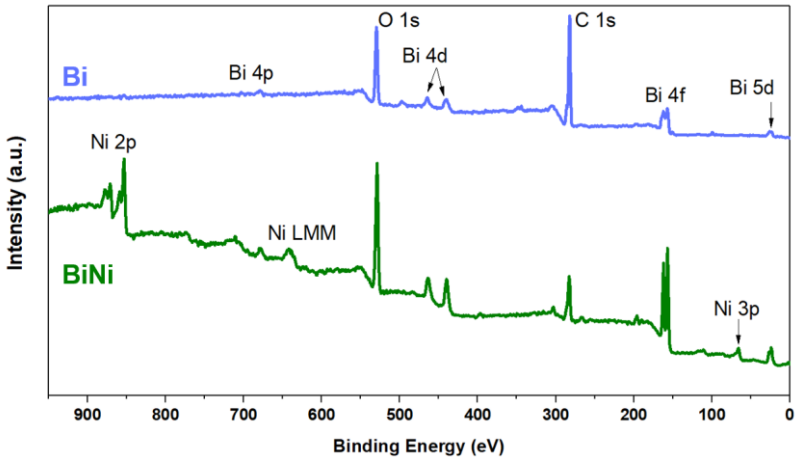

Figure 5.9: XPS survey scan of c-Bi and a-BiNi: Ni 2p and 3p peaks confirmed the introduction of Ni.

Figure 5.10 demonstrated the XPS survey scan of c-Bi and a-BiNi, confirming the introduction of Ni in pristine Bi. From XPS results, the Bi 4f peaks shift to lower binding energies suggested that Bi act as an electron acceptor. Also, the shifts of the Ni 2p XPS peaks to higher binding energies suggested that the electron is transferred from Ni. Recent

works have shown that the NRR is electron-enrichment-dependent in many alloy-based systems,[128] the interaction between bimetallic atoms can alter the electronic states of metal atoms and potentially enhance the catalytic activity. Through the modulation of the electronic configuration, the surface properties and adsorption energy can be modified.

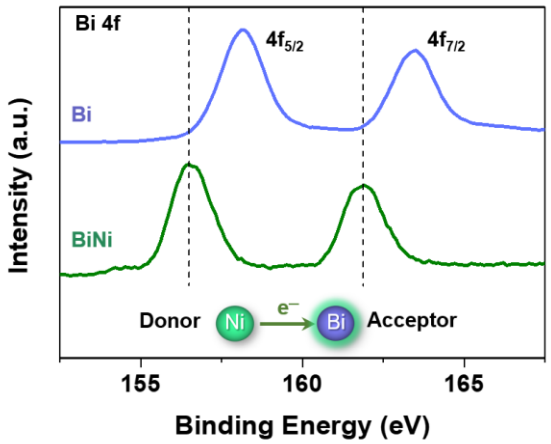

Figure 5.10: XPS Bi 4f spectra of Bi and BiNi alloy: peak shifts to lower energies in Bi 4f and higher energy in Ni 2p peaks, indicating the electron acceptor of Bi and the electron transfer from Ni to Bi.

To gain a deeper understanding of the charge transfer in BiNi alloys, as shown in Figure 5.11, electrochemical impedance spectroscopy (EIS) measurement was performed at -0.6 V. BiNi alloy-based electrode possessed an area-specific impedance of less than 90 $\Omega\,cm^2$, significantly smaller than the Bi-based electrode. The smaller radius of semicircles indicated favorable charge transport across the alloy framework. The enhanced electron transfer can be attributed to the electron transfer from Ni to Bi, as confirmed by XPS results.

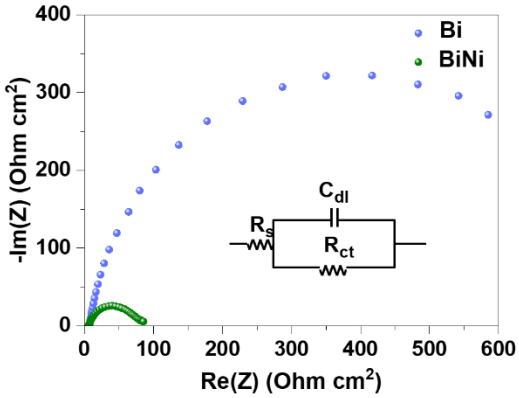

Figure 5.11: EIS spectra of Bi and BiNi: smaller radius of the semicircles indicating improved charge transfer in BiNi.

5.4.2 Chemical adsorption of N_2 on BiNi alloy

As discussed above, Bi-metal only can physically adsorb N_2, which would significantly increase the overall NRR energy barrier. Regulating the electronic configuration of Bi is possible to optimize the surface properties and N adsorption energy of Bi-based electrocatalysts, such as the formation of alloys via the substitution of Bi with heteroatoms.

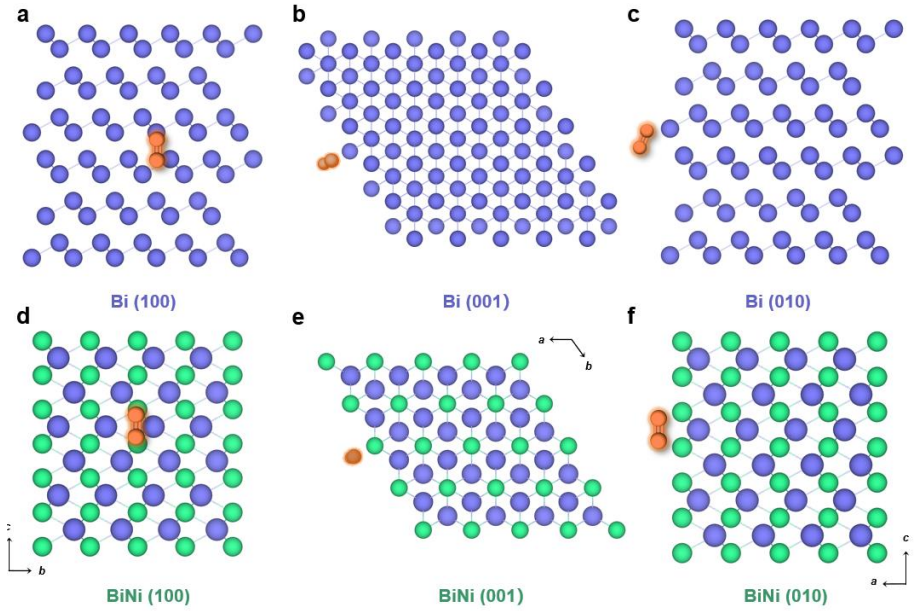

Figure 5.12: Adsorption of N_2 on (100) crystal facets of Bi and BiNi from three directions.

The catalytic activity was investigated by DFT simulations. Computational modeling revealed that Bi-metal cannot adsorb molecular N_2 at any site (Figure 5.12a-c, Figure 5.13a-d). After Ni-substitution, BiNi alloys enable the chemical adsorption of N≡N (Figure 5.13-14), which is stronger compared with physical adsorption, allowing elongated N≡N bond length of 1.17 Å for a chemisorbed N≡N on BiNi (001) compared with that on the elemental Bi (001) (1.11 Å, physical adsorption). Compared with Bi-metal without chemical adsorption, the stronger binding ability of N≡N on BiNi alloy is able to activate N_2 molecules in the following steps.

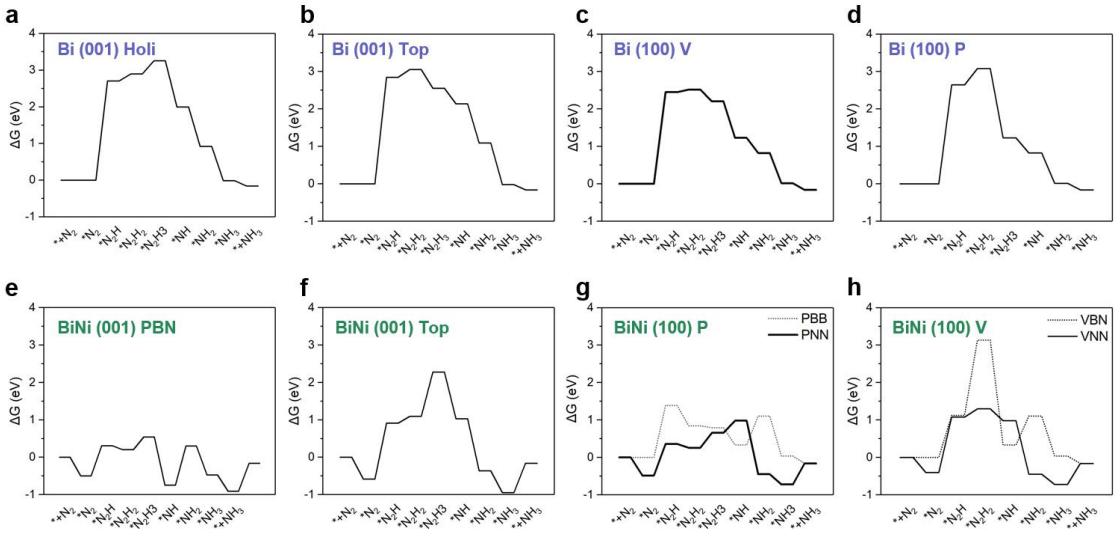

Figure 5.13: Gibbs free energy diagrams of NRR on different low-index crystal facets of Bi and BiNi from DFT calculation. For the Bi surface, molecular N_2 cannot chemically adsorb on (001) or (100) crystal facet, resulting in $\Delta G = 0$ in the first step. In comparison, both BiNi (001) and (100) crystal facets can chemisorb N_2, bringing our improved overall NRR kinetics.

Our preliminary DFT computation results in Figure 5.12 and 5.13 show that Ni-substitution in bismuth can change the surface properties and the adsorption energy of intermediates. On the metals with relatively weak *N adsorptions, including Pt, Au, and Bi, the reaction selectivity is mostly dependent on the competition between the adsorptions of $*N_2$ and *H, and the first-step N≡N bond activation ($* N_2 + H^+ + e^- \rightarrow *NNH$) is universally accepted as the rate-determining step (RDS) of the nitrogen reduction reaction.

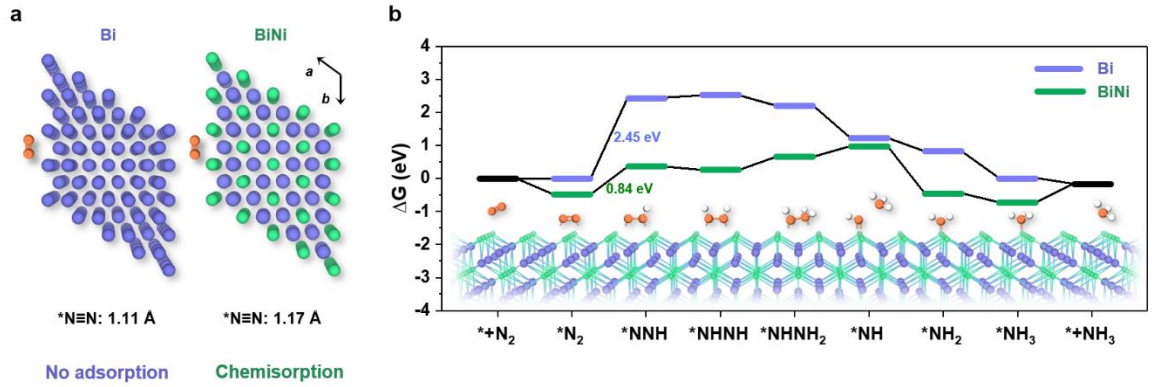

Figure 5.14: Adsorption of N_2 on BiNi alloys versus Bi-metal: (a) Nitrogen (orange) adsorption on Bi and BiNi alloys: Ni-substitution can promote the N_2 adsorption while no adsorption on pure Bi-metal. (b) Energy diagram of NRR process on Bi and BiNi. The RDS is the 2nd step and Ni substitution can effectively modulate the adsorption abilities of nitrogen adsorption.

As demonstrated from DFT calculations in Figure 5.14b, the NRR process on both Bi and BiNi surfaces prefers to follow the associative alternating pathway with a side-on mode. The observation of the highest energy barrier linking reductive protonation of chemisorbed N_2 to *NNH confirmed the RDS is the first N≡N cleavage instead of N-H_x formation, and thus the NRR activity is related to the ΔG_{*NNH}. From Figure 5.14b, we can see ΔG_{*NNH} is 0.84 eV on BiNi (100) surface, significantly lower than that on elemental Bi (100) surface (2.45 eV). In the next several steps of the side-on mode, the *NNH captures the second and third ($H^+ + e^-$) pair and forms NNH_2 and *$NHNH_2$ with the ΔG of -0.10 eV and 0.39 eV. Subsequently, the fourth ($H^+ + e^-$) pair attacks *$NHNH_2$ and split the N≡N bond, leading to the formation of the first NH_3 molecule. The remaining *N is then hydrogenated to produce *NH, *NH_2, and *NH_3 by successively adsorbing three ($H^+ + e^-$) pairs with free energy changes of -1.42 eV, -0.27 eV, and 0.56 eV, respectively, indicating the subsequent hydrogenated processes are relatively facile to happen. In this

regard, from the thermodynamic aspect, one can conclude that alloying with Ni can effectively activate molecular N_2 and modulate the adsorption properties of the active sites, bringing about the potential electrocatalytic NRR capability.

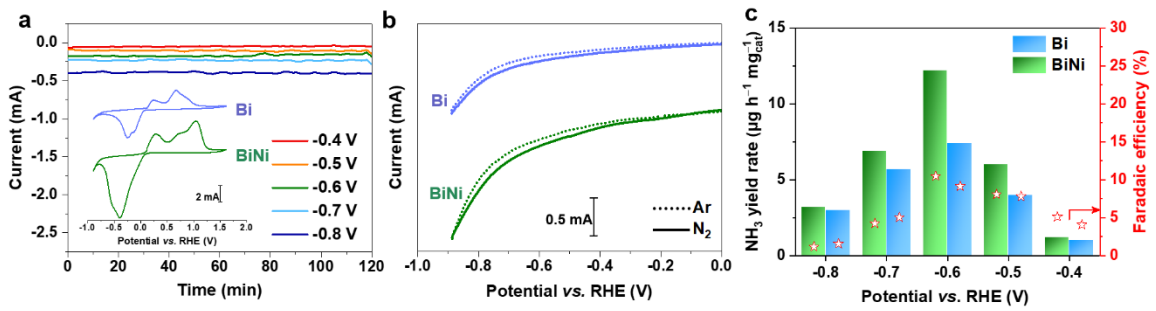

Figure 5.15: Electrocatalytic NRR activity of crystalline BiNi alloys and Bi. (a) CA curves under different voltages from -0.4V to -0.8V and CV curves of Bi and Bi-Ni alloys. (b) LSV curves of Bi and BiNi alloys in N_2 and Ar-saturated 0.1M Na_2SO_4 electrolyte. (c) The yield rate of NH_3 Faradic efficiency from -0.4 V to -0.8 V of Bi and BiNi alloys under N_2 production.

Bi and BiNi alloys were first synthesized via a polymer gel-derived method using Bi-based cyano coordinated polymers (CCPs) as both the precursor. Both Bi and BiNi samples were then treated in the Ar atmosphere at 400 °C, to guarantee similar crystallinity and nanostructures (here we want to focus on the electronic effect and exclude other effects from the surface area). To preliminarily test the NRR activity of Bi-metal and BiNi alloy electrocatalysts, the cyclic voltammetry (CV) was first conducted on carbon fiber paper (CFP) electrodes with a scan rate of 50 mV s^{-1} in a 0.1M N_2-saturated Na_2SO_4 aqueous solution. From the inset of Figure 5.15a, the two oxidation peaks at 0.23 V and 0.65 V (vs. RHE) can be ascribed to the oxidation of metallic bismuth to Bi^{III}. Similar to other Bi-based electrodes,[14, 129] the former is due to the formation of a thin layer of Bi oxide sites, while the latter is related to the thickening of the oxidized product Bi^{III}. A sharp

cathodic peak at -0.39 V can correspond to the reduction of Bi^{III}. For BiNi alloys, there are extra peaks relevant to Ni^{II}/Ni^{III}, suggesting the successful Ni-introduction. The polarization curves of Bi and BiNi were evaluated in both N_2-saturated and Ar-saturated 0.1M Na_2SO_4 electrolyte (Figure 5.15b). The current of the Bi electrode in N_2-saturated electrolyte was higher than that in Ar-saturated electrolyte at the potential ranging from around -0.4 to -0.9V (vs. RHE), indicating that Bi possessed electrocatalytic activity toward nitrogen fixation. Compared with Bi-metals, BiNi alloy shows slightly increased current density, and the difference in two electrolytes (corresponding to the onset potential of nitrogen fixation) begins at around -0.3 V. At the potential below -0.85 V (vs. RHE), the current of BiNi in N_2-saturated Na_2SO_4 approximated to that in Ar-saturated Na_2SO_4. In this case, the hydrogen evolution reaction became the primary electrochemical reaction. The increased current can be ascribed to the increased electrochemical surface area (ECSA) and slightly improved hydrogen evolution process due to the Ni-substitution in the BiNi catalyst.

The electrocatalytic NRR performance of both catalysts was tested in N_2-saturated 0.1M Na_2SO_4. Figure 5.15a shows the chronoamperometry measurement of BiNi from -0.4 to -0.8 V. The concentration of $NH4^+$ in electrolyte after 2-hour NRR was quantified via a calibrated indophenols blue method (Figure 5.10c). NH_3 production on BiNi could be detected at -0.60 V (vs. RHE) with a yield rate of 12.2 mg h^{-1} mg_{cat}^{-1} and a Faradaic efficiency of 10.5% based on NH_3 synthesis. As a comparison, Bi possessed a lower yield rate of 7.4 mg h^{-1} mg_{cat}^{-1} at -0.60 V with a Faradaic efficiency of 9.1%. The Faradaic efficiency of BiNi was further decreased to 4.2% at -0.70 V, mainly caused by the competition from the faster HER kinetics on Ni at more negative voltages.

5.4.3 Bi-Ni Cyano Coordinated Polymers-derived 3D amorphous BiNi alloy

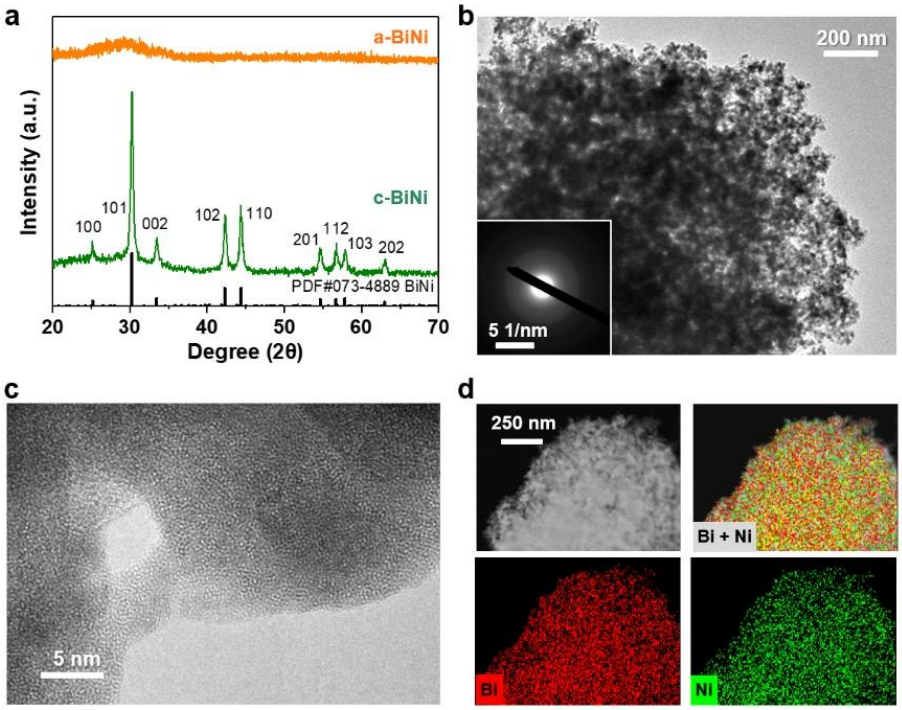

Figure 5.16: (a) XRD of a-BiNi and c-BiNi. (b) TEM, ED, (c) HRTEM, and (d) elemental mapping of a-BiNi.

To further facilitate the kinetics of NRR electrocatalysis on alloy electrocatalysts, amorphization engineering is applied in BiNi. Amorphous BiNi (a-BiNi) alloys are synthesized through NaBH4- induced amorphization by reacting Bi-Ni-CCP with NaBH4 in diethylene glycol (DEG) at room temperature. The amorphous alloys can be transformed to crystalline alloys (c-BiNi) electrocatalyst via thermal annealing in an inert atmosphere, while maintaining the chemical composition. Figure 5.16a displays the X-ray diffraction (XRD) pattern of a typical as-prepared BiNi alloy catalyst with a Bi/Ni molar ratio of 1:1. Different from c-BiNi, a-BiNi shows solely one broad diffraction peak centered at around 30 °, suggesting the increased disordered structure in the amorphous phase.

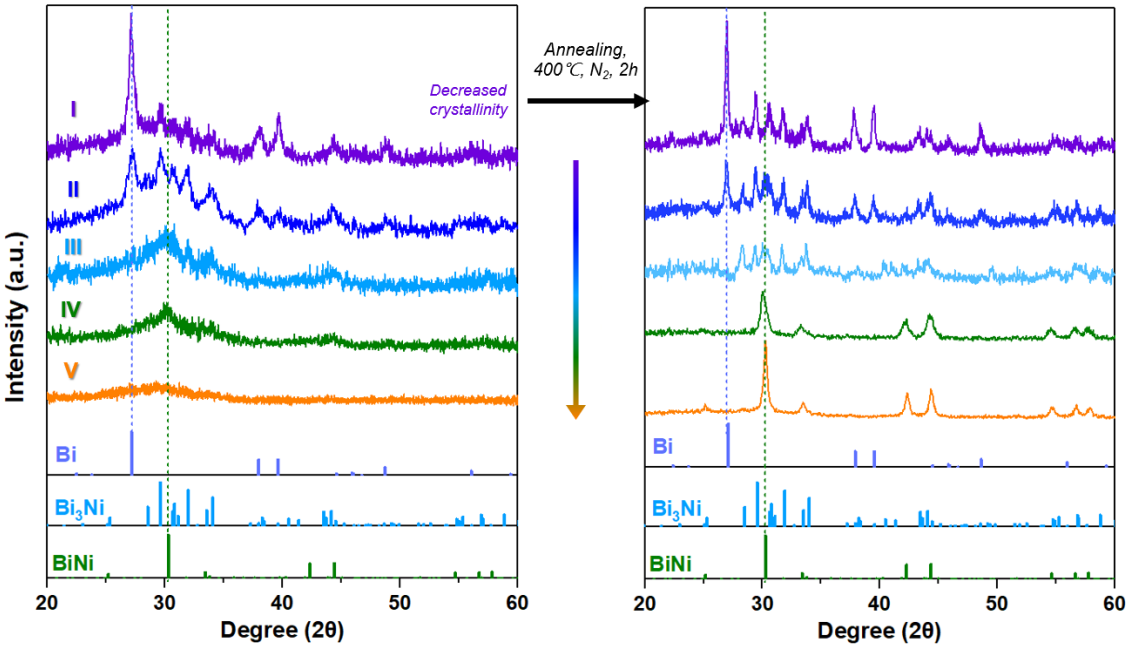

Figure 5.17: Composition and crystallinity evolution of the reduction of Bi-Ni-CCP to BiNi via $NaBH_4$ in DEG. The amorphous phase can be indirectly characterized by annealing the samples under 400°C, Bi cannot form an amorphous phase by $NaBH_4$ reduction of Bi precursor, according to the experimental results in Figure 5.6.

Interestingly, I found both compositions and crystallinity evolved as the reduction reaction continued. At the first 30 min of the reaction (step I), the products are mostly crystalline Bi and crystalline Bi_3Ni, while most $Ni^{(II)}$ has not been reduced (still solvated in DEG. Step II at around ~2 hours will yield more crystalline Bi_3Ni and become the dominant phase in the solid phase. After a 1-day reaction (step III), most $Ni^{(II)}$ has been reduced and elemental Bi disappears, and alloys with Ni to form low-crystalline Bi_3Ni and low-crystalline BiNi. After around 3 days, the dominant phase is low-crystalline BiNi, and finally amorphous BiNi (corresponding to 4-7 days).

In this system, BH_4^- is the reduction agent and meanwhile induces amorphization. DEG acts as surfactants and meanwhile maintains a reductive atmosphere. The following is the potential of half-reactions in the system.

(1) $BH_4^- + 8OH^- - 8\ e^- \rightarrow BO_2^- + 6H_2O$ (E= −1.24V)

(2) $Bi^{3+} + 3\,e^- \rightarrow Bi(s)$ (fast) (E = +0.31V)

(3) $-[Ni\text{-}CN]- + e^- \rightarrow Ni(s) + CN^-$ (slow) (E = −0.91V)

Bi^{3+} will be reduced to Bi^0 at first and form the crystalline core, while the formation of Ni^0 is slow. According to the recent literature and our control experiments, Only Ni can form an amorphous phase by the $NaBH_4$ reduction of Ni precursor, while Bi cannot form an amorphous phase.[124] The mechanism of BH_4^--induced amorphization of BiNi is proposed below:

$2BH_4^- + 2H_2O \rightleftharpoons 2B + 5H_2 + 2OH^-$ (slow)

$Ni + B \rightleftharpoons Ni\text{-}B$ (amorphous)

$Bi + Ni\text{-}B \rightleftharpoons Bi\text{-}Ni\text{-}B$ (amorphous)

$4Bi\text{-}Ni\text{-}B + 3O_2 + 4OH^- \rightarrow 4Bi\text{-}Ni$ (amorphous) $+ 4BO_2^- + 2H_2O$

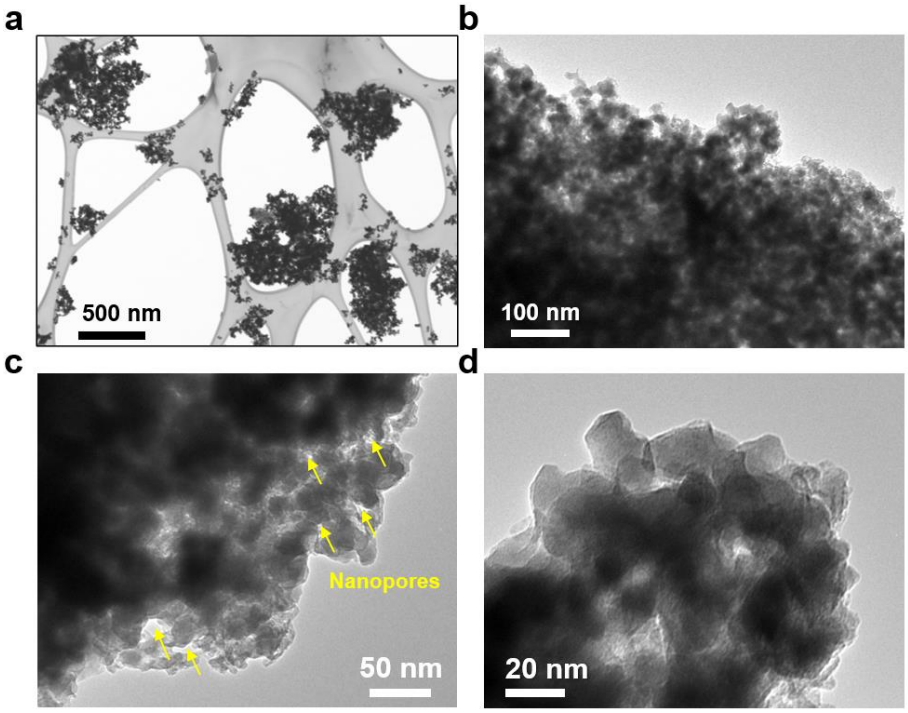

Figure 5.18: TEM images of 3D a-BiNi on C grid: The 3D porous framework is composed of small nanosheets (around 20 nm diameter). Annealing the amorphous BiNi alloy catalyst at 400 °C in Ar transformed the amorphous phase into a phase-pure crystal, and the particle size can be maintained after heat treatment.

The morphology was characterized by microscopy including TEM and SEM. As shown in Figure 5.16b and c, the as-synthesized a-BiNi catalyst exhibits similar 3D architectures with crystalline BiNi and crystalline Bi (c-Bi), composed of 3D interconnected nanoparticles and nanopores. The amorphous characteristics of the alloy catalyst can also be detected by selected-area electron diffraction (SAED). The diffusive rings in the inset of Figure 5.16b indicate the disordered atomic arrangement in alloys. Furthermore, high-resolution transmission electron microscopy (HRTEM, Figure 5.16c) confirmed the disordered structures of the BiNi alloy catalyst at an atomic level. Energy-dispersive X-ray spectroscopy (EDX, Figure 5.16d) mapping test was applied to check the

elemental distribution of Bi and Ni, where Bi and Ni elements are uniformly distributed across the entire 3D structures. The Bi/Ni atomic ratio was characterized to be 0.49:0.51, which is consistent with the binary phase diagram of BiNi.

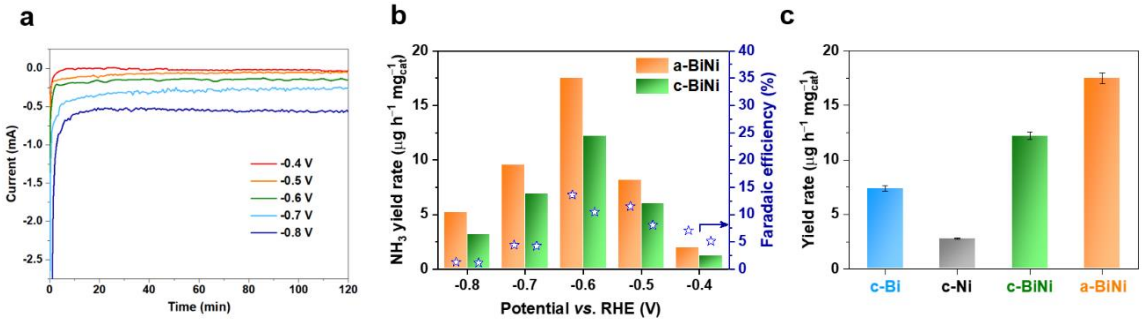

Figure 5.19: (a) CA curves under different voltages from -0.4V to -0.8V of a-BiNi alloys. (b) The yield rate of NH_3 production and Faradic efficiency from -0.4 V to -0.8 V of a-BiNi alloys and c-BiNi (crystalline alloys) alloys under N_2. (c) Comparison of the NH_3 yield rate at -0.6 V of c-Bi, c-Ni (crystalline Bi and Ni), a-BiNi, and c-BiNi alloys.

To investigate the role of amorphization engineering in BiNi alloy, we compared the NH_3 production of a-BiNi, c-BiNi, c-Bi, and c-Ni (Figure 5.19c). a-BiNi showed the NH_3 yield rate of 17.5 mg h^{-1} mg_{cat}^{-1} (1.43 times the yield rate of c-BiNi) and Faradaic efficiency of 13.8% at -0.60V (vs. RHE), suggesting improved electrocatalytic activity in amorphous alloy catalysts.

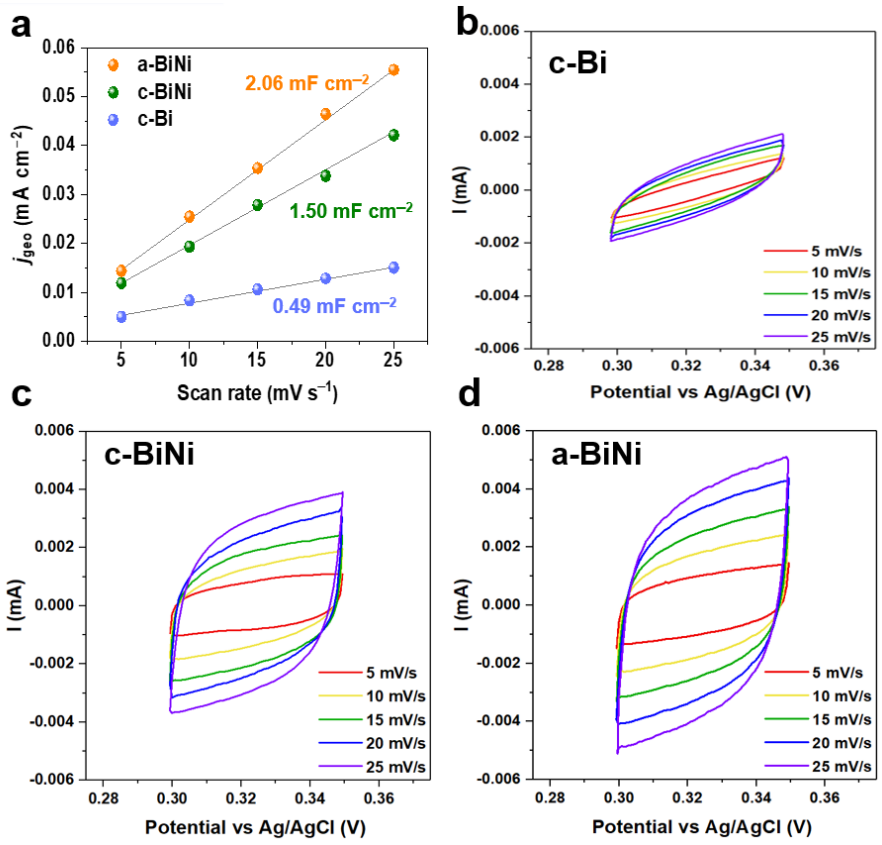

Figure 5.20: ECSAs of Bi-based NRR electrocatalysts: improved ECSA in amorphous BiNi compared with c-Bi and c-BiNi, due to enhanced electron transfer and amorphous feature.

To probe the synergistic effect of alloying effect and amorphization engineering in a-BiNi for electrocatalysis, the electrochemically active surface areas of the various catalysts were measured by testing the electrical double-layer capacitance of various electrocatalysts, and charging current density (based on geometry area, j_{geo}) differences were then plotted against scan rates (Figure 5.14). The ECSA of a-BiNi is almost 1.5 times of that the crystalline-BiNi alloy and 4.2 times of that the crystalline-Bi metal, as shown in Figure 5.14a. The enlarged electrochemical surface areas of amorphous BiNi alloy can be

ascribed to the synergistic effect between enhanced electron transfer favoring accessibility of active sites and increased exposed sites promoting the mass and electron transport.

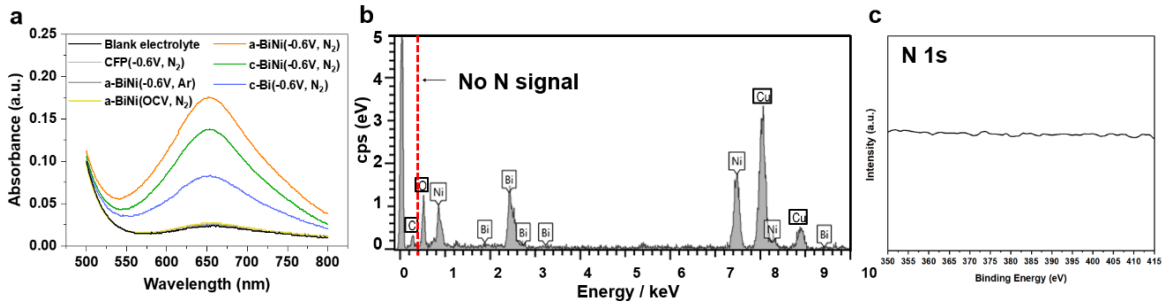

Figure 5.21: Exclusion of N contamination in amorphous BiNi alloy: No N-species were found before electrochemical tests: (a) UV-vis absorption spectra of electrolyte under different testing conditions. No N signals are detected from (b) EDS and (c) XPS spectra in a-BiNi.

To verify that NH_3 production was generated via the nitrogen reduction process catalyzed by a-BiNi electrocatalysts, a series of control experiments were conducted. As shown in Figure 5.21a, the control experiment in Ar was to analyze the possible contaminants from impurities (such as NO_3^-) from the electrolyte or electrocatalysts. When the reaction conducted in an Ar-saturated electrolyte at -0.60 V (vs. RHE) for 2 hours, the UV-Vis intensity of the control experiment in Ar is 0.0250 @ 655 nm, which can be converted to the yield rate of less than 0.12 mg h^{-1} mg_{cat}^{-1} (based on the calibration curve), indicating the absence of NH_3 left or generated from other N-containing residues in the catalyst. By subtracting the NH_3 measured from the control experiment in the Ar atmosphere, the yield rate and the Faradaic efficiency of a-BiNi at -0.60 V (vs. RHE) are calculated to be 17.38 mg h^{-1} mg_{cat}^{-1} and 13.70%. The UV-Vis data is consistent with the data obtained from EDS and XPS (Figure 5.21b and c), displaying no detectable N element in a-BiNi electrocatalyst. When a-BiNi was applied in N_2-saturated 0.1M Na_2SO_4 at an

open-circuit voltage (OCV), the yield rate of NH_3 production for BiNi was below the detection limit, implying the absence of NH_3 impurity from N_2 gas (99.999% ultra-high purity), CFP electrode, or atmosphere.

	Mass yield rate	Areal yield rate	FE	electrolyte	Ref.
	ug h^{-1} mg^{-1}	ug h^{-1} cm^{-2}			
3D amorphous BiNi	**17.50**	**8.75**	**13.80%**	**0.1 M Na_2SO_4**	**This Work**
Defect-rich Bi	5.43	2.40	11.68%	0.2 M Na_2SO_4	[130]
Bi nanosheets	6.50	3.25	12.11%	0.1 M Na_2SO_4	[127]
Mosaic Bi nanosheets	13.23	2.54	10.46%	0.1 M Na_2SO_4	[131]
Bi nanosheets	12.49	8.99	7.09%	0.1 M $NaHCO_3$	[132]
S-doped Bi nanobelts	10.28	5.14	10.48%	0.1 M Na_2SO_4	[133]
Bi@porous C	28.63	14.30	10.58%	0.1 M Na_2SO_4	[134]
Bi-CeO_2 Nanorods	--	6.29	8.56%	0.5 M Na_2SO_4	[27]
Porous Bi_5O_7I nanotubes@C	8.55	0.64	13.42%	0.1 M Na_2SO_4	[135]
Amorphous $Bi_4V_2O_{11}$-CeO_2	23.21	--	10.16	0.1 M HCl	[118]
Bi_2O_3/graphene	6.50	4.21	11.20%	0.1 M Na_2SO_4	[136]

Table 5.2: Comparison table of a-BiNi with recently reported Bi-based NRR electrocatalyst.

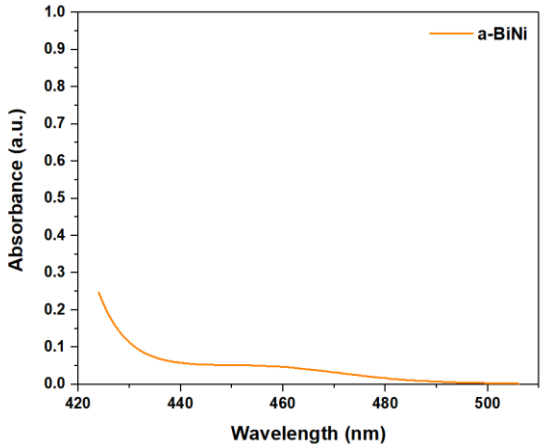

Figure 5.22: UV-vis spectrum from 420 to 510 nm of electrolytes after 2-hour-NRR of a-BiNi.

The amount of the possible by-product, hydrazine (N_2H_4), in the post-NRR electrolyte was analyzed by UV-Vis absorption spectra, to evaluate the selectivity of a-BiNi NRR electrocatalysts. As shown in Figure 5.16, The production of N_2H_4 was below the detection limit, which implying very low N_2H_4 concentration and high selectivity of NH_3 production over amorphous BiNi electrocatalyst. The long-term cycling test was further performed to investigate the stability property of the BiNi electrocatalyst. The alternating cycling test of electrocatalytic nitrogen fixation was performed @ -0.6 V (vs. RHE) between N_2 and Ar-saturated 0.1M Na_2SO_4 (Figure 5.23a). The yield rate of amorphous alloy catalysts can maintain 17.0 mg h^{-1} mg_{cat}^{-1} and faradaic efficiency is around 13.5% in each cycle in N_2-saturated electrolyte, while an extremely low yield rate is observed in Ar-saturated electrolyte, implying the catalytic activity and good cycling stability towards long-term nitrogen reduction. Additionally, after each 2-hour-NRR test at -0.60 V, no obvious degradation of total current was observed (Figure 5.23b), and the total

current of 3D amorphous BiNi electrocatalysts can be retained over 81% after 100 hours, suggesting the good electrochemical stability of NRR catalysts.

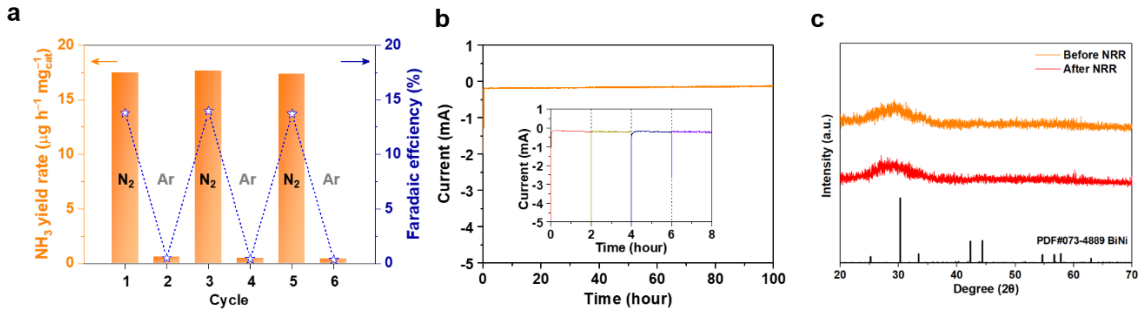

Figure 5.23: (a) Alternating cycling test of a-BiNi @−0.6 V (vs. RHE) between N_2 and Ar-saturated 0.1 M Na_2SO_4. (b) Long-term stability test of a-BiNi. (c) Post-XRD analysis of a-BiNi.

The chemical composition stability of BiNi electrocatalyst was investigated by XRD after a 2-hour nitrogen reduction reaction. From the ex-situ XRD characterization of the BiNi electrocatalyst in Figure 5.23c, no new phase was observed, demonstrating the high electrochemical stability of amorphous alloy catalysts. Besides, the 3D interconnected structure of a-BiNi can also be maintained after the NRR cycling test from the post-catalysis SEM.

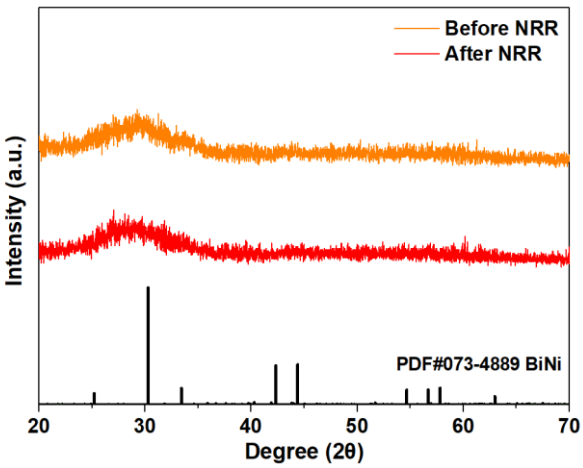

Figure 5.24: XRD of a-BiNi before and after NRR. No detectable difference between the fresh a-BiNi and post-NRR samples indicates no new phase or crystalline BiNi were formed.

5.5 CONCLUSIONS

To summarize, an amorphous BiNi alloy with an interconnected porous framework derived from 3D gels was developed for the enhanced electrocatalytic N_2 fixation process. Owing to the chemisorption of nitrogen and the lower ΔG_{*NNH} on the surface of BiNi, and the amorphous feature of 3D interconnected framework, amorphous Bi-Ni alloy electrocatalyst exhibits desirable catalytic activity for NH_3 production with a high yield rate of 17.5 mg h^{-1} mg_{cat}^{-1} and Faradaic efficiency of 13.8%, showing potential applications for practical nitrogen fixation.

Based on the above investigation including DFT simulations and experimental measurements (XPS, EDLC, EIS, and other electrochemical measurements), the enhanced NRR activity of a-BiNi can be attributed to the co-effects of optimized nitrogen adsorption and activation, disordered structure in amorphous phase for enlarged active surface area, and 3D conductive pathway with enhanced electron and ion transfer: (1) Ni substitution of

Bi can modulate the electronic configuration of pristine metals, allowing the alloy catalyst delivers optimized N adsorption energy of N_2 and intermediates; (2) the amorphization engineered phase possessing disordered atom arrangement and the defect-rich surface can provide high surface areas with abundant active sites to absorb/desorb N_2 and intermediates, and (3) the enhanced electron transfer due to Ni substitution and 3D bimetallic scaffold. The 3D hierarchical porous alloy pathways, not only serve as a high conductive network to facilitate electronic transport, but also offer a faster transport channel for both gas and electrolyte diffusion, favorable for increased ECSA and the contact between the electrocatalysts and electrolyte.[137] Moreover, the 3D interconnected porous scaffold with high structural stability against structure collapse alleviates the typical problem of particle aggregation upon cycling, allowing efficient and durable electrocatalytic activity of amorphous alloy NRR catalysts for potential practical applications. The enhanced electrochemical activity can be ascribed to the enhanced electron transport and increased active surface area of the 3D nanoporous alloy framework. Moreover, the 3D interconnected porous framework possesses high structural durability for long-term nitrogen fixation cycling.

Studies in Chapter 5 provide insights into optimizing the adsorption energy of reactants and intermediates combined with tuning the crystallinity of electrocatalysts in the nitrogen fixation field. Our proposed earth-abundant amorphous alloys demonstrate an alternative insight into developing effective and durable nitrogen fixation catalysts for potential practical applications. The gel derivatives incorporating the advantageous characteristics of highly porous structure with large surface area, uniformly distributed active species, efficient mass/charge transport, rationally controlled dopants, etc., become promising electrocatalysts for HER, OER, ORR, carbon dioxide reduction reaction (CO_2RR)[138], nitrate reduction reaction (NitRR)[139, 140] and more.

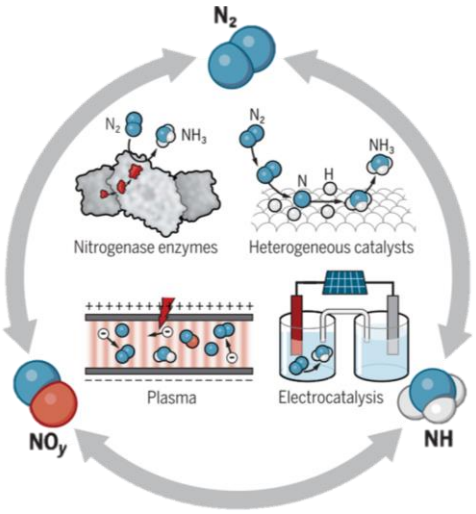

Figure 5.25: Nitrogen cycle via biological and artificial methods.

Looking forward, although increasing attention has been paid to the aqueous-based electrosynthesis of ammonia from N_2 under ambient conditions, this process still suffers from the low yield rate (<10 mmol g_{cat}^{-1} h^{-1}) and low Faradaic efficiency (<66%) due to the difficulties in breaking the triple bond of N_2 with high bonding energy and the suppression of the HER.[141-143]

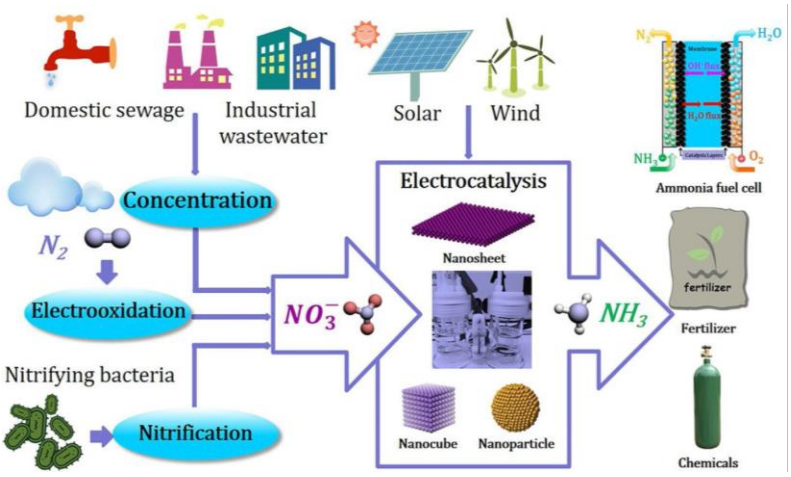

Figure 5.26: Nitrate reduction reaction process contributing to the future sustainability of fertilizer and renewable fuels recycling.

Another oxidized form of nitrogen, nitrate (NO_3^-), ubiquitously exists in the environment as the result of anthropogenic forcing on soil and water pollution through crop fertilization.[139, 140] Thanks to the relatively higher yield rate (>10 mmol $gcat^{-1}$ h^{-1}) and Faradaic efficiency (>80%), NitRR is a potential direction to effectively solve water pollution and meanwhile efficiently produce NH_3. Thus, developing precious-metal-free electrocatalysts for the advanced efficient electrochemical NH_3 synthesis with improved activity is highly expected.

Chapter 6: Summary

6.1 DISSERTATION SUMMARY

This dissertation focused on the structural engineering and electronic tuning of inorganic nanomaterials for electrocatalysis. My doctoral research is driven by the urgent need to break through the bottleneck of the current non-noble-metal electrocatalysts, suffering from low mass/charge transport. By combining the structural design and electronic modification of transition-metal-based electrocatalysts, the mass transfer and charge transport of the electrochemical process can be significantly improved, achieving advanced electrocatalysis with improved intrinsic catalytic activities and increased active surface areas.

The irreversible aggregation of nanomaterials during the electrode fabrication leads to the decrease of active surfaces and sluggish mass transfer for molecule adsorption. To address this issue, porosity engineering is applied in 2D mixed transition metal-based oxides, selenides, and phosphides. Pore/holey engineering offers larger active surface areas and abundant active sites for the adsorption of molecules, to alleviate the restacking issue of the isolated 2D nanomaterials and further facilitate the ion transfer. To extend porous/holey features to a wide range of electrocatalysts, gels and their derivatives are applied as promising electrocatalysts possessing enhanced mass/charge transfer. Compared with conventional electrocatalysts prepared from bulky powders suffering from severe problems on electrolyte penetration and electron transports, gel-based electrocatalysts, due to their unique hierarchical structures, ease of functionalization, and high wettability for ion transfer, serve as an ideal platform to study the fundamental electrocatalytic mechanism and facilitate the electrochemical reaction kinetics. For another, to improve increase the number of active sites on the catalyst surface, amorphization engineering is applied in gel-

derived BiNi alloy, to create different atomic arrangements and introduce defective sites and under-coordinated dangling bonds for N adsorption. With the assistance of newly developed advanced characterization techniques, we can clarify the relationships of active surface areas, and electrocatalytic efficiency and stability.

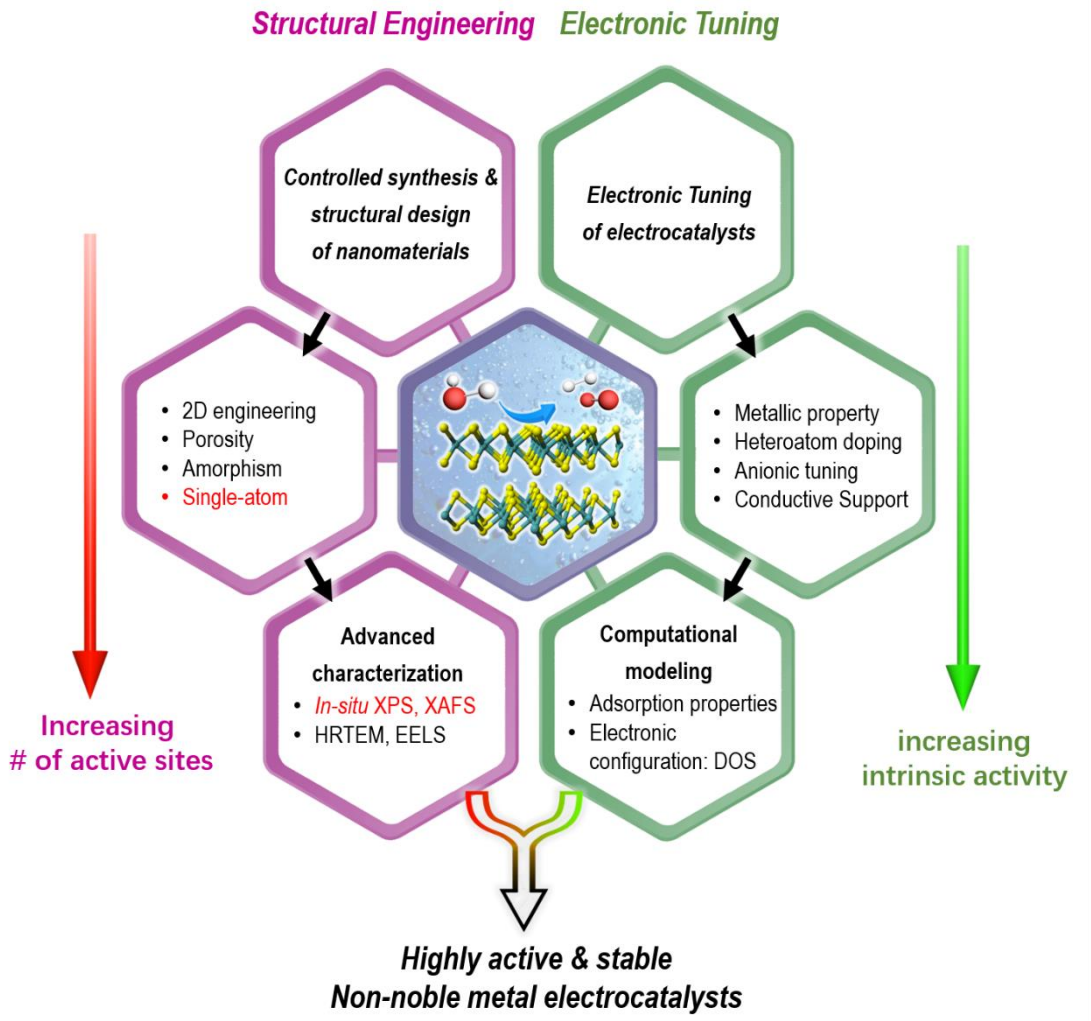

Figure 6.1: Conclusion and perspectives of structural engineering and electronic tuning of non-noble-metal-based electrocatalysts.

For another, many electrocatalysts are semiconductors or insulators, giving rise to inferior electron transfer during the electrochemical process. Through the modification of the electronic configuration of electrocatalysts, including anion substitution of oxides for metallic characteristics, hybrid with conductive additives for enhanced electron transfer,[137] and alloying with transition metals for enhanced electron transfer and N adsorption energy regulation, the electron transfer is boosted in 2D nanomaterials, cyanogel electrocatalysts, and gel-derived alloys. The density of state, energy band and the local electronic/atomic structure optimizations of electrocatalysts can be demonstrated by modeling computation. More importantly, electronic tuning strategies, such as anionic substitution and alloying, not only can boost the electron transfer by increasing electrical conductivity but also tailoring the surface properties for optimized free energy change of the absorption/desorption. To deeply understand the reaction pathway and mechanism of these multi-electron transfer, DFT modeling is employed to calculate the Gibbs free energy change of the absorption/desorption process of the intermediates, to disclose real active sites and intrinsic activities, shedding light on the reaction kinetics at the electronic and atomic levels.

The pursuit of green and large-scale energy conversion technologies has driven researchers to explore novel and potentially more efficient and stable electrocatalysts. By employing the structural design and electronic tuning of non-noble-metal electrocatalysts, active and stable electrocatalysts, with high active-site accessibility, rapid mass transport channel, desirable electrical conductivity, and optimized adsorption energy can be obtained. The strategies delivered in this dissertation would be of great value to guide the structural engineering and rational electronic tunning of advanced electrocatalysts with outstanding activity, selectivity, and durability, to meet the requirement of practical applications.

6.2 FUTURE DIRECTIONS

To fully exploit the strategies delivered in this dissertation for advanced electrocatalysis, the research of electrocatalysis should go both down to atomic/electronic level for fundamental studies and up to macroscopic assemblies for practical applications.

Large-scaled controlled synthesis of novel nanomaterials. Because of the 3D isotropic structure of gel materials, it is hard to control the 1D/2D structure in the cyanogel system. By functionalizing the monomers of cyanogels or applying appropriate shape-controlled templates, it is possible to realize 1D morphology by extending in a straight line along one axis or 2D planar morphology by extending in a straight line along two axes.

Advanced electrocatalyst and mechanism study. Hybrid electrocatalysts, especially heterojunction catalysts, play a critical role in efficient and stable catalyst design. The electronic interaction and electron transfer at the interface can be widely tuned by phase and strain, providing more opportunities to investigate the interfacial interaction and designing highly efficient electrocatalysts. Moreover, single-atom catalysts (SACs) with the ultimate fine distribution of metal active sites have been emerged as one of the most promising topics because of unique catalytic features and high atom utilization. Recently, single transition metal atoms bonded to N-doped carbon matrix are attracting much attention in the community of SACs. It has been noticed that the strong substrate effect on isolated metal atoms (M-N-C, M= Fe, Co, Mn, Cu, *etc.*) not only optimizes the electronic structure of the metal sites but also confines and stabilizes the single atoms. Cyanogels and conductive polymers, containing abundant heteroatom with high composition tunability, are ideal precursors of the single-atom catalysts. Due to relatively well-defined active sites, SAC is a good material platform to probe reaction mechanisms and fundamental physicochemical processes.[144, 145]

Electrocatalysis for renewable conversion with novel reactors. In my future research, I will continue pushing the core of low-dimensional materials energy conversion devices. In addition to electrocatalytic water splitting and nitrogen reduction, more attention will be paid to the fundamental study of nitrate reduction and carbon dioxide reduction electrocatalysis. As discussed in Chapter 5, electrocatalytic nitrogen reduction reaction (NitRR) under ambient conditions is a more energy-efficient and green technology for the conversion of NO_x into NH_3, compared with electrocatalytic N_2 fixation. To bridge the gap between lab-scale electrocatalysis and large-scale application, novel electrocatalysis reactors are highly required. For example, with the help of gas diffusion layer (GDL) electrodes (containing porous materials composed of a dense array of carbon fibers), the electrically conductive pathway for current collection can be enhanced. GDL plays an important role in the electronic connection between the bipolar plate with channel-land structure and the electrode.[146] By applying solid-state electrolytes, the contamination of the product solution by extraneous ions can be avoided, removing the need for costly separation processes for more practical applications.

References

1. Seh, Z. W.; Kibsgaard, J.; Dickens, C. F.; Chorkendorff, I.; Nørskov, J. K.; Jaramillo, T. F., *Science* **2017,** *355*, eaad4998.
2. Turner, J. A., *Science* **2004,** *305*, 972-974.
3. Pomerantseva, E.; Bonaccorso, F.; Feng, X.; Cui, Y.; Gogotsi, Y., *Science* **2019,** *366*, eaan8285.
4. Yang, M.-Q.; Wang, J.; Wu, H.; Ho, G. W., *Small* **2018,** *14*, 1703323.
5. Bak, J.; Heo, Y.; Yun, T. G.; Chung, S.-Y., *ACS Nano* **2020,** *14*, 14323-14354.
6. Suryanto, B. H. R.; Du, H.-L.; Wang, D.; Chen, J.; Simonov, A. N.; MacFarlane, D. R., *Nat. Catal.* **2019,** *2*, 290-296.
7. Luo, J.; Im, J.-H.; Mayer, M. T.; Schreier, M.; Nazeeruddin, M. K.; Park, N.-G.; Tilley, S. D.; Fan, H. J.; Grätzel, M., *Science* **2014,** *345*, 1593-1596.
8. Zhang, Y.; Pang, S.; Wei, Z.; Jiao, H.; Dai, X.; Wang, H.; Shi, F., *Nat. Commun.* **2018,** *9*, 1465.
9. Guo, C.; Ran, J.; Vasileff, A.; Qiao, S.-Z., *Energy Environ. Sci.* **2018,** *11*, 45-56.
10. Anantharaj, S.; Ede, S. R.; Sakthikumar, K.; Karthick, K.; Mishra, S.; Kundu, S., **2016**.
11. Cheng, F.; Chen, J., *Chem. Soc. Rev.* **2012,** *41*, 2172-2192.
12. Lu, Q.; Yu, Y.; Ma, Q.; Chen, B.; Zhang, H., *Adv. Mater.* **2016,** *28*, 1917-1933.
13. Zhou, L.; Zhuang, Z.; Zhao, H.; Lin, M.; Zhao, D.; Mai, L., *Adv. Mater.* **2017,** *29*, 1602914.
14. Han, N.; Wang, Y.; Yang, H.; Deng, J.; Wu, J.; Li, Y.; Li, Y., *Nat. Commun.* **2018,** *9*, 1320.
15. Geng, X.; Sun, W.; Wu, W.; Chen, B.; Al-Hilo, A.; Benamara, M.; Zhu, H.; Watanabe, F.; Cui, J.; Chen, T.-p., *Nat. Commun.* **2016,** *7*, ncomms10672.
16. Wang, D.-Y.; Gong, M.; Chou, H.-L.; Pan, C.-J.; Chen, H.-A.; Wu, Y.; Lin, M.-C.; Guan, M.; Yang, J.; Chen, C.-W., *J. Am. Chem. Soc.* **2015,** *137*, 1587-1592.
17. Han, J.; Ji, X.; Ren, X.; Cui, G.; Li, L.; Xie, F.; Wang, H.; Li, B.; Sun, X., *J. Mater. Chem. A* **2018,** *6*, 12974-12977.
18. Zhang, L.; Ding, L. X.; Chen, G. F.; Yang, X.; Wang, H., *Angew. Chem.* **2019,** *131*, 2638-2642.
19. Liu, W.-J.; Hu, X.; Li, H.-C.; Yu, H.-Q., *Small* **2018,** *14*, 1801878.
20. Zhang, J.; Zhao, L.; Liu, A.; Li, X.; Wu, H.; Lu, C., *Electrochim. Acta* **2015,** *182*, 652-658.
21. Luo, Y.; Chen, G.-F.; Ding, L.; Chen, X.; Ding, L.-X.; Wang, H., *Joule* **2019,** *3*, 279-289.
22. Xu, Y.; Lin, Z.; Zhong, X.; Huang, X.; Weiss, N. O.; Huang, Y.; Duan, X., *Nat. Commun.* **2014,** *5*, 4554.
23. Zhu, Y.; Peng, L.; Fang, Z.; Yan, C.; Zhang, X.; Yu, G., *Adv. Mater.* **2018,** *30*, 1706347.

24. Schoenbaum, C. A.; Schwartz, D. K.; Medlin, J. W., *Acc. Chem. Res.* **2014,** *47*, 1438-1445.
25. Prieto, G.; Tüysüz, H.; Duyckaerts, N.; Knossalla, J.; Wang, G.-H.; Schüth, F., *Chem. Rev.* **2016,** *116*, 14056-14119.
26. Tian, J.; Liu, Q.; Asiri, A. M.; Sun, X., *J. Am. Chem. Soc.* **2014,** *136*, 7587-7590.
27. Liu, Y.; Li, C.; Guan, L.; Li, K.; Lin, Y., *J. Phys. Chem. C* **2020,** *124*, 18003-18009.
28. Chen, P.; Xu, K.; Fang, Z.; Tong, Y.; Wu, J.; Lu, X.; Peng, X.; Ding, H.; Wu, C.; Xie, Y., *Angew. Chem.* **2015,** *127*, 14923-14927.
29. Lambert, T. N.; Vigil, J. A.; White, S. E.; Davis, D. J.; Limmer, S. J.; Burton, P. D.; Coker, E. N.; Beechem, T. E.; Brumbach, M. T., *Chem. Commun.* **2015,** *51*, 9511-9514.
30. Liu, Y.; Cheng, H.; Lyu, M.; Fan, S.; Liu, Q.; Zhang, W.; Zhi, Y.; Wang, C.; Xiao, C.; Wei, S.; Ye, B.; Xie, Y., *J. Am. Chem. Soc.* **2014,** *136*, 15670-15675.
31. Xu, K.; Chen, P.; Li, X.; Tong, Y.; Ding, H.; Wu, X.; Chu, W.; Peng, Z.; Wu, C.; Xie, Y., *J. Am. Chem. Soc.* **2015,** *137*, 4119-4125.
32. Liang, H.; Gandi, A. N.; Anjum, D. H.; Wang, X.; Schwingenschlögl, U.; Alshareef, H. N., *Nano Lett.* **2016,** *16*, 7718-7725.
33. Zou, X.; Zhang, Y., *Chem. Soc. Rev.* **2015,** *44*, 5148-5180.
34. Li, J.; Yan, M.; Zhou, X.; Huang, Z.-Q.; Xia, Z.; Chang, C.-R.; Ma, Y.; Qu, Y., *Adv. Funct. Mater.* **2016,** *26*, 6785-6796.
35. Liu, L.; Jiang, Z.; Fang, L.; Xu, H.; Zhang, H.; Gu, X.; Wang, Y., *ACS Appl. Mater. Interfaces* **2017,** *9*, 27736-27744.
36. Zhuang, M.; Ou, X.; Dou, Y.; Zhang, L.; Zhang, Q.; Wu, R.; Ding, Y.; Shao, M.; Luo, Z., *Nano Lett.* **2016,** *16*, 4691-4698.
37. Jiao, L.; Zhou, Y.-X.; Jiang, H.-L., *Chemical science* **2016,** *7*, 1690-1695.
38. Wang, J.; Yang, W.; Liu, J., *J. Mater. Chem. A* **2016,** *4*, 4686-4690.
39. Huang, Z.; Chen, Z.; Chen, Z.; Lv, C.; Humphrey, M. G.; Zhang, C., *Nano Energy* **2014,** *9*, 373-382.
40. Chen, P.; Xu, K.; Tao, S.; Zhou, T.; Tong, Y.; Ding, H.; Zhang, L.; Chu, W.; Wu, C.; Xie, Y., *Adv. Mater.* **2016,** *28*, 7527-7532.
41. Liang, H.-W.; Brüller, S.; Dong, R.; Zhang, J.; Feng, X.; Müllen, K., *Nat. Commun.* **2015,** *6*, 1-8.
42. Du, C.; Yang, L.; Yang, F.; Cheng, G.; Luo, W., *ACS Catal.* **2017,** *7*, 4131-4137.
43. Feng, Y.; Yu, X.-Y.; Paik, U., *Chem. Commun.* **2016,** *52*, 1633-1636.
44. Yu, J.; Li, Q.; Li, Y.; Xu, C. Y.; Zhen, L.; Dravid, V. P.; Wu, J., *Adv. Funct. Mater.* **2016,** *26*, 7644-7651.
45. Li, Y.; Liu, J.; Chen, C.; Zhang, X.; Chen, J., *ACS Appl. Mater. Interfaces* **2017,** *9*, 5982-5991.

46. Liang, H.; Gandi, A. N.; Anjum, D. H.; Wang, X.; Schwingenschlögl, U.; Alshareef, H. N., *Nano Lett.* **2016,** *16*, 7718-7725.
47. Li, J.; Yan, M.; Zhou, X.; Huang, Z. Q.; Xia, Z.; Chang, C. R.; Ma, Y.; Qu, Y., *Adv. Funct. Mater.* **2016,** *26*, 6785-6796.
48. You, B.; Jiang, N.; Sheng, M.; Bhushan, M. W.; Sun, Y., *ACS Catal.* **2016,** *6*, 714-721.
49. Laursen, A.; Patraju, K.; Whitaker, M.; Retuerto, M.; Sarkar, T.; Yao, N.; Ramanujachary, K.; Greenblatt, M.; Dismukes, G. C., *Energy Environ. Sci.* **2015,** *8*, 1027-1034.
50. Zhu, W.; Yue, X.; Zhang, W.; Yu, S.; Zhang, Y.; Wang, J.; Wang, J., *Chem. Commun.* **2016,** *52*, 1486-1489.
51. Tang, C.; Cheng, N.; Pu, Z.; Xing, W.; Sun, X., *Angew. Chem.* **2015,** *127*, 9483-9487.
52. Gu, S.; Du, H.; Asiri, A. M.; Sun, X.; Li, C. M., *PCCP* **2014,** *16*, 16909-16913.
53. Zhuang, M.; Ou, X.; Dou, Y.; Zhang, L.; Zhang, Q.; Wu, R.; Ding, Y.; Shao, M.; Luo, Z., *Nano Lett.* **2016,** *16*, 4691-4698.
54. Hao, J.; Yang, W.; Zhang, Z.; Tang, J., *Nanoscale* **2015,** *7*, 11055-11062.
55. Feng, L.-L.; Li, G.-D.; Liu, Y.; Wu, Y.; Chen, H.; Wang, Y.; Zou, Y.-C.; Wang, D.; Zou, X., *ACS Appl. Mater. Interfaces* **2015,** *7*, 980-988.
56. Zou, X.; Huang, X.; Goswami, A.; Silva, R.; Sathe, B. R.; Mikmeková, E.; Asefa, T., *Angew. Chem.* **2014,** *126*, 4461-4465.
57. Feng, L.-L.; Yu, G.; Wu, Y.; Li, G.-D.; Li, H.; Sun, Y.; Asefa, T.; Chen, W.; Zou, X., *J. Am. Chem. Soc.* **2015,** *137*, 14023-14026.
58. Liu, T.; Ma, X.; Liu, D.; Hao, S.; Du, G.; Ma, Y.; Asiri, A. M.; Sun, X.; Chen, L., *ACS Catal.* **2017,** *7*, 98-102.
59. Guan, B. Y.; Yu, L.; Lou, X. W. D., *Angew. Chem. Int. Ed.* **2017,** *56*, 2386-2389.
60. Li, W.; Gao, X.; Xiong, D.; Wei, F.; Song, W.-G.; Xu, J.; Liu, L., *Adv. Energy Mater.* **2017,** *7*, 1602579.
61. Tang, T.; Jiang, W.-J.; Niu, S.; Liu, N.; Luo, H.; Chen, Y.-Y.; Jin, S.-F.; Gao, F.; Wan, L.-J.; Hu, J.-S., *J. Am. Chem. Soc.* **2017,** *139*, 8320-8328.
62. Masa, J.; Weide, P.; Peeters, D.; Sinev, I.; Xia, W.; Sun, Z.; Somsen, C.; Muhler, M.; Schuhmann, W., *Adv. Energy Mater.* **2016,** *6*, 1502313.
63. Huang, S.; Meng, Y.; He, S.; Goswami, A.; Wu, Q.; Li, J.; Tong, S.; Asefa, T.; Wu, M., *Adv. Funct. Mater.* **2017,** *27*, 1606585.
64. Tang, C.; Zhang, R.; Lu, W.; He, L.; Jiang, X.; Asiri, A. M.; Sun, X., *Adv. Mater.* **2017,** *29*, 1602441.
65. Menezes, P. W.; Indra, A.; Das, C.; Walter, C.; Göbel, C.; Gutkin, V.; Schmeiβer, D.; Driess, M., *ACS Catal.* **2017,** *7*, 103-109.
66. Ledendecker, M.; Krick Calderón, S.; Papp, C.; Steinrück, H. P.; Antonietti, M.; Shalom, M., *Angew. Chem. Int. Ed.* **2015,** *54*, 12361-12365.
67. Wang, X.; Li, W.; Xiong, D.; Petrovykh, D. Y.; Liu, L., *Adv. Funct. Mater.* **2016,** *26*, 4067-4077.

68. Guo, Y.; Bae, J.; Zhao, F.; Yu, G., *Trends Chem.* **2019**.
69. Bhattacharya, S.; Samanta, S. K., *Chem. Rev.* **2016,** *116*, 11967-12028.
70. Kwon, I. C.; Bae, Y. H.; Kim, S. W., *Nature* **1991,** *354*, 291-293.
71. Vermonden, T.; Censi, R.; Hennink, W. E., *Chem. Rev.* **2012,** *112*, 2853-2888.
72. Zhou, X.; Guo, Y.; Zhao, F.; Yu, G., *Acc. Chem. Res.* **2019,** *52*, 3244-3253.
73. Li, P.; Jin, Z.; Qian, Y.; Fang, Z.; Xiao, D.; Yu, G., *ACS Energy Lett.* **2019,** *4*, 1793-1802.
74. Zhai, D.; Liu, B.; Shi, Y.; Pan, L.; Wang, Y.; Li, W.; Zhang, R.; Yu, G., *ACS Nano* **2013,** *7*, 3540-3546.
75. Shi, Y.; Zhang, J.; Pan, L.; Shi, Y.; Yu, G., *Nano Today* **2016,** *11*, 738-762.
76. Shi, Y.; Zhou, X.; Zhang, J.; Bruck, A. M.; Bond, A. C.; Marschilok, A. C.; Takeuchi, K. J.; Takeuchi, E. S.; Yu, G., *Nano Lett.* **2017,** *17*, 1906-1914.
77. Li, P.; Jin, Z.; Peng, L.; Zhao, F.; Xiao, D.; Jin, Y.; Yu, G., *Adv. Mater.* **2018,** *30*, 1800124.
78. Li, P.; Jin, Z.; Qian, Y.; Fang, Z.; Xiao, D.; Yu, G., *Mater. Today* **2020,** *35*, 78-86.
79. Fang, Z.; Li, P.; Yu, G., *Adv. Mater.* **2020,** *32*, 2003191.
80. Wan, W.; Zhang, R.; Ma, M.; Zhou, Y., *J. Mater. Chem. A* **2018,** *6*, 754-775.
81. Zhao, F.; Bae, J.; Zhou, X.; Guo, Y.; Yu, G., *Adv. Mater.* **2018,** *30*, 1801796.
82. Fang, Z.; Zhang, A.; Wu, P.; Yu, G., *ACS Mater. Lett.* **2019,** *1*, 158-170.
83. Alemán, J.; Chadwick, A. V.; He, J.; Hess, M.; Horie, K.; Jones, R. G.; Kratochvíl, P.; Meisel, I.; Mita, I.; Moad, G., *Pure Appl. Chem.* **2007,** *79*, 1801-1829.
84. Pan, L.; Yu, G.; Zhai, D.; Lee, H. R.; Zhao, W.; Liu, N.; Wang, H.; Tee, B. C. K.; Shi, Y.; Cui, Y.; Bao, Z., *Proc. Natl. Acad. Sci.* **2012,** *109*, 9287.
85. Zhang, B.; Zheng, X.; Voznyy, O.; Comin, R.; Bajdich, M.; García-Melchor, M.; Han, L.; Xu, J.; Liu, M.; Zheng, L.; García de Arquer, F. P.; Dinh, C. T.; Fan, F.; Yuan, M.; Yassitepe, E.; Chen, N.; Regier, T.; Liu, P.; Li, Y.; De Luna, P.; Janmohamed, A.; Xin, H. L.; Yang, H.; Vojvodic, A.; Sargent, E. H., *Science* **2016,** *352*, 333.
86. Zhang, W.; Xu, X.; Zhang, C.; Yu, Z.; Zhou, Y.; Tang, Y.; Wu, P.; Guo, S., *Small Methods* **2017,** *1*, 1700167.
87. Xu, Y.; Sheng, K.; Li, C.; Shi, G., *ACS Nano* **2010,** *4*, 4324-4330.
88. Chen, Z.; To, J. W. F.; Wang, C.; Lu, Z.; Liu, N.; Chortos, A.; Pan, L.; Wei, F.; Cui, Y.; Bao, Z., *Adv. Energy Mater.* **2014,** *4*, 1400207.
89. Yin, Z.; Zheng, Q., *Adv. Energy Mater.* **2012,** *2*, 179-218.
90. Danks, A. E.; Hall, S. R.; Schnepp, Z., *Materials Horizons* **2016,** *3*, 91-112.
91. Zhang, W.; Zhu, X.; Chen, X.; Zhou, Y.; Tang, Y.; Ding, L.; Wu, P., *Nanoscale* **2016,** *8*, 9828-9836.
92. Zhang, W.; Zhang, J.; Zhang, M.; Zhang, C.; Zhang, A.; Zhou, Y.; Tang, Y.; Wu, P., *New J. Chem.* **2015,** *39*, 8249-8253.
93. Wu, P.; Zhang, A.; Peng, L.; Zhao, F.; Tang, Y.; Zhou, Y.; Yu, G., *ACS Nano* **2018,** *12*, 759-767.
94. Zhao, F.; Shi, Y.; Pan, L.; Yu, G., *Acc. Chem. Res.* **2017,** *50*, 1734-1743.

95. Han, N.; Yang, K. R.; Lu, Z.; Li, Y.; Xu, W.; Gao, T.; Cai, Z.; Zhang, Y.; Batista, V. S.; Liu, W., *Nat. Commun.* **2018,** *9*, 1-10.
96. Reier, T.; Nong, H. N.; Teschner, D.; Schlögl, R.; Strasser, P., *Adv. Energy Mater.* **2017,** *7*, 1601275.
97. *ACS Energy Lett.* **2017,** *2*, 1937-1938.
98. Blasco-Ahicart, M.; Soriano-López, J.; Carbó, J. J.; Poblet, J. M.; Galan-Mascaros, J. R., *Nat. Chem.* **2018,** *10*, 24-30.
99. Pokhrel, R.; Goetz, M. K.; Shaner, S. E.; Wu, X.; Stahl, S. S., *J. Am. Chem. Soc.* **2015,** *137*, 8384-8387.
100. Zhang, W.; Lai, W.; Cao, R., *Chem. Rev.* **2017,** *117*, 3717-3797.
101. Han, L.; Tang, P.; Reyes-Carmona, Á.; Rodríguez-García, B.; Torréns, M.; Morante, J. R.; Arbiol, J.; Galan-Mascaros, J. R., *J. Am. Chem. Soc.* **2016,** *138*, 16037-16045.
102. Paolella, A.; Faure, C.; Timoshevskii, V.; Marras, S.; Bertoni, G.; Guerfi, A.; Vijh, A.; Armand, M.; Zaghib, K., *J. Mater. Chem. A* **2017,** *5*, 18919-18932.
103. Hurlbutt, K.; Wheeler, S.; Capone, I.; Pasta, M., *Joule* **2018,** *2*, 1950-1960.
104. Zhou, M.; Qian, J.; Ai, X.; Yang, H., *Adv. Mater.* **2011,** *23*, 4913-4917.
105. Gaikwad, N.; Bhanoth, S.; More, P. V.; Jain, G. H.; Khanna, P. K., *Nanoscale* **2014,** *6*, 2746-2751.
106. Zhao, F.; Zhou, X.; Shi, Y.; Qian, X.; Alexander, M.; Zhao, X.; Mendez, S.; Yang, R.; Qu, L.; Yu, G., *Nature Nanotechnology* **2018,** *13*, 489-495.
107. Hu, Q.; Li, G.; Liu, X.; Zhu, B.; Chai, X.; Zhang, Q.; Liu, J.; He, C., *Angew. Chem. Int. Ed.* **2019,** *58*, 4318-4322.
108. Shi, Y.; Pan, L.; Liu, B.; Wang, Y.; Cui, Y.; Bao, Z.; Yu, G., *J. Mater. Chem. A* **2014,** *2*, 6086-6091.
109. Guo, Y.; Bae, J.; Fang, Z.; Li, P.; Zhao, F.; Yu, G., *Chem. Rev.* **2020,** *120*, 7642-7707.
110. Zhang, A.; Fang, Z.; Tang, Y.; Zhou, Y.; Wu, P.; Yu, G., *Nano Lett.* **2019,** *19*, 6292-6298.
111. Luo, M.; Guo, S., *Nat. Rev. Mater.* **2017,** *2*, 17059.
112. Liu, Z.; Yang, X.; Cui, L.; Shi, Z.; Lu, B.; Guo, X.; Zhang, J.; Xu, L.; Tang, Y.; Xiang, Y., *Particle & Particle Systems Characterization* **2018,** *35*, 1700366.
113. Wu, P.; Fang, Z.; Zhang, A.; Zhang, X.; Tang, Y.; Zhou, Y.; Yu, G., *Research* **2019,** *2019*, 8393085.
114. Zheng, G.; Yan, J.-M.; Yu, G., *Small Methods* **2019,** *3*, 1900070.
115. Guo, W.; Zhang, K.; Liang, Z.; Zou, R.; Xu, Q., *Chem. Soc. Rev.* **2019,** *48*, 5658-5716.
116. Deng, J.; Iñiguez, J. A.; Liu, C., *Joule* **2018,** *2*, 846-856.
117. Lee, H. K.; Koh, C. S. L.; Lee, Y. H.; Liu, C.; Phang, I. Y.; Han, X.; Tsung, C.-K.; Ling, X. Y., *Sci. Adv.* **2018,** *4*, eaar3208.
118. Lv, C.; Yan, C.; Chen, G.; Ding, Y.; Sun, J.; Zhou, Y.; Yu, G., *Angew. Chem. Int. Ed.* **2018,** *57*, 6073-6076.

119. Li, S.-J.; Bao, D.; Shi, M.-M.; Wulan, B.-R.; Yan, J.-M.; Jiang, Q., *Adv. Mater.* **2017,** *29*, 1700001.
120. Zhang, C.; Xu, Y.; Lv, C.; Bai, L.; Liao, J.; Zhai, Y.; Zhang, H.; Chen, G., *Applied Catalysis B: Environmental* **2020,** *264*, 118416.
121. Li, H.; Wei, W.; Zhao, Y.; Li, H., Preparation and Catalytic Applications of Amorphous Alloys. In *Catalysis*, The Royal Society of Chemistry: 2015; Vol. 27, pp 144-186.
122. Shi, M.-M.; Bao, D.; Li, S.-J.; Wulan, B.-R.; Yan, J.-M.; Jiang, Q., *Adv. Energy Mater.* **2018,** *8*, 1800124.
123. Cai, W.; Chen, R.; Yang, H.; Tao, H. B.; Wang, H.-Y.; Gao, J.; Liu, W.; Liu, S.; Hung, S.-F.; Liu, B., *Nano Lett.* **2020,** *20*, 4278-4285.
124. Alexander, A.-M.; Hargreaves, J. S. J., *Chem. Soc. Rev.* **2010,** *39*, 4388-4401.
125. *Chem. Rev.* **2012,** *112*, 673-674.
126. Grape, E. S.; Flores, J. G.; Hidalgo, T.; Martínez-Ahumada, E.; Gutiérrez-Alejandre, A.; Hautier, A.; Williams, D. R.; O'Keeffe, M.; Öhrström, L.; Willhammar, T.; Horcajada, P.; Ibarra, I. A.; Inge, A. K., *J. Am. Chem. Soc.* **2020,** *142*, 16795-16804.
127. Yao, D.; Tang, C.; Li, L.; Xia, B.; Vasileff, A.; Jin, H.; Zhang, Y.; Qiao, S.-Z., *Adv. Energy Mater.* **2020,** *10*, 2001289.
128. Xue, Z.-H.; Zhang, S.-N.; Lin, Y.-X.; Su, H.; Zhai, G.-Y.; Han, J.-T.; Yu, Q.-Y.; Li, X.-H.; Antonietti, M.; Chen, J.-S., *J. Am. Chem. Soc.* **2019,** *141*, 14976-14980.
129. Wu, J.; Miao, Y.; Liang, X.; Yang, Z.; Yang, Y.; Ouyang, R., *Electroanalysis* **2014,** *26*, 856-863.
130. Wang, Y.; Shi, M.-m.; Bao, D.; Meng, F.-l.; Zhang, Q.; Zhou, Y.-t.; Liu, K.-h.; Zhang, Y.; Wang, J.-z.; Chen, Z.-w.; Liu, D.-p.; Jiang, Z.; Luo, M.; Gu, L.; Zhang, Q.-h.; Cao, X.-z.; Yao, Y.; Shao, M.-h.; Zhang, Y.; Zhang, X.-B.; Chen, J. G.; Yan, J.-m.; Jiang, Q., *Angew. Chem. Int. Ed.* **2019,** *58*, 9464-9469.
131. Li, L.; Tang, C.; Xia, B.; Jin, H.; Zheng, Y.; Qiao, S.-Z., *ACS Catal.* **2019,** *9*, 2902-2908.
132. Xia, L.; Fu, W.; Zhuang, P.; Cao, Y.; Chee, M. O. L.; Dong, P.; Ye, M.; Shen, J., *ACS Sustain. Chem. Eng.* **2020,** *8*, 2735-2741.
133. Lin, Y.; Yang, L.; Jiang, H.; Zhang, Y.; Bo, Y.; Liu, P.; Chen, S.; Xiang, B.; Li, G.; Jiang, J.; Xiong, Y.; Song, L., *J. Phys. Chem. Lett.* **2020,** *11*, 1746-1752.
134. Qiu, Y.; Zhao, S.; Qin, M.; Diao, J.; Liu, S.; Dai, L.; Zhang, W.; Guo, X., *Inorg. Chem. Front.* **2020,** *7*, 2006-2016.
135. Liu, Y.; Huang, B.; Chen, X.; Tian, Z.; Zhang, X.; Tsiakaras, P.; Shen, P. K., *Applied Catalysis B: Environmental* **2020,** *271*, 118919.
136. Sun, Y.; Deng, Z.; Song, X.-M.; Li, H.; Huang, Z.; Zhao, Q.; Feng, D.; Zhang, W.; Liu, Z.; Ma, T., *Nano-Micro Lett.* **2020,** *12*, 133.
137. Fang, Z.; Fernandez, D.; Wang, N.; Bai, Z.; Yu, G., *Sci. China Chem.* **2020**.

138. Birdja, Y. Y.; Pérez-Gallent, E.; Figueiredo, M. C.; Göttle, A. J.; Calle-Vallejo, F.; Koper, M. T. M., *Nat. Energy* **2019,** *4*, 732-745.
139. Zeng, Y.; Priest, C.; Wang, G.; Wu, G., *Small Methods* **2020,** *4*, 2000672.
140. Fu, X.; Zhao, X.; Hu, X.; He, K.; Yu, Y.; Li, T.; Tu, Q.; Qian, X.; Yue, Q.; Wasielewski, M. R.; Kang, Y., *Applied Materials Today* **2020,** *19*, 100620.
141. Li, P.; Jin, Z.; Fang, Z.; Yu, G., *Angew. Chem. Int. Ed.* **2020,** *59*, 22610-22616.
142. Lv, C.; Qian, Y.; Yan, C.; Ding, Y.; Liu, Y.; Chen, G.; Yu, G., *Angew. Chem. Int. Ed.* **2018,** *57*, 10246-10250.
143. Lv, C.; Zhong, L.; Yao, Y.; Liu, D.; Kong, Y.; Jin, X.; Fang, Z.; Xu, W.; Yan, C.; Dinh, K. N.; Shao, M.; Song, L.; Chen, G.; Li, S.; Yan, Q.; Yu, G., *Chem* **2020,** *6*, 2690-2702.
144. Qian, Y.; Liu, Y.; Zhao, Y.; Zhang, X.; Yu, G., *EcoMat* **2020,** *2*, e12014.
145. Fang, Z.; Yu, G., *Sci. China Chem.* **2018,** *61*, 1045.
146. Xia, C.; Xia, Y.; Zhu, P.; Fan, L.; Wang, H., *Science* **2019,** *366*, 226.

Vita

Zhiwei Fang was born in Anhui, China. He received his B.S. degree in chemistry from the University of Science and Technology of China in 2016. He began his Ph.D. studies with Prof. Guihua Yu at the University of Texas at Austin in Fall 2016. His current research focuses on the controlled synthesis and design of cost-effective nanomaterials, as alternatives to precious catalysts for key electrocatalysis processes, including electrocatalytic oxygen evolution, hydrogen evolution, and ammonium synthesis.

Email address: zf@utexas.edu

This dissertation was typed by the author.